Review Article

Short-wavelength free-electron laser sources and science: a review

E A Seddon[1,2,3]**, J A Clarke**[2,3]**, D J Dunning**[2,3]**,
C Masciovecchio**[4]**, C J Milne**[5]**, F Parmigiani**[4,6,7]**, D Rugg**[8]**,
J C H Spence**[9]**, N R Thompson**[2,3]**, K Ueda**[10]**, S M Vinko**[11]**,
J S Wark**[11] **and W Wurth**[12]

[1] The Photon Science Institute, The University of Manchester, Oxford Road, Manchester UK
[2] ASTeC, STFC Daresbury Laboratory, Sci-Tech Daresbury, Keckwick Lane, Daresbury, Cheshire WA4 4AD, UK
[3] The Cockcroft Institute, Sci-Tech Daresbury, Keckwick Lane, Daresbury, Cheshire, WA4 4AD, UK
[4] Elettra Sincrotrone Trieste s.s.14 Km. 163.5, 34149 Trieste, Italy
[5] Paul Scherrer Institute, 5232 Villigen-PSI, Switzerland
[6] Universit degli Studi di Trieste, Via A. Valerio 2, Trieste 34127, Italy
[7] C.N.R. I.O.M., Strada Statale 14, km 163.5, Trieste 34149, Italy
[8] Rolls-Royce plc, PO Box 31, Derby, DE24 8BJ UK
[9] Department of Physics, Arizona State University, Tempe, AZ 85287, USA
[10] IMRAM, Tohoku University, 980-8577 Sendai, Japan
[11] Department of Physics, Clarendon Laboratory, University of Oxford, Parks Road, Oxford OX1 3PU, UK
[12] Physics Department and Center for Free-Electron Laser Science, University of Hamburg, 22761 Hamburg, Germany and DESY Photon Science, 22607 Hamburg, Germany

E-mail: `elaine.seddon@cockcroft.ac.uk`

Abstract. This review is focused on free-electron lasers (FELs) in the hard to soft X-ray regime. The aim is to provide newcomers to the area with insights into: the basic physics of FELs, the qualities of the radiation they produce, the challenges of transmitting that radiation to end users and the diversity of current scientific applications. Initial consideration is given to FEL theory in order to provide the foundation for discussion of FEL output properties and the technical challenges of short-wavelength FELs. This is followed by an overview of existing X-ray FEL facilities, future facilities and FEL frontiers. To provide a context for information in the above sections, a detailed comparison of the photon pulse characteristics of FEL sources with those other sources of high brightness X-rays is made. A brief summary of FEL beamline design and photon diagnostics then precedes an overview of FEL scientific applications. Recent highlights are covered in sections on Structural Biology, Atomic and Molecular Physics, Photochemistry, Non-linear Spectroscopy, Shock Physics, Solid Density Plasmas. A short industrial perspective is also included to emphasise potential in this area.

Dedicated to John M. J. Madey (1943-2016) and Rodolfo Bonifacio (1940-2016) whose perception, drive and perseverance paved the way for the realisation and development of short-wavelength free-electron lasers.

PACS numbers: ?, ?

Contents

1. Introduction

X-ray free-electron lasers (XFELs) are a remarkable development in the range of tools for scientific experimentation. They provide radiation with many orders of magnitude enhancement in brightness over other X-ray sources, pulse durations down to a few femtoseconds, polarisation control, broad wavelength tunability and multi-colour operation. Consequently they have opened up huge possibilities for experimental studies. This review focuses on FELs in the hard to soft X-ray regime *i.e.* fundamental wavelengths from a few Å up to several tens of nm [1–4]. It is written with the aim of providing newcomers to the field with insights into: the basic physics of FELs, the qualities of the radiation they produce, the challenges of transmitting that radiation to end users and the diversity of current scientific applications.

The first section considers FEL theory in order to provide the foundation for discussion of FEL output properties and the technical challenges of short-wavelength FELs (Section 2). Unlike a conventional laser, the electrons in a FEL are not bound in discrete energy levels within a gain medium but are unbound (free) particles in a relativistic electron beam. Consequently a FEL is smoothly tunable and the scalable physics of the FEL mechanism allows them to operate at any wavelength from THz to X-rays. The key feature that separates FELs from other sources of synchrotron radiation (SR) such as storage rings is a positive feedback process in which electrons self-organise and radiation is exponentially amplified. This process is depicted schematically in Figure 1, which shows a bunch of relativistic electrons propagating through an array of alternating polarity dipole magnets (an undulator). Short-wavelengths FELs amplify light in a single pass of a long undulator (so called 'high-gain' operation), most often in the mode of self-amplified spontaneous emission (SASE). Through interaction with the initially incoherent radiation emission, whose intensity scales linearly with the electron density, electrons form into micro-bunches separated by the radiation wavelength. The narrow-bandwidth emission is then coherent, scaling as N^2, and with brightness enhanced $\propto N$, where N is the number of electrons emitting collectively (typically $\geq 1 \times 10^6$ for X-ray FELs). The amplification process results in almost full spatial coherence and as linac-based accelerators for FELs deliver bunches with very high peak current, FEL output peak brightness can exceed that of storage ring sources by at least eight orders of magnitude, see Figure 17. Section 2.8 describes the SASE FEL properties.

Discussion of advances in FEL properties beyond SASE is included in an overview of existing X-ray FEL facilities, future facilities and FEL frontiers, highlighting the state-of-the-art capabilities of short-wavelength FELs and anticipated future developments (Section 3). A comparison of FEL properties with other sources is given in Section 4 and details of optics and diagnostics of FEL beamlines can be found in Section 5. Section 6 focuses on the diverse range of scientific applications of short-wavelength FELs including their potential industrial utilisation. After pioneering work at longer wavelengths the first results from a FEL with a fundamental wavelength below 100 nm were obtained on the FLASH facility [1] at DESY. (This machine, originally known as the Tesla Test Facility, TTF, first lased in February 2000 at a wavelength of 109 nm.) FLASH opened to users in 2005 and its intense beams immediately enabled ground-breaking work. Not surprisingly many of the first publications were in the field of atomic, molecular and optical physics and this early work has been steadily built upon ever since (Section 6.2) as researchers continue to take advantage of the extremely short pulse duration and the high peak power of FEL beams; for reviews see [5–11]. FLASH was also widely used as an essential test-bed for the development of ideas and techniques that would utilise the short wavelength and coherence of this
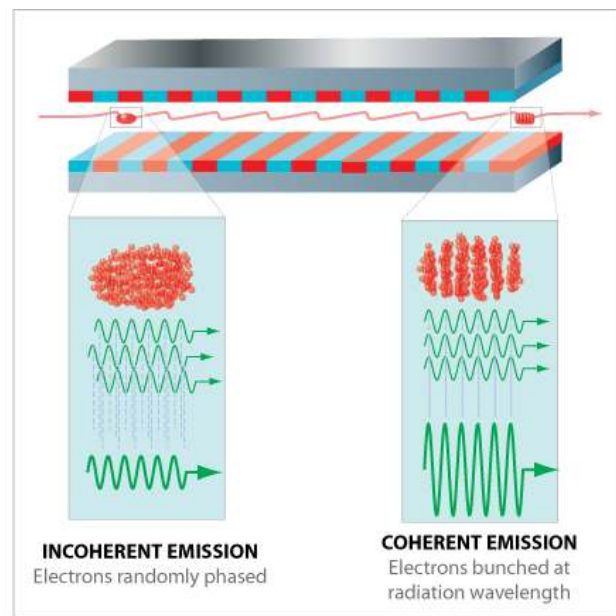
Figure 1. Schematic of the basic FEL mechanism. Bunches of randomly phased relativistic electrons propagate through an undulator, an array of alternating polarity dipole magnets (depicted as red and blue blocks). The electrons oscillate transversely causing radiation emission. The transverse electric field of the co-propagating radiation couples to the electron transverse velocity allowing an energy exchange. This coupling enables a positive feedback process in which the electrons start to micro-bunch, coherently enhancing their emission, which acts back on the electrons further enhancing the micro-bunching, and so on, giving an exponential growth of the radiation intensity.

type of source, notably in coherent diffractive imaging (Section 6.1). The world's first Ångstrom-wavelength FEL, the Linac Coherent Light Source, LCLS [2], opened its doors to users in October 2009 and has proved a great success ever since. LCLS was followed by SACLA [3], a more compact hard X-ray machine, and FERMI@elettra [4], which provides much improved stability at soft X-ray wavelengths through seeding. These facilities have served as a focus for international collaboration and have enabled both the establishment of advanced techniques and the widespread development of expertise that will be essential for the full utilisation of upcoming facilities including PAL XFEL [12], SwissFEL [13], European XFEL [14] and LCLS-II [15].

Whilst short photon pulses are important for very high peak power, they are also essential for time-resolved measurements using pump-probe techniques. The importance of dynamics measurements was recognised from the outset and synchronisation of table-top lasers with FEL beams has been a prime technical challenge. The implementation of seeding has had a major impact in this area though the use of time-stamping has proved an effective method to determine time dependencies in notable cases. Recent results in, and further references for, dynamics on FELs can be found in various parts of Section 6.

2. High-Gain FEL Theory and Standard Properties

This section gives a summary of the underlying theoretical framework of high-gain FELs and a description of the standard radiation properties. Readers are also referred to other reviews [16–19] and books [20–23] on this topic.

2.1. Background

The radiation from electron beams passing through a series of alternating-polarity magnetic fields was first theorised by Motz [24] and Ginzburg [25]. Motz also demonstrated the first undulator in 1953 [26] then Phillips developed the ubitron [27] ('undulating beam interaction') a microwave emitting undulator device which demonstrated some of the key FEL features of micro-bunching and the extraction of energy from the electron beam.

The free-electron laser concept was introduced by Madey in 1971 [28] without knowledge of the earlier work by Motz and Phillips [29]. He used a quantum mechanical description and recognised the potential scalability of the technique to short wavelengths. Madey and colleagues proceeded to demonstrate a FEL configuration in which externally generated laser light was amplified by up to 7 % *via*

co-propagation with an electron beam in a single pass through a short undulator magnet [30]. Such a system is considered to be a low-gain amplifier. A second set of experiments by the same group demonstrated a low-gain oscillator FEL configuration [31], in which an optical cavity was introduced, allowing exponential radiation amplification by interaction with successive electron bunches. These experiments prompted much theoretical interest and classical alternatives to the quantum theory were proposed by, for example, Colson [32] and Hopf [33]. Work by a number of groups led to the conclusion that a FEL can be described classically to a very good approximation, with the quantum contribution, due to electron recoil on photon emission, being negligibly small down to X-ray wavelengths [16]. Approximating to a constant radiation intensity over one undulator pass, Colson's approach showed that in the low-gain regime of FEL operation the FEL equations take the same form as those describing a simple pendulum, as described in Section 2.5.

The high-gain theory, described in Section 2.7, was developed in the 1970s and 80s [34–42] and showed the possibility of exponential increase in radiation intensity during a single undulator pass. This removed the requirement for an optical cavity, bypassing limitations in mirror technology at short wavelengths, hence opening the way for the development of X-ray FELs. The high-gain FEL was first demonstrated in 1985 at microwave wavelengths [43] and was followed by several experiments, including [44–48], verifying the properties of the output against theory at shorter wavelengths. Since then successive advances have allowed the minimum FEL wavelength to be reduced until today LCLS [2] and SACLA [3] operate in the hard X-ray. Details of the high-gain FEL output properties are given in Section 2.8 and the required electron beam properties are given in Section 2.9.

For a more extensive historical perspective readers are referred to the reviews by Madey [29] and Pellegrini [49]. A chronology of developments in short-wavelength FELs is given in Section 3.

2.2. Fundamentals

In a FEL, highly relativistic electrons with Lorentz factor $\gamma = E/mc^2 = E$ [MeV]$/0.511$ take a sinusoidal path through the undulator magnetic field and emit synchrotron radiation due to the transverse acceleration in x. In the electron rest frame the emission can be approximated by the usual symmetric emission from an oscillating charge, as shown in Figure 2. The electrons follow closely behind the emitted radiation in their direction of travel, z, such that in the lab frame the radiation emission is concentrated in the forward direction, as shown in
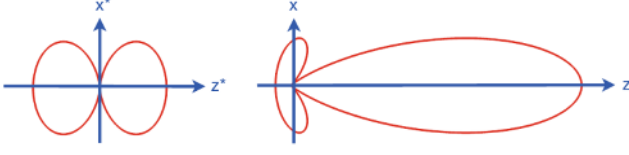
Figure 2, with opening angle $1/\gamma$ [20].

Figure 2. Radiation distribution in the laboratory frame from a charge oscillating in x while at rest in z (left) and moving in z at speed $v = 0.9c$ (right). Reproduced with permission from Springer Tracts in Modern Physics Vol. 258 [20], Copyright (2014) Springer.

The propagation of the radiation ahead of the electrons is termed 'slippage'. In free-space propagation the slippage is set by the relativistic electron velocity, $v = c(1 - 1/\gamma^2)^{\frac{1}{2}}$, which is less than the speed of light by just one part in a billion for the ~ 10 GeV energies typically required for hard X-ray FELs. When propagating within the undulator a second contribution to the slippage comes from the undulating electron trajectory (Section 2.3) which further reduces the average z-velocity. These two contributions are typically of similar magnitude. As will be seen, the amount of slippage defines the FEL wavelength (Section 2.4) and temporal properties of the output pulse (Section 2.8.1).

2.3. Electron Trajectory in the Undulator

Undulators provide a sinusoidal magnetic field in either one or two planes. The first case is termed 'planar' and generates linearly polarised light. The second is usually termed 'helical' or 'elliptical' and generates circularly or elliptically polarised light. There is sometimes the ability to vary the polarisation by longitudinal adjustment of the magnetic arrays. More details can be found in a number of texts on the topic, for example [50].

The transverse component of the electron velocity in the presence of the magnetic field can be established using the Lorentz equation

$$\mathbf{F} = \frac{d(\gamma m \mathbf{v})}{dt} = e(\mathbf{E} + \mathbf{v} \times \mathbf{B}) = -e v_z B_y \hat{\mathbf{x}} \quad (1)$$

where the simplifying assumption is made that $\mathbf{E} = 0$ and the small components of the cross product term are neglected. Assuming a planar undulator field $B_y = B_0 \sin(k_u z)$, with peak magnetic field B_0 and wavenumber k_u, changing the independent variable from t to z and integrating gives the transverse velocity

$$v_x = \frac{eB_0}{\gamma m k_u} \cos(k_u z) = \frac{Kc}{\gamma} \cos(k_u z) \quad (2)$$

and $v_y = 0$, where K is the undulator parameter

defined as

$$K = \frac{eB_0}{mck_u} = 93.36 B_0[T]\lambda_u[m] \quad (3)$$

and λ_u is the period of the undulator magnetic field. The maximum deflection angle is therefore given by $\vartheta_{max} = K/\gamma$. Typical undulator periods of a few centimetres and fields of ~ 1 T give $K \simeq 1-3$, such that the electron trajectory in the undulator lies just within the $1/\gamma$ opening angle of the synchrotron radiation.

Using $v_z^2 = v^2 - v_x^2$ it is straightforward to find the electron longitudinal velocity averaged over an undulator period

$$\bar{v}_z \simeq c\left(1 - \frac{1 + \frac{1}{2}K^2}{2\gamma^2}\right). \quad (4)$$

The dependence of the longitudinal electron velocity on energy is important in the formation of micro-bunching as shown in Section 2.5.

2.4. Resonance Condition

Introducing a co-propagating radiation field, $E_x = E_0\cos(kz - \omega t + \phi)$ of constant amplitude E_0 and phase ϕ, the transverse component of the electron velocity (2) couples with the transverse electric field to allow energy transfer, the rate of which is given by

$$\frac{d\gamma mc^2}{dt} = \mathbf{F} \cdot \mathbf{v} = eE_x v_x$$
$$= \frac{eE_0 Kc}{2\gamma}\{\cos[(k + k_u)z - \omega t + \phi]$$
$$+ \cos[(k - k_u)z - \omega t + \phi]\}. \quad (5)$$

The right-hand side of (5) represents the superposition of two waves, where the first wave has phase velocity $< c$ and is known as the ponderomotive wave. The second wave has phase velocity $> c$ and can be neglected [16]. Sustained energy transfer can occur when the electron longitudinal velocity $\bar{v}_z$ is matched to the phase velocity of the ponderomotive wave $\omega/(k + k_u)$, so using (4) leads directly to the resonance condition

$$\lambda_r = \frac{\lambda_u}{2\gamma^2}\left(1 + \frac{K^2}{2}\right). \quad (6)$$

It is convenient to define the phase of the electron relative to the ponderomotive wave as

$$\theta = (k + k_u)z - \omega t \quad (7)$$

in which case at resonance the electrons remain in phase with the ponderomotive wave and $d\theta/dt = 0$.

Equation (6) defines the resonant wavelength of the FEL in terms of the electron beam energy, undulator period and undulator parameter. For typical undulator parameters, as given in Section 2.3, the
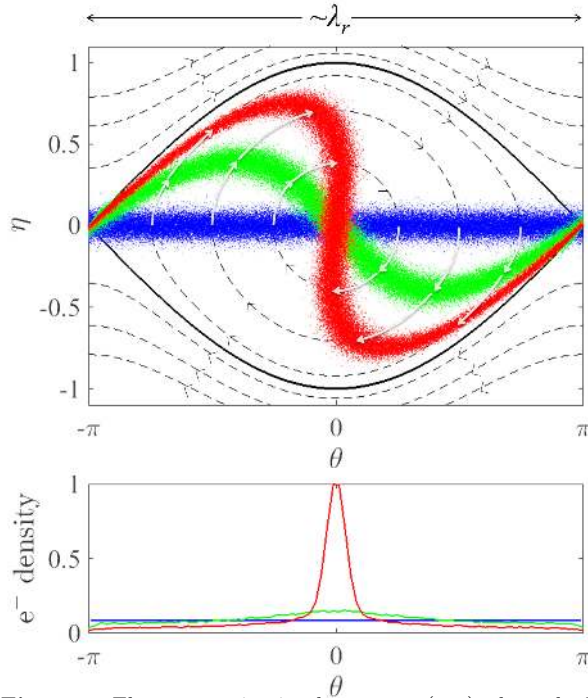
beam energy must be in the multi-GeV range to reach sub-nanometre wavelengths. The resonance condition also explains the smooth wavelength tunability of the FEL: it is only necessary to change the on-axis magnetic field, which can easily be done by changing the gap between the magnetic arrays of the undulator. Gap tuning can typically give a factor around four in wavelength tuning while maintaining sufficient field for lasing. A much wider wavelength range is accessible by changing the electron beam energy, though this requires adjusting multiple accelerator parameters so is less convenient.

It is straightforward to show that the resonance condition corresponds to the electrons slipping back exactly one wavelength relative to the radiation field per undulator period, as illustrated in Figure 3. This relative slippage between electrons and radiation has important consequences for the longitudinal coherence properties of the FEL output, as described in Section 2.8.1.

Figure 3. Schematic of the undulator resonance condition. As the electrons traverse one undulator period the radiation propagates forward relative to the electrons by one radiation wavelength, allowing sustained energy transfer. Depending on their longitudinal alignment, electrons either gain or lose energy, which leads to micro-bunching. Figure constructed following the approach of [51].

2.5. Micro-Bunching

Depending on the phase of an electron relative to the ponderomotive phase, the transfer of energy can be positive, negative, or zero, as shown in Figure 3. Defining γ_r as the resonant energy, a normalised relative electron energy

$$\eta = \frac{\gamma - \gamma_r}{\gamma_r} \qquad (8)$$

can be introduced. Using (5) and (7), the evolution of the electron energy and ponderomotive phase can then be expressed in a form identical to the equations

describing the motion of a simple pendulum [16, 32]

$$\frac{\mathrm{d}\eta}{\mathrm{d}z} = -\chi_1 E_0 \sin\theta \qquad (9)$$

$$\frac{\mathrm{d}\theta}{\mathrm{d}z} = 2k_u\eta \qquad (10)$$

where $\chi_1 = eKJJ/(2\gamma_r^2 mc^2)$ and the independent variable is changed from t to z. The equations represent an average over an undulator period and the parameter JJ simply accounts for a reduction in coupling due to the oscillation in electron longitudinal velocity in a planar undulator compared to a helical undulator [16, 52], with typical values in the range $0.7 - 1$.

The longitudinal electron dynamics described by (9) and (10) can be represented in the energy-phase plane (or 'longitudinal phase space') as shown in Figure 4. The separatrix defines the region of interest, within which electrons are said to be confined within a ponderomotive well. Electron bunches in FELs are generally much longer than the resonant wavelength so electrons are distributed over many ponderomotive wells and approximately evenly within an individual well. Electrons initially in the range $-\pi < \theta < 0$ gain energy from the field while electrons in the region $0 < \theta < \pi$ lose energy, giving an energy modulation. The higher energy electrons advance in phase because they are deflected less in the magnetic field of the undulator thus take a shorter trajectory and the lower energy electrons are retarded so that the energy modulation is converted to a density modulation. This is the FEL micro-bunching.

In the analogy to a simple pendulum θ and η correspond to the angle from vertical and angular velocity respectively. A phase space trajectory within the separatrix is analogous to the pendulum swinging, while one outside represents rotation. Figure 4 is equivalent to an array of pendulums that are initially stationary with a range of angles, evolving to a later case with most hanging near vertical, *i.e.* 'bunched' in space while spread in angular velocity.

2.6. Net Energy Transfer

In Figure 4, micro-bunching occurs around $\theta = 0$ and the system is symmetric with no net energy transfer. The process through which net energy transfer develops can be appreciated by picturing the ponderomotive well defined by the separatrix in Figure 4 moving negatively in phase relative to the electrons during the interaction. The position about which electron micro-bunching occurs is then displaced to a region of energy loss, such that net energy loss takes place.

The cause of this phase shift differs between low-gain and high-gain FELs. The FEL interaction shown

Figure 4. Electron motion in phase space (top) where the FEL interaction is dominated by the radiation field (*i.e.* low-gain FEL). The blue points represent the initial electron distribution – evenly separated in phase and with a small energy spread centred around the resonant energy ($\eta = 0$). The system evolves with the electrons following the dashed lines (phase space trajectories) such that energy modulation (green points) occurs, which develops into strong density modulation, *i.e.* micro-bunching (red points), which is shown by the projection onto the θ-axis (bottom). The solid black line is the separatrix.

in Figure 4 is that of a low-gain FEL. Here net energy loss occurs when the initial mean electron energy is positively detuned ($\eta > 0$) from resonance with the dominant radiation field. For low-gain oscillators with no external radiation field, this is equivalent to stating that gain occurs at a wavelength offset from that of resonance with the electron beam, as per Madey's theorem [28, 29]. More details on low-gain FELs can be found in, among others, [21, 22, 53]. It should also be noted that an inverse FEL effect for electron acceleration is also possible [54, 55].

For high-gain FELs it is the FEL interaction itself which drives the radiation phase and so enables net energy transfer.

2.7. High-Gain Theory

Because the pendulum model assumes a fixed radiation field its validity is limited to low-gain FELs, where the effect of net energy transfer is negligible. This section gives an overview of deriving and solving the high-gain FEL [34–42] equations leading to a description of the high-gain FEL process shown in Figure 5. A more detailed derivation is given in several texts [16, 19, 20].

2.7.1. Self-Consistent Model and Approximations

To describe the high-gain FEL self-consistently the radiation field must be allowed to evolve. The essential procedure is to combine together the coupled electron energy and phase equations (9 and 10), with the Maxwell wave equation

$$\left[\frac{\partial^2}{\partial z^2} - \frac{1}{c^2}\frac{\partial^2}{\partial t^2} - \nabla_\perp^2\right] E_x = \frac{1}{\epsilon_0 c^2}\left[\frac{\partial J_x}{\partial t} + c^2\frac{\partial \rho_e}{\partial x}\right] \tag{11}$$

which describes the evolution of the transverse radiation electric field when driven by the electron beam transverse current [16]. Here $\nabla_\perp^2$ is the transverse Laplacian, ϵ_0 is the permittivity of free space, J_x is the transverse current density, and ρ_e is the charge density which is a relatively small contribution and can usually be neglected [16], though space charge effects should be accounted for in the formation of micro-bunches [20, 21].

Further simplifying approximations can be applied in various combinations to aid computational and analytic solutions. In the slowly varying envelope approximation (SVEA) [56], the radiation electric field is decomposed into a fast oscillatory term, $e^{i(kz-\omega t)}$, and a complex envelope, $\tilde{E}(z,t) = \frac{1}{2}Ee^{i\phi}$. Assuming that the envelope varies slowly in both z and t, the second order derivatives in these variables in (11) reduce to first order, which is valid in the anticipation of long-range coherence and narrow bandwidth [38]. A less restrictive form of the SVEA is commonly used in which the field envelope is assumed to be a slowly varying function of $\tilde{E}(z-ct)$ only, so that any backward propagating, non-resonant, waves are ignored [57, 58]. In this way, relatively short radiation pulses of the order of a few radiation wavelengths, which would violate the full SVEA approximation of [56], may be modelled so long as they do not evolve significantly over one undulator period.

In a similar way the current density term can be simplified. Initially treated as a sum over single-particle currents, with a j-subscript designating single electrons, it can be averaged over a region of the electron beam, Δ (an integer number of radiation wavelengths), over which it is assumed that the field and particle properties do not change significantly [23]. The right hand side of the wave equation can then be expressed in terms of a collective variable known as the bunching parameter

$$b = \langle e^{-i\theta_j}\rangle_\Delta \tag{12}$$

whose phase is that about which micro-bunching occurs and with a magnitude varying between zero, where electrons are uniformly longitudinally distributed, and one, where the electrons are fully bunched and have the same ponderomotive phase

within the slice. The Maxwell wave equation in the SVEA is then

$$\left(\frac{\partial}{\partial z} + \frac{1}{c}\frac{\partial}{\partial t} + \frac{\nabla_\perp^2}{2ik} \right) \tilde{E} = \chi_2 \langle e^{-i\theta_j} \rangle_\Delta \qquad (13)$$

where

$$\chi_2 = \frac{eKJJn_e}{4\epsilon_0\gamma} \qquad (14)$$

and n_e is the average electron volume density.

Another common simplification is a 1D approximation of the FEL equations, where transverse dependencies of the bunch charge density and radiation field are neglected (see for example [20]). This is a reasonable approximation in many cases and can be related to the 3D result to assess the impact of radiation diffraction and electron beam focussing *via* correction formulae [59].

One further simplification is to reduce the time dependent system to the 'steady-state' by dropping the $\partial/\partial t$ slippage term in the wave equation and considering a slice comprising a single ponderomotive well [23], thus allowing no longitudinal variations in electron bunch and radiation properties. Using j-subscripts to represent individual electrons in the pendulum equations, the system then comprises $2N_e + 1$ coupled non-linear equations where N_e is the number of electrons per well. Even using a further 'macroparticle' approximation, where each macroparticle represents many electrons, the system of equations is still large and requires numerical solution. Time-dependent simulation codes often work by extending the steady-state model to multiple slices with slippage included *via* propagation of the radiation field between slices.

Modern FEL projects employ a range of simulation codes (reviewed in [19]), with 1D and steady-state models useful for faster simulation times where appropriate. For design studies and benchmarking, 3D time-dependent models operating with the SVEA [60–63] are most commonly used (either with or without averaging over an undulator period [64]) and show close agreement with experiments [2, 65–67], while non-SVEA codes (for example [68]) have much wider bandwidth allowing modelling of more exotic operating modes.

2.7.2. FEL Parameter

This section follows [23] to describe the rescaling of the FEL equations (9, 10, and 13), in terms of the 'FEL parameter' ρ, into a dimensionless form which contains the basic physics of the system. It is shown that ρ then conveniently describes many aspects of the FEL performance and output [41].

In anticipation of an exponentially growing solution, the distance through the undulator, z, is scaled by a nominal 'gain length', proportional to the distance for an e-fold increase in radiation intensity. The scaled distance is $\bar{z} = z/l_g$, with

$$l_g = \lambda_u/(4\pi\rho) \qquad (15)$$

the nominal gain length. The re-scaled phase equation (10) is

$$\frac{\mathrm{d}\theta_j}{\mathrm{d}\bar{z}} = 2k_u l_g \eta_j = p_j \qquad (16)$$

where parameters are collected into a new scaled energy variable, $p = 2k_u l_g \eta = \eta/\rho$. In a similar way, re-scaling the energy equation (9) in terms of p and $\bar{z}$ gives

$$\frac{\mathrm{d}p_j}{\mathrm{d}\bar{z}} = -2k_u l_g^2 \chi_1 (\tilde{E} e^{i\theta_j} + \text{c.c.}) = -(A e^{i\theta_j} + \text{c.c.}) \quad (17)$$

where parameters are collected into a scaled complex field amplitude $A = 2k_u l_g^2 \chi_1 \tilde{E}$. Finally, the steady-state and 1D form of the wave equation (13) is re-scaled in terms of A and $\bar{z}$

$$\frac{\mathrm{d}A}{\mathrm{d}\bar{z}} = 2k_u l_g^3 \chi_1 \chi_2 \langle e^{-i\theta_j} \rangle_\Delta = \langle e^{-i\theta_j} \rangle_\Delta. \qquad (18)$$

Given the exponential solution (Section 2.7.3) it is required that $2k_u l_g^3 \chi_1 \chi_2 = 1$, which defines the dimensionless ρ-parameter as a collection of system parameters and fundamental constants

$$\rho = \left[\frac{\chi_1 \chi_2}{(2k_u)^2} \right]^{1/3} = \left(\frac{e^2 K^2 JJ^2 n_e}{32\epsilon_0 \gamma^3 mc^2 k_u^2} \right)^{1/3}. \qquad (19)$$

For short-wavelength FELs ρ is typically in the range 10^{-4} to 10^{-3}, with the lower end of the range at shorter wavelengths due to the $1/\gamma$ scaling. The significance of ρ is discussed in the following sections.

2.7.3. Analytic Solution

An analytic solution to the high-gain FEL equations can be found by linearising the equations in terms of the radiation field and two collective variables to represent the electrons [41]. The radiation field, A, and the bunching parameter, b, are as previously defined but a collective energy variable is introduced, $P = \langle p_j^{-i\theta_j} \rangle$ (not to be confused with power in later sections). This describes the amplitude and phase of the energy modulation. For a resonant interaction and zero energy spread the FEL equations (16-18) reduce to a set of three coupled linear equations

$$\dot{b} = -iP \qquad (20)$$

$$\dot{P} = -A \qquad (21)$$

$$\dot{A} = b \qquad (22)$$

which can easily be collected into one third order equation

$$\dddot{A} = iA. \tag{23}$$

The full solution is a linear combination of three components, corresponding to cases with constant magnitude, exponential decay and – crucially – exponential growth. Given an undulator much longer than the gain length, the exponential growth dominates and provides orders of magnitude increase in radiation intensity. The exponentially growing solution is

$$A = A_0 e^{(i+\sqrt{3})\bar{z}/2}. \tag{24}$$

The power gain length is therefore $L_G = l_g/\sqrt{3}$, such that the power grows as

$$P_{\mathrm{rad}} \propto e^{z/L_G}. \tag{25}$$

Short-wavelength FELs starts up from either low-intensity spontaneous emission as described in Section 2.8.1 or from 'seeding' *via* an external source as described in Section 3.

2.7.4. Physical Interpretation of the High-Gain FEL Interaction

The evolution of the longitudinal phase space in a high-gain FEL is shown in Figure 5, as determined by numerical solution of the high-gain equations. This can be used in combination with the analytic solution to give a physical picture of the high-gain FEL interaction.

The electrons are initially uniformly distributed longitudinally with a finite energy distribution as shown in Figure 5 (a). Exponential growth occurs in the radiation intensity (Figure 5 (f)), as well as the amplitude of the electron beam energy modulation and micro-bunching, as can be seen in Figure 5 (b-d). The interaction is essentially a positive feedback process which can be described in terms of a three-step cycle [49]:

- The interaction of the electrons with the radiation field causes energy modulation of the electron beam on the scale of the radiation wavelength, λ_r.

- The energy modulation evolves into density modulation (micro-bunching), since higher energy electrons are deflected less in the undulator (4).

- The micro-bunching results in increased radiation intensity through coherent emission.

For this cycle to conserve energy, the micro-bunching must occur at a phase corresponding to net energy loss, but from Figure 4 it is not obvious that this should be the case. Consideration of the phases resolves this. It is apparent that (20-22) imply phase dependencies between the complex parameters A, P, and b, and that (23) requires phase rotation of $\pi/2$ over three

derivatives. The exponentially growing solution for A (24) indeed has a phase rotation component as well as exponential growth, and it can be shown that P and b take equivalent forms. The exponentially growing solution dominates through having a relatively small ($\pi/6$) phase difference between A, P, and b, and their respective derivatives with respect to $\bar{z}$. The additional radiation emission thereby adds constructively to the radiation field already present, and likewise for the energy modulation and bunching, while the phase of each parameter is driven to negative values with increasing $\bar{z}$, as can be seen by the phase of the separatrix in Figure 5 (a-e). Essentially, as the phases shift an equilibrium in the relative phases of A, P, and b has the bunching phase trailing the centre of the ponderomotive well (by $\pi/3$), corresponding to a position of continuous net energy transfer.

The exponential amplification cannot continue indefinitely and eventually saturates (Figure 5 (f)) as the electrons approach maximal bunching ($|b| = 1$). The phase space at saturation is shown in Figure 5 (e).

2.8. Output Properties of the SASE FEL

This section summarises the main properties of high-gain FELs in the standard SASE operating mode. More advanced operating modes and the corresponding enhancements over the properties given here are described in Sections 3 and 4.

2.8.1. Temporal Structure

The default operating mode of X-ray FELs is called self-amplified spontaneous emission (SASE) [41]. Here the electron beam injected into the undulator has a small intrinsic initial bunching b_0, due to random microscopic density variations in the electron bunch at the sub-wavelength scale. This initial bunching, termed shot noise, is always sufficient to trigger exponential growth in the coupled electron-radiation system. The further evolution of the longitudinal radiation pulse characteristics is then strongly dependent on the relative slippage between radiation and electrons. By including this relative slippage in the FEL equations the system can be solved to show that at saturation the radiation pulse comprises a random superposition of many spikes with uncorrelated phases [69]. The maximum peak-to-peak distance between spikes is $2\pi l_c$ where the co-operation length

$$l_c = \lambda_r/(4\pi\rho) \tag{26}$$

is the slippage in a gain length. A wavefront therefore propagates a distance l_c through the electron beam per gain length and the co-operation length is seen to define the scale at which collective effects evolve throughout the electron beam. For a sufficiently
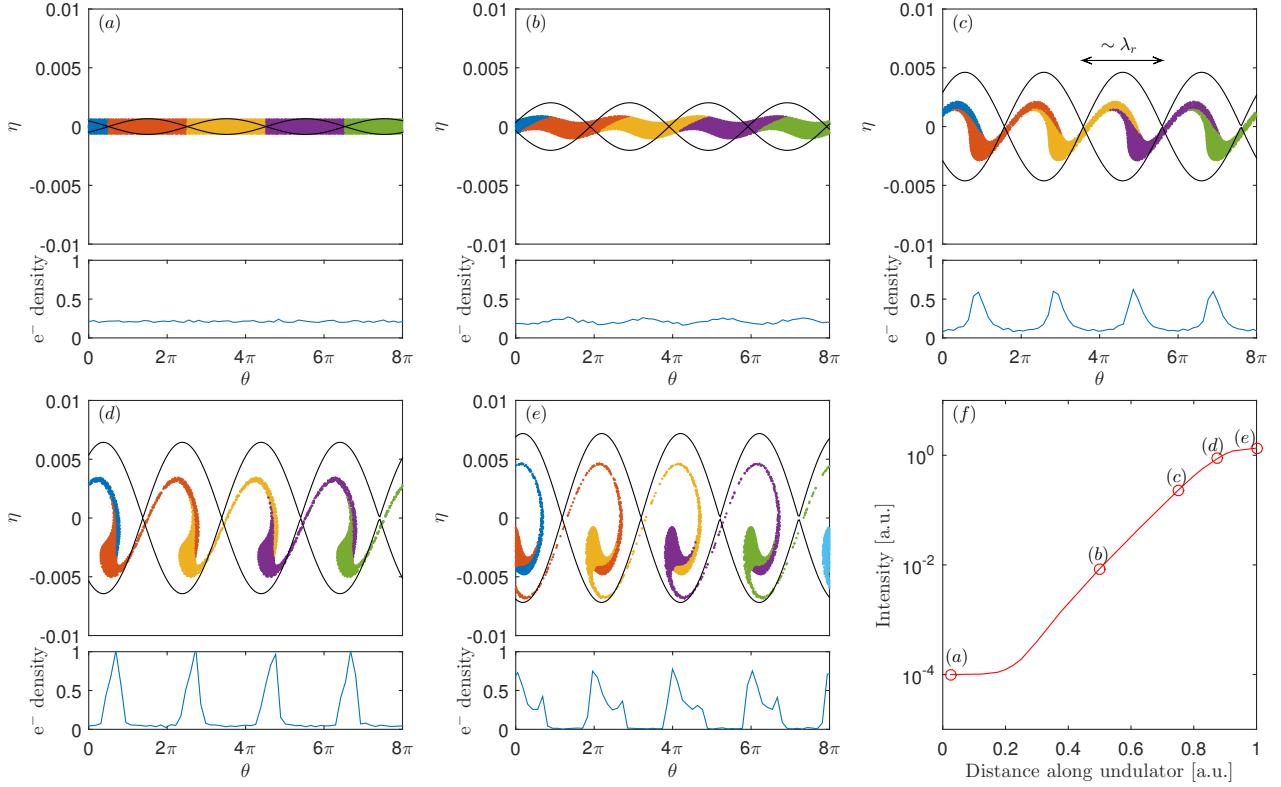
Figure 5. High-gain FEL longitudinal phase space evolution. Plots (a)-(e) show the longitudinal phase space above the corresponding density modulation at different points in the high-gain amplification process, as indicated in the plot of radiation intensity against distance through the undulator (f). Plot (a) is the initial condition of the electron beam, (b) and (c) are during the exponential growth phase as modulation and bunching grow, plot (d) is the start of saturation as the electrons become maximally bunched and (e) is into saturation as the phase space continues to evolve with little power growth. Different slices of the electron bunch are marked in different colours. During amplification the separatrix (solid black line) is driven to negative phase and the micro-bunching remains centred about a phase corresponding to net energy loss. Figure constructed following the approach of [20].

long electron beam, different regions along the beam develop from the localised noise source autonomously and are therefore uncorrelated in phase. In this sense, the SASE process can be considered as a 'localised' collective process. Typically, in the X-ray the electron bunch length $l_b \gg 2\pi l_c$, so there are many random spikes in the output pulse which has a total length equal to that of the electron bunch. If however the electron bunch length $l_b \leq 2\pi l_c$ only one SASE spike can develop and single spike output is possible. Such a regime is known as weak superradiance or single-spike SASE [70, 71].

The co-operation length also then parameterises the SASE radiation coherence. The coherence time is [72]

$$\tau_{\mathrm{coh}} \simeq \frac{1}{\rho\omega}\sqrt{\frac{\pi \ln N_c}{18}} \qquad (27)$$

where $N_c = I/(e\rho\omega)$ with I the electron bunch current. This can be simplified using (26) and by noting that for typical X-ray FELs the square root term evaluates to $\simeq 1.6$ to show that the coherence length is typically

about 3 co-operation lengths

$$l_{coh} \simeq 3l_c \qquad (28)$$

or half the peak-to-peak spacing of the SASE spikes.

The features of a typical SASE pulse are illustrated in Figure 6 which shows simulation results for a high-gain SASE FEL with parameters similar to FLASH [1]. Figure 6 (a) shows the intensity profile comprising multiple random spikes. Figure 6 (b) shows the radiation phase, colour-coded to indicate the associated radiation intensity. The phase is seen to vary randomly from spike to spike but is almost constant within each spike showing that individual spikes have good temporal coherence. Figure 6 (c) shows the electron bunch current profile. In the simulation the current is averaged over slices one wavelength long so this shows that even if the electron bunch is perfectly smooth over this scale the output pulse will be noisy due to the shot noise at sub-wavelength scales. Finally Figure 6 (d) shows the spectrum of the output pulse which also comprises multiple random spikes.
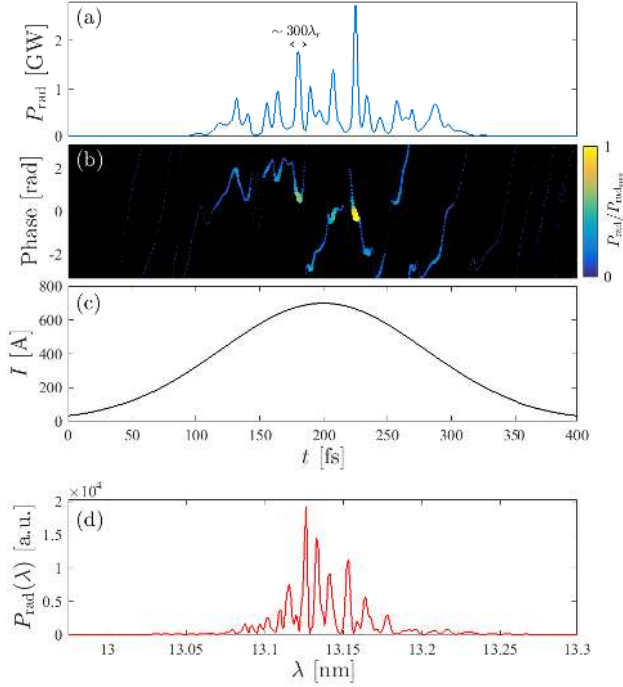
Figure 6. Example SASE properties. The plots show simulation results for a high-gain SASE FEL with parameters similar to FLASH [1], results are shown at saturation: (a) radiation temporal profile consisting of multiple spikes, (b) radiation phase showing phase correlation within but not between spikes, (c) the idealised Gaussian current profile used in the simulation and (d) the radiation spectrum, also consisting of multiple spikes.

2.8.2. Bandwidth

The pulse shown in Figure 6 is just one example of a typical SASE output pulse. In practice each pulse has a different arrangement of spikes, temporally and spectrally, due to the start up from noise. It is important to note that although the number of temporal spikes is approximately the same as the number of spectral spikes, there is not a one-to-one correspondence between them. Each temporal spike does not have a distinct wavelength but has the full bandwidth of the envelope which is the gain bandwidth of the FEL system. This can be seen clearly in Figure 7 which shows a windowed Fourier transform of the simulated FEL pulse in Figure 6 (a).

The gain bandwidth can be derived analytically from the FEL equations (16-18) by examining the system in terms of a small perturbation away from the resonant energy to determine the exponential gain as a function of this energy detuning, then using the resonance condition (6) to relate energy detuning to wavelength detuning. The result obtained is that the relative rms bandwidth narrows with distance travelled through the undulator as $\sigma_\lambda \simeq 2\rho\sqrt{\pi/\bar{z}}$. The FEL

approaches saturation at $\bar{z} \geq 10$ so the rms bandwidth of the saturated output is

$$\sigma_\lambda \simeq \rho. \tag{29}$$

2.8.3. Power, Pulse Energy, and Flux

As the radiation field grows along the undulator the scaled parameters (A, P and b) increase together to near unity – at this point the electrons are fully bunched and the power saturates. Saturation at $P \approx 1$ corresponds to a mean relative electron energy loss of $\bar{\eta} = (\gamma - \gamma_r)/\gamma_r \approx \rho$ as shown in Figure 5 (d). Thus ρ is again shown to be a fundamental indicator of FEL performance as it represents the efficiency of the conversion of electron beam power to radiation power. The peak radiation power at saturation is given by

$$P_{\rm rad} \approx \rho P_{\rm beam} = \rho I_{\rm peak}[{\rm A}]E[{\rm eV}] \tag{30}$$

where $P_{\rm beam}$, $I_{\rm peak}$ and E are the electron beam peak power, peak current, and energy respectively. Typically for short-wavelength high-gain FELs ρ is in the range 10^{-4} to 10^{-3}, the electron beam energy is in the tens of GeV and the peak current is a few kA, so FEL peak output power is in the tens of GW.

The FEL power scales as $P_{\rm rad} \propto n_e^{4/3}$ in the steady-state, which can be seen from the scalings $P_{beam} \propto n_e$ and $\rho \propto n_e^{1/3}$ (19). The power is non-linear in n_e because the electrons become microbunched by the FEL interaction leading to a coherent superposition of emission. For unbunched electrons randomly distributed over a length much longer than the
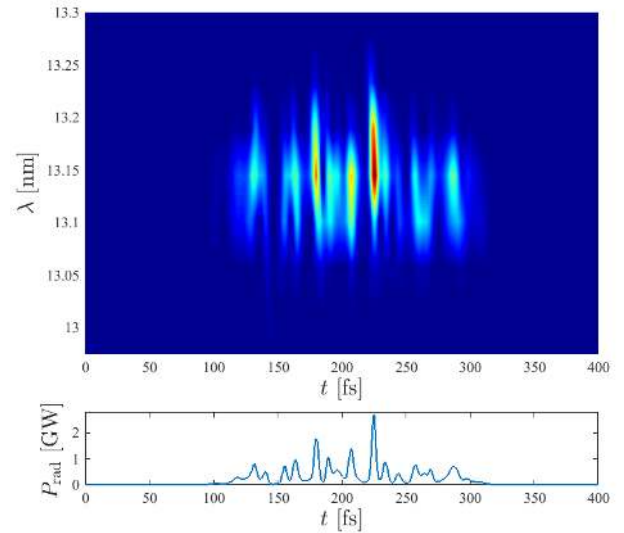

Figure 7. Time-frequency plot of the simulated SASE FEL pulse shown in Figure 6 (a). The top panel shows a windowed Fourier transform of the output pulse and the bottom panel shows the intensity profile. Each temporal spike is seen to have the full gain bandwidth.

radiation wavelength, undulator radiation is incoherent and scales as $P_{\rm rad} \propto n_e$ [49], whereas for a perfectly pre-bunched beam injected into an undulator, where the bunching factor remains constant, the power scales as $P_{\rm rad} \propto n_e^2$. In the FEL the interaction self-bunches the electrons; the number of electrons emitting together in a gain length scales as $n_e^{2/3}$ (since $I \propto n_e$ and $l_c \propto n_e^{-1/3}$), such that the power scaling $P_{\rm rad} \propto n_e^{4/3}$ is intermediate between the unbunched and fully pre-bunched cases. However, under certain conditions, slippage effects in the high-gain FEL can lead to a pure superradiant emission where the power does indeed scale as $P_{\rm rad} \propto n_e^2$ [70].

The pulse energy is the instantaneous power integrated over the pulse duration. With peak powers in the tens of GW and pulse durations 10-100 fs the pulse energy is typically 100 μJ to a few mJ. The number of photons per pulse is the pulse energy divided by the photon energy, typically 5×10^{10} to 5×10^{11}. Table 1 on page 15 lists the pulse energies available from currently operational facilities. Higher harmonics are also present in the FEL output, with intensity less than a few percent of the fundamental [73]. FEL facilities also produce spontaneous undulator radiation, the power of which can be on the order of the FEL power for hard X-ray FELs [20]. Nevertheless, the FEL radiation is many orders of magnitude brighter than this due to the narrower angular and spectral distributions.

2.8.4. Transverse Coherence
The radiation emission over the first few gain lengths of the FEL process has significant higher order mode content but because the growth of the field is driven most strongly on-axis this favours coupling to the fundamental Gaussian mode – higher order modes are wider or even have a minimum on axis and are therefore driven less strongly [16]. By the time the FEL is close to saturation the fundamental mode strongly dominates and the output beam is close to diffraction limited [74–76]. Beyond saturation the spatial coherence starts to degrade due to the growth in the number of higher order transverse modes.

2.8.5. Brightness
As shown, a FEL produces pulses of high peak power, narrow bandwidth and near-diffraction limited spatial coherence. This means it is possible to focus an intense flux of near-monochromatic photons onto a small area, making the X-ray FEL an extremely useful scientific tool. The flux, bandwidth and spatial coherence are simultaneously quantified by the spectral brightness, defined as

$$B = \frac{\Phi}{4\pi^2 \Sigma_x \Sigma_{\theta x} \Sigma_y \Sigma_{\theta y}} \qquad (31)$$

where Φ is the spectral flux, the number of photons per second divided by the relative bandwidth and Σ represents a quadrature sum of the photon beam and electron beam rms beam sizes or divergences. Under the assumption that the FEL output is close to diffraction limited and that the FEL undulator is very long this simplifies to

$$B = \frac{4\Phi}{\lambda^2} \qquad (32)$$

then using that the relative bandwidth $\sigma_\lambda \simeq \rho$ the expression for peak spectral brightness, in units of photons/s/mm^2/mrad^2/0.1% BW, becomes

$$B \simeq 8 \times 10^9 \frac{P}{\rho\lambda}. \qquad (33)$$

For $P_{\rm rad} \simeq 10$ GW, $\rho \simeq 10^{-3}$ and $\lambda = 0.1$ nm, this gives $B \simeq 8 \times 10^{32}$ photons/s/mm^2/mrad^2/0.1% BW, exceeding that available from storage ring sources by at least eight orders of magnitude. A more detailed comparison between X-ray FEL brightness and alternative sources is given in Section 4.

2.9. Electron Beam Requirements

This section gives a brief overview of the electron beam requirements for FELs. Further details are given in [77]. As well as describing properties of the FEL output as given in Section 2.8, the FEL parameter, ρ, defines many other aspects of the system. The initial relative energy spread of the electron beam should be less than the FEL-induced modulation which increases to ρ at saturation [20], leading to the criterion

$$\frac{\sigma_E}{E} < 0.5\rho. \qquad (34)$$

From (30) and (15), to maximise the output power and minimise the gain length the FEL parameter ρ should be maximised. From (34), to minimise the degradation due to beam energy spread ρ should be maximised. It is also found that the allowed relative tolerances on many other system errors, such as undulator field errors, scale with ρ. It is clear therefore that the FEL parameter is fundamental and not just a convenient scaling parameter, and to obtain the best FEL performance, and maintain that performance in the presence of spreads or errors in system parameters, the FEL parameter should be maximised. It is convenient now to express ρ as

$$\rho \propto \frac{1}{\gamma} \left(\frac{I_{\rm peak} K^2 \lambda_u^2}{\sigma_b^2} \right)^{\frac{1}{3}} \qquad (35)$$

where σ_b is the electron beam radius. Together, the parameters γ, K and λ_u define the FEL wavelength

via the resonance condition (6) so for a specified FEL wavelength these are not free parameters. The FEL parameter is therefore maximised by increasing the peak current and reducing the transverse beam size. The beam size scales as the square root of the beam transverse emittance – this is a measure of the electron beam quality and is approximately the product of the beam size and beam divergence

$$\varepsilon_x = \sqrt{\langle x^2 \rangle \langle x'^2 \rangle - \langle xx' \rangle^2} \qquad (36)$$

where x is the horizontal offset and $x' = \mathrm{d}x/\mathrm{d}z$ is the angle of the particle trajectory relative to the axes (assuming $\langle x \rangle = \langle x' \rangle = 0$). The vertical emittance, ε_y, is defined equivalently. A small emittance is therefore required to obtain a small beam radius σ_b and maintain this small radius over a reasonable distance. It is also found that for the most efficient transverse overlap of the electrons and radiation the transverse phase space of the electron beam must be less than that of the diffraction limited photon beam giving

$$\varepsilon < \frac{\lambda_r}{4\pi}. \qquad (37)$$

This shows that the requirements on electron beam quality become increasingly stringent at shorter wavelengths.

Together the peak current, energy spread, and transverse emittance can be expressed as the electron beam brightness

$$B_e = \frac{I}{c\sigma_E \gamma^2 \varepsilon^2} \qquad (38)$$

so a high brightness beam is necessary to meet the requirements for high peak current, small energy spread and small transverse emittance [77]. It should be noted however that although a high brightness electron bunch is necessary it is not always sufficient – a bunch must be correctly configured, for example meeting (34) and (37), to be optimal.

To deliver high brightness beams to the FEL requires a high brightness electron source and a system for accelerating and manipulating the electron bunches to maintain brightness in the presence of degrading effects such as coherent synchrotron radiation (CSR) emission from dipole magnets in the beam transport system, wakefields, and micro-bunching instability. The fact that beams can be delivered with sufficient brightness for X-ray FELs to operate is testament to tremendous developments in numerous areas including low-emittance photo-injectors and CSR compensation and prevention. For the interested reader, a review of these and other technologies required for X-ray FELs is given in [17].
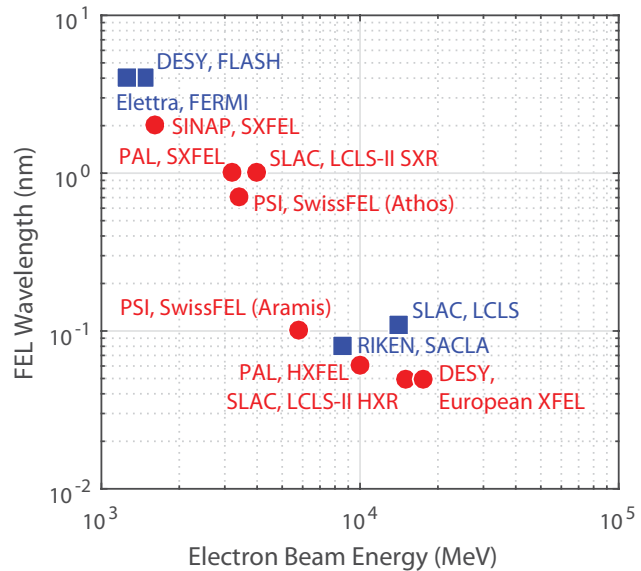

Figure 8. FEL Facilities shown by minimum output wavelength and maximum electron beam energy. Operational facilities are shown in blue and facilities under construction or funded development are shown in red.

3. FEL Projects and Advanced Techniques

3.1. A Brief Chronology of Existing Sources

There are now a number of X-ray FEL user facilities in operation worldwide. The main output parameters of these sources are given in Table 1. Figure 8 shows the minimum operating wavelength and maximum electron beam energy of existing sources (in blue) as well as FEL sources that are under construction or are funded developments (in red). This plot clearly illustrates the fact that the shorter the target photon wavelength, the greater the electron beam energy required – a consequence of the resonance condition (6). This has important consequences for the size and cost of facilities because multi-GeV beams are required for hard X-rays. Typical accelerating gradients for copper and superconducting linacs are in the range of tens MV/m so the accelerating structures themselves can be hundreds of metres long for hard X-ray FELs. Another important driver for facility size is the ablation threshold on the first beamline optic – transversely coherent multi-GW FEL pulses in the hard X-ray must propagate and diverge for tens of metres before the risk of damaging the first optic is sufficiently low (see Section 5).

This section summarises some important milestones in the rapid evolution of X-ray FEL sources. Access to short-wavelength FEL radiation for users began in 2005 with the opening of FLASH [1] at DESY, Hamburg. FLASH grew out of the Tesla Test Facil-

Name	Institute	Wavelength (nm)	Pulse Energy	Pulse Duration	Pulses/s	Energy (GeV)
FLASH [1]	DESY	4-52	10-500 μJ	50-200 fs	5000	1.25
FERMI [4]	Elettra	20-80	<30 μJ	150 fs	10	1.5
LCLS [2]	SLAC	0.1-4.6	2-6 mJ	2-100 fs	120	15
SACLA [3]	RIKEN	0.08-0.25	80-250 μJ	20-30 fs	60	8.5

Table 1. Parameters for currently operational X-ray FEL facilities.

ity (TTF) which was conceived as a demonstrator of superconducting RF cavities intended for use on the TESLA Linear Collider, and later the International Linear Collider. Due to the fact that the accelerating cavities are superconducting the thermal load is low and the accelerator can provide over 5000 electron bunches per second. A generic time structure of the FEL pulses is illustrated in Figure 9 – FLASH operates in pulsed mode where macropulses with a repetition rate of 10 Hz are comprised of 500 micropulses with a repetition rate of 1 MHz. The principle of FEL operation is SASE [41], with the milestone of first lasing demonstrated in 2000 at a wavelength of 109 nm [78]. In 2005 TTF was renamed FLASH and first user operations commenced at a wavelength of 32 nm [79]. In the intervening period significant development in beamline design, diagnostics and detectors had been carried out as required by the unprecedented peak brightness of the FEL source. Within two years, after increases in the electron beam energy, the minimum wavelength was reduced further to 6.5 nm [80].

In the USA, the first hard X-ray FEL, the LCLS at the Stanford Linear Accelerator Center (SLAC), became operational for users in 2009 [2]. Again the mode of operation was SASE. The key design goals (230 fs X-ray pulses tunable from 800 eV to 8 keV with 10^{12} photons per pulse at 8 keV) were achieved within 5 months of first lasing – a remarkable achievement and testament to the detailed planning and design work of the previous years. The LCLS is based on a 1 km section of relatively old normal conducting accelerator so thermal considerations limit the micropulse repetition rate to 120 Hz.

The following year, 2010, saw two milestones. The first was access to FEL photons in the water window when FLASH began offering 4.1 nm output [81]. The second was first lasing of the world's first seeded short-wavelength FEL facility, FERMI@Elettra in Italy [4]. In this facility a coherent laser seed was used to dominate the instrinsic noise of the output of a SASE FEL. FERMI@Elettra is based on the principle of High-Gain Harmonic Generation (HGHG) [82] in which a coherent laser seed is upconverted to a higher harmonic within the FEL, with the higher harmonic output inheriting the coherence properties of the seed laser. The principle is illustrated in Figure 10. As

expected the output pulses demonstrated superior qualities compared to SASE. They had an extended temporal coherence length with rms bandwidth 5×10^{-4}, a reduction by a factor of three from the typical SASE bandwidth (which is the ρ parameter, as discussed in Section 2.8.2), and much improved shot-to-shot relative wavelength stability of 7×10^{-5} (rms) [4].

In 2011 the world's second hard X-ray SASE FEL, SACLA at SPring-8 in Japan, achieved lasing for the first time [3]. The design of SACLA is notably different from that of LCLS with the key concepts demonstrated at the SCSS test accelerator [83] which had achieved first lasing at 49 nm in 2006 [84]. To make the facility as compact as possible the FEL undulators are placed within the vacuum. This enables the undulator gap to be significantly smaller, which in turn enables a shorter undulator period with sufficient magnetic field on axis. The LCLS undulator period is 30 mm whereas for SACLA it is only 18 mm. The smaller undulator period means, *via* the resonance condition (6), that the electron beam energy is just over half that of LCLS. The process of generating the electron bunch is also different at SACLA – instead of a photocathode electron gun where a short laser pulse is used to generate a short electron bunch *via* photoemission, the electron gun at SACLA is thermionic and uses a single crystal of CeB_6 as a cathode. This is heated and produces fairly long pulses of electrons that are transported and successively accelerated and compressed in RF cavities of increasing frequencies until final acceleration in normal conducting cavities at 5.7 GHz, twice the frequency of LCLS. The higher RF frequency allows correspondingly smaller cavities so that higher accelerating gradients can be achieved. The combination of short period in-vacuum undulators and high acceleration gradient allows the length of SACLA to be only 750 m compared to about 3 km for LCLS. A disadvantage of the lower beam energy is that the FEL pulse energy is lower – around 250 μJ compared to 6 mJ for LCLS. This is because the FEL converts a proportion of the electron beam power into X-ray power and the electron beam power is, from (30), proportional to the beam energy.

In 2012 SACLA opened for users. The same year LCLS introduced self-seeding, an idea first proposed
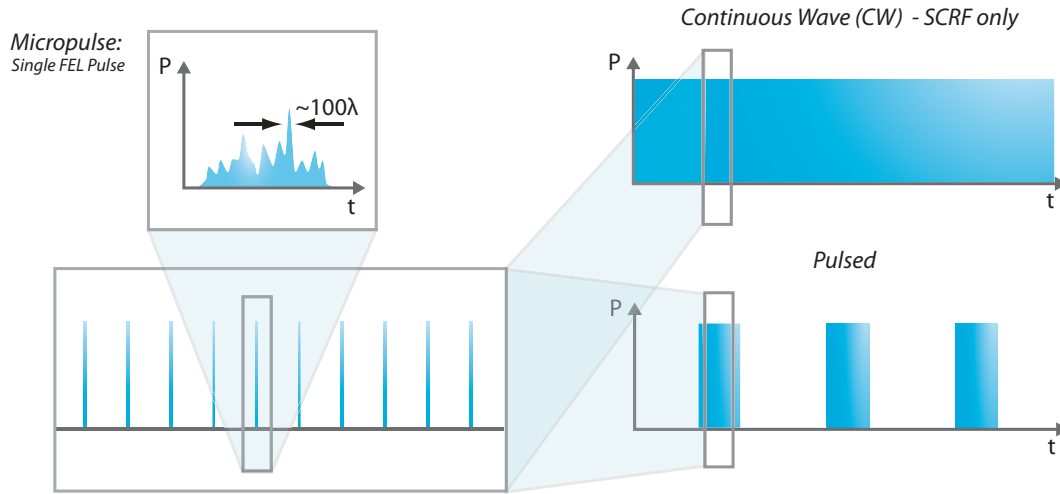
Figure 9. Generic illustration of typical FEL time structures. The individual FEL pulses are termed 'micropulses'. The illustration shows a typical micropulse from a SASE FEL where the length of each SASE spike is around 100 wavelengths. These repeat periodically at MHz repetition rates and comprise a 'macropulse'. For FELs driven by normal conducting RF (NCRF) accelerators the duration of the macropulse can be from a single micropulse up to a few μs with the macropulses repeating at typically 10-100 Hz. The thermal load on the accelerating structures limits the total number of micropulses per second. For FELs driven by superconducting RF (SCRF) accelerators the thermal load on the cavities is low so the number of pulses per second can be high – the duration of the macropulse can be from several ms in 'pulsed' mode up to effectively infinite in 'continuous wave' (CW) mode.

nearly 20 years ago [85], in the hard X-ray (HXR). Self-seeding works by spectrally filtering the noisy SASE pulse partway through the undulator, using a diamond crystal monochromator around which the electron beam is diverted in a magnetic chicane, then amplifying this filtered 'self-seed' to saturation in the remaining section of the undulator [86, 87]. The

Figure 10. Schematic of the principle of HGHG, reproduced from [82]. The top shows normal SASE in which saturation is reached in a single long undulator. In HGHG a laser seed introduces a coherent energy modulation in the first undulator, termed a Modulator, which is tuned to frequency ω. This modulation is converted into a density modulation in a magnetic chicane which has dispersion so that the path length of an electron depends on its energy. Radiation at the nth harmonic of the seed laser wavelength is generated and amplified to saturation in the Radiator undulator which is tuned to be resonant at frequency $n\omega$.

technique, illustrated in Figure 11, enabled the SASE bandwidth to be reduced by a factor of forty. Back in Europe, FERMI@Elettra opened for users operating over the wavelength range 100-20 nm and offering, for the first time in an FEL facility, full control of the output polarisation through the use of variably polarising undulators.

The capabilities of the existing sources were expanded the following year by the introduction of two-colour lasing at LCLS and FERMI and two-colour lasing and HXR self-seeding at SACLA. At LCLS, as illustrated in Figure 12, an emittance spoiling foil [89] with a double slot was combined with a delay chicane, producing two pulses with wavelengths separated by 1.9% and temporal delay of up to 40 fs [88]. The approach at FERMI was different – the FEL was seeded by two separate seed laser pulses of slightly different wavelengths. The FEL output pulses of central wavelengths 37.4 nm and 37.2 nm (tuned to the Ti $M_{2,3}$ absorption edge), thus had a wavelength separation of approximately 0.5% and the temporal delay between the two pulses, each of duration 100 fs, was controllable over 300-700 fs [91]. SACLA offered two-colour double pulses using a similar scheme to that at LCLS but with greater wavelength separation due to the wider tuning range of the variable gap undulators. Wavelength separation of 30% and temporal separation of up to 40 fs were demonstrated [90]. The scheme is illustrated in Figure 13.

In the last two years self-seeding in the soft X-ray has been introduced at LCLS [92], giving an approximate five-fold increase in spectral brightness
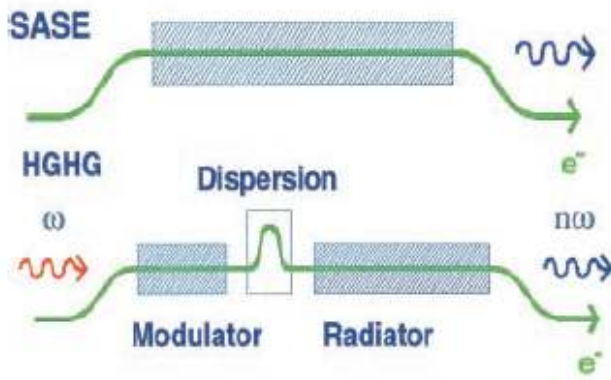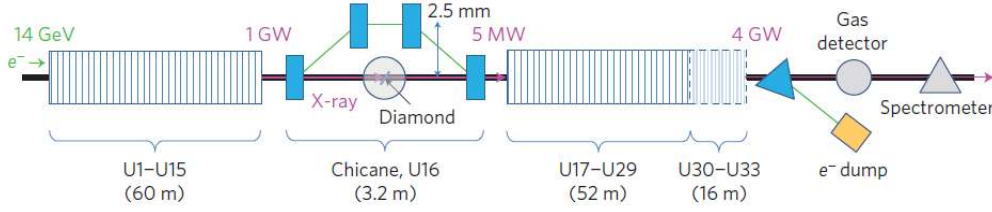
Figure 11. Schematic of the HXR self-seeding scheme implemented at LCLS, reproduced from [87]. The SASE output from the first undulator is passed through a diamond crystal creating a monochromatic wake which extends behind the pulse. The electron beam is diverted by the magnetic chicane which smooths out the microbunching already induced in the bunch while simultaneously delaying the bunch so that it then overlaps with the trailing wake. The monochromatised X-rays are amplified to saturation in the second undulator. Reproduced with permission from *Nature Photonics*, Copyright (2012) Nature Publishing Group.
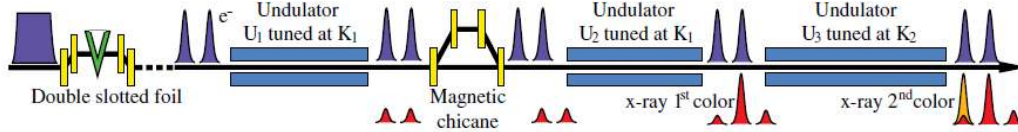
Figure 12. Schematic of the two-colour double pulse scheme at LCLS [88]. The scheme utilises an emittance spoiling foil[89] with a double slot, which creates two short regions along the electron bunch of unspoiled emittance, which are made to lase at slightly different wavelengths by adjusting the K values of the undulator sections within the limited available range. A delay chicane provides flexible temporal separation. Reproduced with permission from *Physical Review Letters*, Copyright (2013) American Institute of Physics.
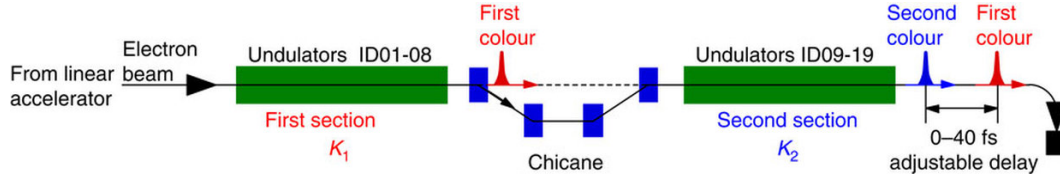
Figure 13. Schematic of two-colour double pulse scheme at SACLA [90]. The variable gap undulator sections can be tuned to widely different wavelengths. Reproduced with permission from *Nature Communications*, Copyright (2013) Nature Publishing Group.

compared to SASE, and FERMI has reached its design intensity at 4 nm [93]. At the LCLS the introduction of a variably polarising 'afterburner' undulator, installed after the planar radiator undulator section, has enabled the provision of polarised hard X-rays [94], and recently demonstrations have been made of the production of tens of gigawatt femtosecond multicolour pulses with separation up to one picosecond, three-colour pulses and two colour pulses with polarisation control of the second pulse [95]. So as of today, FEL users have access to intense X-ray photon sources of unprecedented peak power and flexibility, that cover a wide photon energy range, that can provide multiple pulses with independently variable wavelength separation and delay, and control of linewidth and polarisation.

3.2. Future Facilities

To keep up with rapidly increasing demand there are new facilities under contruction and major upgrades to existing facilities distributed across three continents. In Europe, there is SwissFEL [13] at the Paul Scherrer Institute (PSI), Switzerland, and the

European XFEL [14] at DESY, Germany. In the USA there is LCLS-II [15] at SLAC, California, and in Asia there is the Pohang Accelerator Laboratory (PAL) X-FEL [12] in South Korea and the SXFEL [96] at the Shanghai Institute of Applied Physics (SINAP), China. The main design parameters and expected dates of first lasing are given in Table 2.

The soft X-ray free-electron laser (SXFEL) at SINAP is initially being constructed as an R&D prototype for a hard X-ray FEL to explore key FEL schemes and technologies and to build up expertise. However, the expectation is that it will be upgraded to a soft X-ray user facility. The FEL will be externally seeded, operating in an HGHG configuration (as FERMI does currently). It is also proposed to use an alternative harmonic generation technique, called Echo-Enabled Harmonic Generation (EEHG) [97, 98] which compared to HGHG is potentially able to generate coherent harmonics of the seed laser to much higher harmonic number – in HGHG the bunching degrades exponentially with harmonic number k whereas for EEHG it degrades as $k^{-1/3}$. This technique may therefore enable the
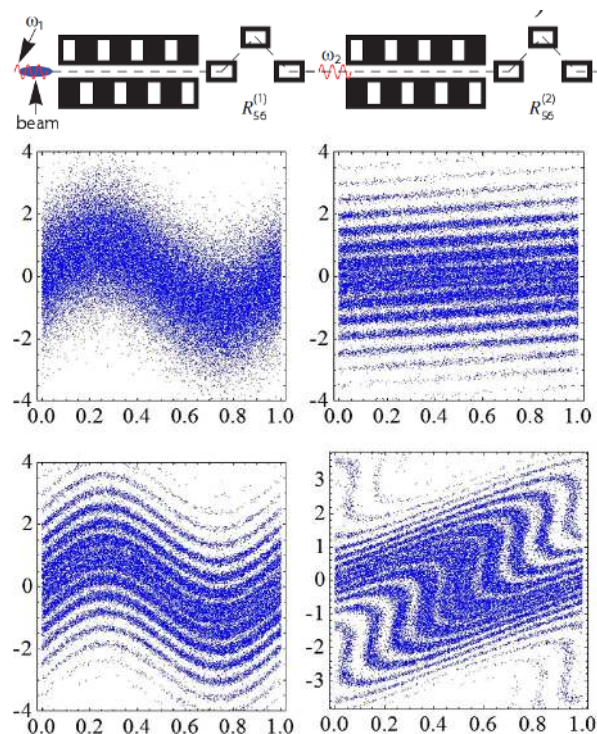
17

Figure 14. Schematic illustration of the principle of EEHG, reproduced from [97]. Top: a laser seed introduces a coherent energy modulation in the first modulator undulator. This modulation is strongly sheared in a magnetic chicane with strong dispersion. A second laser imposes another energy modulation before a second chicane converts this into a final density modulation with strong coherent bunching at some shorter wavelength which is a combined harmonic function of the wavelengths of the two lasers. Bottom: the electron bunch longitudinal phase space, with energy on the vertical axis and time on the horizontal axis, at the exit of the first modulator (top left), the exit of the first strong chicane (top right), at the exit of the second modulator (bottom left) and at the exit of the second chicane (bottom right). The strong bunching at the high harmonic is clearly visible in the final phase space where the horizontal striations visible after the first modulator have been transformed to have a significant vertical component. Reproduced with permission from *Physical Review Letters*, Copyright (2009) American Institute of Physics.

production of temporally coherent FEL pulses at shorter wavelengths than are possible with HGHG. The EEHG configuration is shown schematically in Figure 14.

The remaining facilities listed in Table 2 will operate in SASE and self-seeded modes. LCLS-II and European XFEL employ superconducting RF (SCRF) accelerators enabling many more FEL micropulses per second than facilities based on normal conducting accelerators. At LCLS-II a new SCRF linac producing CW pulses at 1 MHz will deliver high-repetition rate beam at up to 4 GeV to the SXR and HXR FELs and the existing copper linac will deliver beam at up to 15 GeV to the HXR FEL. The SCRF linac will have better energy stability than the copper linac, by a factor of

about 10, which will improve the stability of the FEL wavelength in SASE mode and the pulse energy in self-seeded mode.

It is also expected that many of the new (and existing) facilities will continue to push the boundaries of FEL performance to open up new possibilities for scientific discovery. Some of the frontiers are discussed in the following section.

3.3. FEL Technical Frontiers

The current directions of FEL development are towards: the generation of transform limited FEL pulses (where the product of the pulse duration and the bandwidth is as small as allowed by the uncertainty principle); the reduction of pulse lengths below the electron bunch length and into the attosecond regime; and the increase of output power well beyond the normal saturation level, towards terawatt FELs. New techniques often rely on precise manipulation of the electron beam by lasers (as reviewed in [99]) and/or magnets, or control of the radiation field.

In the soft X-ray, schemes such as HGHG produce pulses close to the transform limit by importing temporal coherence from a longer wavelength external seed laser then upconverting this to a higher harmonic within the FEL. This technique becomes increasingly more challenging towards the hard X-ray because of the lack of seed sources at short wavelengths. The problem is compounded by the fact that the power of the seed must increase as the wavelength decreases such that it remains sufficient to dominate the shot noise (from which SASE starts) which scales inversely with wavelength.

The EEHG scheme has the potential to reach shorter wavelengths than HGHG, due to the improved efficiency of the harmonic bunching generated in the electron beam. However, the dominant technique has become self-seeding which, as discussed above, is now widely implemented. To date self-seeding does not produce fully transform limited pulses – the output bandwidth can be reduced substantially compared to that of SASE but not to that limited by the pulse duration – and the wavelength tunability and repetition rate are constrained by the optical systems used to monochromatise the FEL radiation. Alternative proposals have been made to generate near transform limited pulses, for example by artificially increasing the slippage between radiation and electrons by delaying the electrons in magnetic chicanes inserted along the undulator [100–103]. It is possible that such schemes (due to the fact that no optics are required) offer greater ease of wavelength tunability and may be suited to high-repetition rate facilities but experimental verification is required – this is planned for example at the CLARA FEL test facility [104]

Institute	Name	Wavelength (nm)	Pulses/s	Energy (GeV)	First Lasing
SINAP	SXFEL	2–9	10	0.84–1.6	2017
PSI	SwissFEL (Athos)	0.7–7.0	100	2.5–3.4	
	SwissFEL (Aramis)	0.1–0.7	100	2.1–5.8	2016
SLAC	LCLS-II (SXR)	0.25–6.2	10^6	2.0-4.0	2019
	LCLS-II (HXR)	0.05–1.2	120	2.5–15	
PAL	XFEL (SX)	1.0–4.5	60	2.6–3.2	2016
	XFEL (HX)	0.06–0.6	60	4–10	
DESY	European XFEL (SXR)	0.4–5	27×10^3	8–17.5	2017
	European XFEL (HXR)	0.05-0.4	27×10^3	8–17.5	

Table 2. Parameters for funded new facilities and major upgrades.

currently under construction at Daresbury Laboratory in the UK.

Other proposals, such as the X-ray FEL oscillator (XFELO), use an optical cavity [105]. A design using diamond crystals in a ring configuration is predicted [106] to produce highly stable transform-limited output pulses but of modest pulse energy. The XFELO requires mirrors of relatively high reflectivity because the single pass gain is modest. A proposal for a high-gain X-ray cavity FEL has also been made [107]. However, for high gain systems the mirror reflectivity can in fact be modest [108–110] as demonstrated in 1999 [111]. It has recently been shown [112] that if the radiation feedback to the start of the undulator is very low, but just sufficient to dominate the shot noise, then it is possible to generate stable transform limited output pulses whereas if the feedback is too high the output degrades back to SASE noise. Feedback factors as low as 10^{-5} can be sufficient suggesting application of this technique may be feasible in the X-ray regime.

As discussed in Section 2.8.1, in HXR SASE the electron bunch length sets the overall radiation pulse duration which is typically a few 10s of fs. To produce few-fs SASE pulses LCLS uses few-fs electron bunches [114]. However, this duration is still thousands of optical cycles and because each SASE spike is typically a few hundred cycles ($\sim$100 as at 0.1 nm) the output still comprises multiple phase-uncorrelated spikes. This is illustrated schematically in Figure 15 (a). Since each SASE spike evolves independently, it has been proposed (for example [89, 115–118]) to pick out a single spike, with duration $\sim$100 as at 0.1 nm, either by reducing the bunch length, termed single spike SASE, or by manipulating the electron bunch such that a short section has higher quality (so preferential gain), called slicing. Some experimental progress has been made for both single spike SASE [114] and slicing *via* emittance spoiling [89, 119]. A short-pulse technique using 'chirped' electron beams (*i.e.* with a small variation in electron beam energy along the bunch) and a tapered undulator has

been demonstrated at visible wavelengths [120, 121] and could be extended to X-rays. Another idea [116] is to use a short laser pulse to pick out part of the electron beam, as shown in Figure 15 (b). In this scheme the radiation pulse is naturally synchronised to the external laser.

It is difficult to generate FEL pulses shorter than a SASE spike due to slippage. The length of a SASE spike is about πl_c, where l_c is the cooperation length (26) introduced in Section 2.8.1. For any electron bunch, or sliced section of electron bunch, shorter than this, a sustained exponential gain cannot be maintained – the light simply slips out ahead of the front of the bunch before it is amplified significantly. A possible solution may be superradiance [122, 123]. Here a short section of the bunch is seeded such that it reaches saturation before the rest of the bunch. Beyond saturation the radiation intensity increases quadratically with distance through the undulator, z, and the pulse length reduces as $z^{-1/2}$. Compared to the exponential regime, where the 'centre-of-mass' of a radiation spike is kept close to the electron longitudinal velocity due to amplification, in this mode the radiation pulse propagates closer to the speed of light. Consequently it propagates into 'fresh' electrons, provided the rest of the bunch starting from noise has not reached saturation. The technique has been demonstrated at UV wavelengths [124–127] but not yet extended towards the X-ray. Few-cycle pulses have been attained *via* superradiance in FEL oscillators, however FEL oscillators operating at X-ray wavelengths are still under development and present ideas for suitable mirror cavities have very narrow bandwidth which is incompatible with the broad-band operation required for few-cycle pulses.

There are also proposals to use external light sources to induce directly microbunching (or a single sharp current spike) over a region of only a few cycles in length before propagation into an undulator [128, 129], however the slippage has a limiting effect. Although few cycle pulses may be produced, power levels are
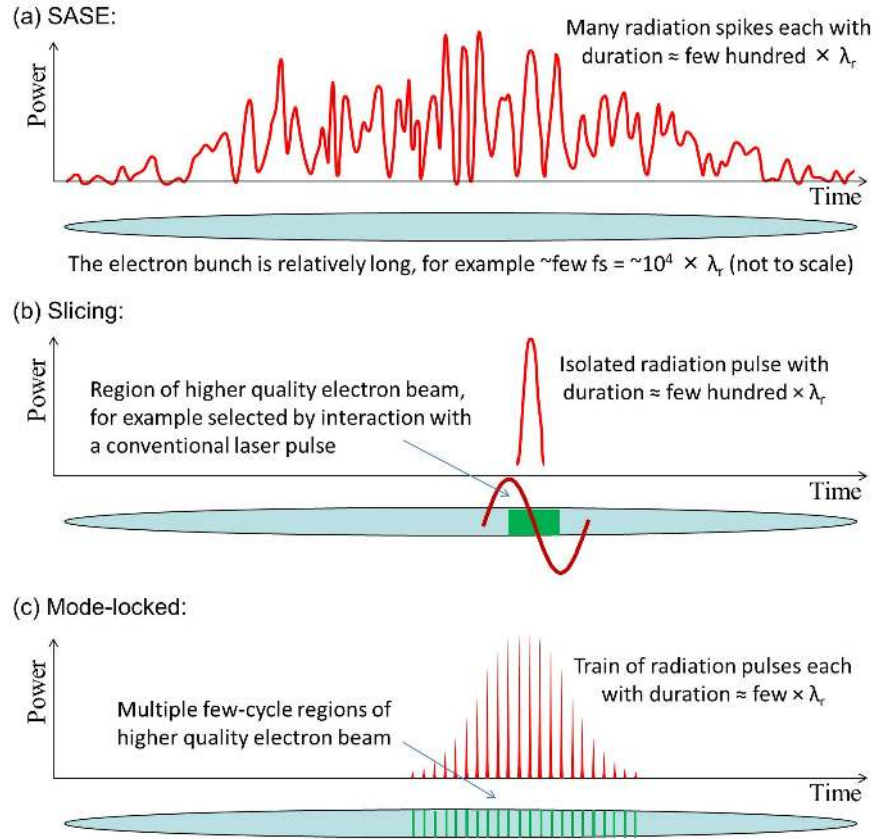
Figure 15. Illustration of different concepts for FEL operation (not to scale): (a) Typical hard x-ray SASE FEL output consists of a number of radiation spikes, each of length $\sim 2\pi l_c$ (a few hundred optical cycles, $\sim$100 as at 0.1 nm); (b) Example of proposals to 'slice' the electron bunch such that a single pulse of length $\sim 2\pi l_c$ ($\sim$100 as at 0.1 nm) is generated; (c) The mode-locked FEL concepts work by slicing the electron bunch into regions $\ll 2\pi l_c$ and periodically shifting the radiation to generate a pulse train with pulses on a similarly short scale [113]. Reproduced from *Physics Procedia* Copyright (2014) Elsevier.

predicted to be modest.

An alternative approach which is analogous to mode-locking in conventional lasers has been proposed [130]. The effect of a microscopic optical cavity is synthesised using small electron delay chicanes inserted between individual modules of a long sectional FEL undulator. Spectrally the output comprises a comb of evenly spaced phase locked modes, with overall bandwidth far greater than SASE. In the temporal domain the SASE pulse is converted into a train of phase locked spikes, each of duration much less than a SASE spike. This is illustrated schematically in Figure 15 (c). The number of cycles in each spike within the train is equal to the number of periods in each undulator module. Simulations predict pulse durations of around 20 as in the HXR. In a development of this idea [131] a mode-locked afterburner undulator/chicane system is added at the end of an existing FEL. This can then be optimised to minimise the output pulse duration without affecting the existing FEL lattice – the undulator modules in the

afterburner system can be reduced in length to only few periods, giving few-cycle output pulses. Simulations predict a train of GW peak power pulses with rms duration 700 zs. Experimental demonstration of the concept at UV wavelengths is planned at CLARA [104] in the UK.

A recent proposal for short pulse production suggested by Prat and Reiche[132] is of interest because it combines elements from many of the schemes discussed so far (superradiance, slicing with a slotted foil and electron beam delays) in a scheme that could be implemented in existing and future XFELs and may result in pulse durations of around 200 as and peak power of 1 TW.

Another likely area of development is pushing the peak FEL output power to well beyond the saturation level by using tapering (see [133] for a good overview). The theory was proposed in 1981 [39] – essentially electrons become trapped in the potential wells of the pondermotive wave and are then stably decelerated (losing their energy to the
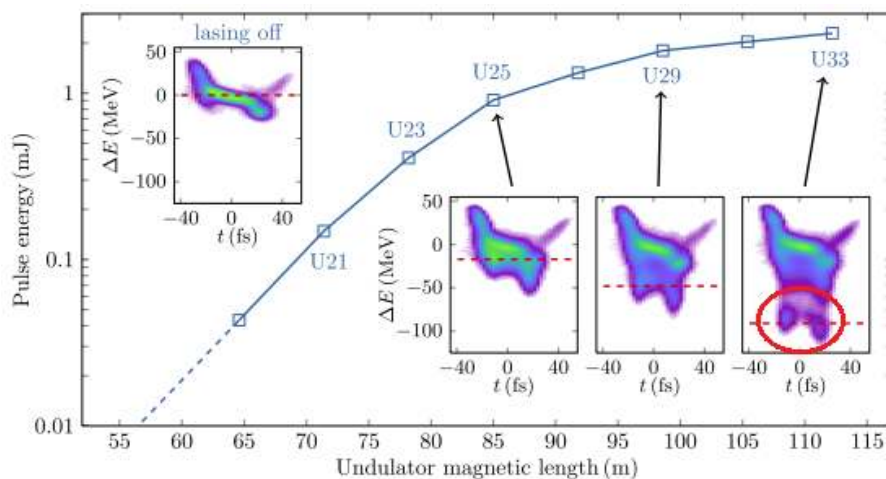
Figure 16. Experimental tapering results from LCLS, showing growth of pulse energy with distance through the undulator system. The U numbers represent individual undulator modules. The insets show the energy-time phase space of the electron bunch as resolved with a transverse deflecting RF cavity – the red circle shows where electrons have been trapped and stably decelerated by use of a taper. Figure reproduced from [133].

optical field) while the undulator K parameter is gradually reduced (tapered) to maintain the FEL resonance. Experiments on amplifier FELs at the end of the 1990s were unsuccessful due to insufficient brightness of the electron beam but experiments on LCLS in 2009 [134] demonstrated more than doubling of the output pulse energy. More recent studies with improved electron beam diagnostic techniques [133] allowed direct observation of electron trapping, as shown in Figure 16. To obtain maximum benefit from tapering the start point and the functional form of the taper must be carefully optimised. For SASE FELs each SASE spike develops independently from the random shot noise in the electron beam and so saturates at a different position along the undulator. It is therefore impossible to optimise the taper for all spikes simultaneously – in this case the increase in power over the normal saturation level is a factor of three or four, enabling a hard X-ray peak output power of approximately 100 GW. However, proposals have been made [135, 136] to use tapering together with self-seeding in which case the improved longitudinal coherence length allows the taper to be matched to the whole pulse – studies predict peak power level increases of a factor thirty or more over normal saturation opening the prospect of TW X-ray FELs.

Development is also targeted towards increasing the average power of short-wavelength FELs for industrial applications such as lithography [137–139], see Section 6.7.2. Progress is anticipated through increasing average electron beam power using SCRF linacs in energy-recovery mode [140], in combination with FEL efficiency enhancement by undulator tapering, together with increased ρ-parameter by further developments to increase electron

bunch brightness.

Reducing the FEL wavelength further to gamma-rays would allow the study of nuclear processes. However, FEL operation at such short wavelengths becomes challenging due to quantum diffusion. When an electron emits a photon it recoils due to the conservation of momentum and random recoil events due to the spontaneous emission of radiation at high photon energies can increase the electron beam energy spread and prevent FEL lasing [141]. The rate of quantum diffusion increases as γ^4 thus limiting the maximum beam energy at which sufficiently small energy spread for lasing can be maintained – this then limits the minimum feasible FEL wavelength. To push far beyond the wavelengths obtained at current facilities may require novel, very short-period undulators enabling the beam energy to be lower or lasing at a higher harmonic [142, 143].

4. Comparing FELs with Alternative Sources of High Brightness X-rays

In this Section the typical optimum photon pulse output parameters of operating high gain X-ray FELs are given. Highlighted will be differences in the pulse output between different modes of operation: SASE, as described in Section 2.8; short-pulse SASE where the bunch charge is reduced to enable the photon pulse length to be reduced while maintaining constant peak power; and self-seeding, as described in Section 3. In practice a taper in the undulator parameter (described in Section 3.3) is normally applied to optimise output power in each of these modes. A further, as yet untested, FEL scheme – XFELO [105] – is also included for comparison. After establishing the typical pulse

properties for X-ray FELs, alternative sources of high brightness X-rays will be discussed. The output properties of the full range of sources will then be compared.

4.1. X-ray FEL Photon Pulse Characteristics

The characteristics of a SASE FEL are described here in terms of the output of a single pulse. This is partly because experimental use of the output is often on a pulse-by-pulse basis. It also assists with comparisons between different FEL facilities since the number of micropulses per second between different facilities can vary by several orders of magnitude, making comparison of properties such as photons per second rather unhelpful.

As explained in Section 2.8, an intrinsic feature of a SASE FEL is the intensity and wavelength variation of the sub-structure of spikes from pulse to pulse. Because of this the exact properties of any particular photon pulse are impossible to predict and the average properties must be quoted instead.

Table 3 summarises typical photon pulse characteristics for a number of alternative X-ray FEL schemes. The exact output parameters depend upon the bunch characteristics and so only broad indicative values are given. For example, the bunch charge makes a large difference to the energy within each pulse and there is a wide variation in this parameter at user facilities (for normal SASE output the charge selected can typically vary between 100 pC and 1 nC). Similarly the short electron bunch required by the short-pulse SASE mode is only possible with low bunch charge, typically 20 pC, and hence the order-of-magnitude reduction in energy per pulse. Self-seeding narrows the bandwidth by one or two orders of magnitude. The XFELO scheme is predicted to have some quite different characteristics [106, 144]. The low energy per pulse and relatively long output pulses give relatively very low peak powers but the relative bandwidth of the radiation is so small that the peak brightness (quoted into a standard 0.1% bandwidth) is very similar to the other schemes. The repetition rate of the XFELO has to be large for the scheme to work (typically MHz) and so average outputs can be very competitive.

4.2. Alternative Sources of High Brightness X-rays

The most common accelerator source of high brightness X-rays is the high energy electron storage ring. These are facilities, typically many hundreds of meters in circumference, that store multi-GeV electrons for tens of hours. The electrons continually circulate through undulators which are installed within the ring to generate spontaneous incoherent synchrotron radiation. The electron bunch density is however insufficient for any FEL gain at X-ray wavelengths. To keep the ring circumference manageable the undulator length is limited to around 5 m but a storage ring may have tens of undulators installed, each serving a different experiment simultaneously. FELs necessarily operate with undulators typically an order of magnitude longer than this and so this advantage is also reflected in the photon output performance. There are more than 50 storage ring light sources in operation worldwide with many others being planned [145].

Two other types of high brightness X-ray source are also included for comparison with FELs. The first is an alternative particle accelerator configuration which also generates spontaneous undulator radiation, the energy recovery linac (ERL). The second is a laser based system which uses femtosecond laser pulse interaction with a target to generate high order harmonics of the fundamental laser wavelength, so-called high harmonic generation (HHG) sources. Since this source requires a laser and not a large particle accelerator, it can be hosted in a research laboratory with a much smaller-scale investment.

All of the accelerator-based X-ray sources discussed in this article are able to generate linear or circularly polarised light (or elliptical in general) by implementing undulators which manipulate the electron beam path both horizontally and vertically [50]. Such undulators are routinely installed in storage rings and have also been implemented in FELs [146]. Linearly polarised light has always been generated in HHG sources but more recently circularly polarised light has also been generated using a sophisticated scheme involving two different colour drive lasers [147, 148].

4.2.1. Storage Ring based Sources
Storage rings generate spontaneous undulator radiation across wide regions of the spectrum including X-rays. The output properties are 5 or 6 orders of magnitude lower than FELs in terms of energy and photons per pulse, and since the electron bunch length is typically of the order of 10 ps the peak flux and brightness are reduced by a further 2 or 3 orders of magnitude. Nevertheless, the number of photon pulses per second is very high due to the electron bunches continuously circulating and so the average properties of storage rings remain competitive.

A number of storage ring facilities are actively pursuing upgrades to the storage ring lattice arrangement to significantly reduce the electron beam emittance so that the emitted light is diffraction limited even at X-ray wavelengths [149]. The undulator radiation is diffraction limited when the brightness would not increase if the electron beam size and divergence were reduced further. Many storage rings are already diffraction limited in the X-ray region in the vertical

Parameter	SASE	Short-Pulse SASE	Self-Seeded	XFELO
Energy per pulse (mJ)	3	0.02	0.2-0.6	0.002
Photons per pulse	3×10^{12}	10^{10}	3×10^{11}	10^{9}
Peak Power (GW)	40-100	40	10-30	0.001 - 0.01
Peak Brightness $(ph/s/mm^2/mrad^2/0.1\% \text{ bw})$	1×10^{33} - 2×10^{34}	8×10^{33}	10^{34}-10^{35}	2×10^{32} - 2×10^{34}
Pulse Length FWHM (fs)	20 - 50	< 1	25	150 - 1500
Bandwidth (%)	0.1 to 0.2	0.1	0.005-0.01	10^{-5}-10^{-4}

Table 3. Typical maximum photon parameters for various X-ray FEL types at around 1 Å. The SASE, short-pulse low-charge SASE, and self-seeded schemes have all been demonstrated and achieved these parameters. The values given include tapering of the undulator parameter as available at present facilities, though studies predict the tapered self-seeded mode could reach TW peak power levels in future facilities [135, 136]. The as-yet untested XFELO scheme is included to show its complimentary properties.

plane but are some way from this in the horizontal plane. The upgrades therefore are largely focussed on reducing the horizontal emittance of the electron beam. These diffraction limited storage rings, sometimes called ultimate storage rings, will increase the average brightness compared to conventional rings by typically one or two orders of magnitude in the X-ray region. The pulse energy and repetition rate are largely unchanged by such an upgrade.

4.2.2. Energy Recovery Linac based Sources
ERL based light sources have been studied by several groups but have not yet been implemented in the X-ray region [140]. ERLs continually use fresh electron bunches and so the electron bunch emittance is not set by the equilibrium condition as found in storage rings. Studies have shown that diffraction limited output in the X-ray region is feasible and so an ERL based light source, which also emits spontaneous undulator radiation, has broadly similar properties to a diffraction limited storage ring. A major difference is that the electron bunches are shorter in an ERL, by typically one order of magnitude, and so the peak properties are enhanced by this amount.

4.2.3. High Harmonic Generation Sources
High Harmonic Generation (HHG) is a non-linear process in which a very intense laser is focussed onto a target that is often, but not necessarily a noble gas [150–152]. The interaction of the strong electric field of the laser with outer-shell electrons leads to the generation of a range of very high order odd harmonics of the laser wavelength. A fundamental laser wavelength of order 1 μm typically leads to the generation of light down to wavelengths of less than 10 nm. The wavelengths generated continue to get shorter as researchers refine techniques and sub nm wavelengths (*i.e.* few keV) have already been reached [153, 154]. However, most sources are limited to about 100 eV. Whilst the pulse energies are only in the 100 nJ

range in this photon energy region [155, 156], this corresponds to an impressive number of photons per pulse (of order 10^{10} in a narrow wavelength band). The number of photons per pulse beyond about 100 eV currently declines rapidly but with 1 kHz laser sources the number of photons per second can still reach beyond 10^{9} into a 1% bandwidth up to around 200 eV [157].

A key feature of HHG sources is that extremely short photon pulses can be generated. In fact the tens of attosecond photon pulse lengths generated are the shortest pulses of light available to experimentalists to date [156]. These short pulses are normally in bursts but single isolated pulses can also be generated by a number of techniques [152].

4.3. Comparison of Output Characteristics

As explained above, the specific output characteristics of X-ray sources of the same type can vary by orders of magnitude depending upon the specific implementation adopted. However, it is possible for typical values and trends to be compared. Figure 17 compares the peak brightness for the accelerator based sources only, since brightness values for HHG sources are not readily available. The X-ray FEL is around nine or ten orders of magnitude brighter than the diffraction limited storage ring due to the greater number of photons per pulse within the normalised bandwidth and the significantly shorter pulse length. FELs are another order or so brighter than conventional storage rings due to the reduction in brightness in these rings as they are not diffraction limited in the X-ray region. An ERL spontaneous source would gain an order of magnitude over diffraction limited storage rings due to the shorter bunch length.

The average brightness levels for accelerator driven sources are compared in Figure 18. The X-ray FEL advantage is reduced to a few orders of magnitude primarily because the number of bunches per second
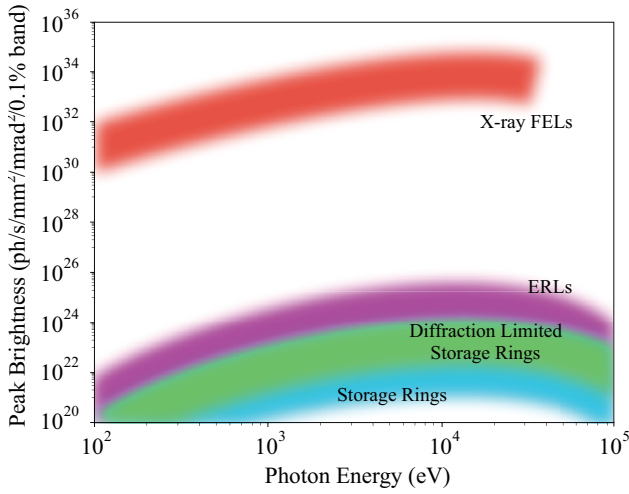
Figure 17. Typical peak brightness as a function of photon energy for accelerator driven X-ray sources.

is much higher in all the other accelerator driven schemes and the bunch length is no longer relevant. The difference between ERLs and diffraction limited storage rings is marginal as the differences in average beam current, emittance values, and undulator length tend to cancel each other out. Conventional storage rings have smaller average brightness as they are not diffraction limited in the X-ray region.
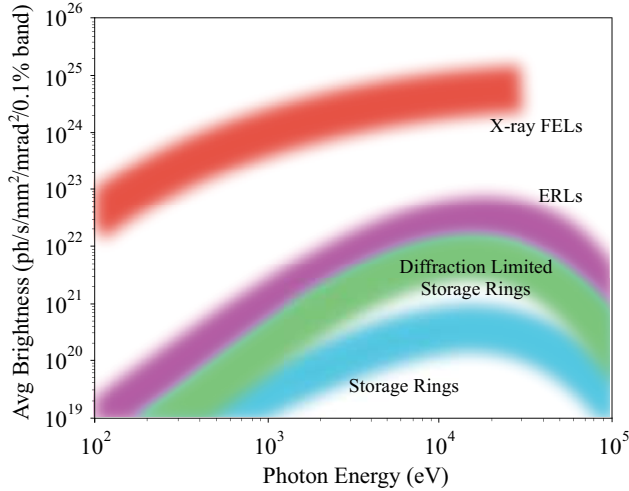
Figure 18. Typical average brightness as a function of photon energy for accelerator driven X-ray sources.

The number of photons generated per pulse into a 0.1% bandwidth is compared in Figure 19, the photon energy range plotted now starts at 10 eV to show clearly the optimum region for HHG sources. X-ray FEL pulses contain about five or six orders of magnitude more photons than storage ring sources in the angstrom wavelength region. ERLs are about an

order of magnitude below storage rings reflecting their lower electron bunch charge. HHG sources generate high photon numbers at low energies but currently this declines rapidly at soft X-ray wavelengths. Note that X-ray FELs have a steeper decline in the number of photons per pulse than other accelerator driven X-ray sources because their optimal performance is only achieved at the fundamental harmonic of the undulator whereas incoherent synchrotron radiation from higher undulator harmonics has similar output characteristics to the fundamental and so extends the high photon energy reach of storage rings and ERLs significantly.
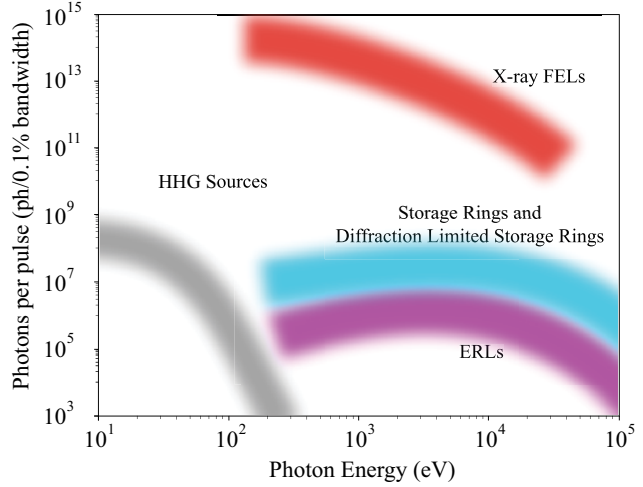
Figure 19. Typical number of photons per pulse for accelerator driven X-ray sources and also laser driven HHG sources.

5. FEL Beamlines: Optics and Diagnostics

X-ray beamline design represents the challenge of delivering high-energy photons to the experiment with a minimum of losses and perturbation of their properties. While the general concepts behind XFEL beamlines are very similar to techniques used at 3rd-generation storage rings [158], there are some crucial differences, which will be the focus of the following sections. Specific details on currently operational beamlines at SACLA [159–161], LCLS [11, 162–166], FERMI [167], FLASH [168, 169], and FLASH2 [170] can be found in the various recent references given above.

5.1. Optics

There are two fundamental XFEL photonics properties that are of relevance to the design and construction of XFEL optics. The first is that the peak intensity of the X-ray beam is extremely high, due to the large number of X-ray photons ($>10^{12}$) delivered in a very short

pulse duration (<100 fs). The second is the excellent transverse coherence of the X-ray beam [4, 171–174], which is due to the FEL lasing process. These properties are what make XFELs unique but they also place stringent requirements on the X-ray optics so as not to degrade the beam characteristics and to be resistant to damage themselves. For facilities that employ superconducting RF accelerators [1, 14, 168, 169, 175] there is the additional problem of high average photon flux, which can be several orders of magnitude above that at recent $3^{\rm rd}$-generation storage rings. This introduces a thermal load problem that is particularly significant when the pulse structure operates in a so-called 'burst mode', causing periodic changes in the thermal characteristics of the optical elements.

5.1.1. Mirrors

The general requirements for XFEL mirrors are the same as those at storage rings: to deliver the photons with as small a perturbation as possible to the photon beam while controlling its direction and spatial extent. There are several parameters specific to XFELs that make this more difficult than for synchrotron radiation. For example, due to the low source divergence of the XFEL beam, the X-ray spot size on the optical elements can often be quite small – even at significant distances from the end of the insertion devices. This, when combined with the short pulse duration, can lead to intensity effects in both the mirror coatings and substrates [176–178] and necessitates grazing-incidence operation with tight control of the mirror angle ($<10^{-6}$ rad). A further complication is that the source point for the radiation moves along the beam propagation direction when the photon energy is changed. This means that for a mirror to work over a range of photon energies it must also have a large acceptance range. Finally, to take advantage of the transverse coherence of the beam at the experiment the optic must not distort this coherence, putting even more stringent requirements on the profile of the mirror (<1 nm figure error) [179]. Note that this last requirement is also important at diffraction limited storage rings [180].

The solution for many XFEL hard X-ray optics [179] has been to use mirror substrates of quartz or silicon prepared using elastic emission machining (EEM), which uses a suspension of SiO_2 nanoparticles (0.1 mm diameter) in water flowing through a nozzle to etch away the top surface of the substrate in a controlled manner (1 nm/minute) [181]. By repeatedly measuring the surface profile of the mirror, using microstitching interferometry (MSI) [182] and relative-angle determinable-stitching interferometry (RADSI) [183], the EEM process can be precisely controlled using nozzle head positioning resulting in
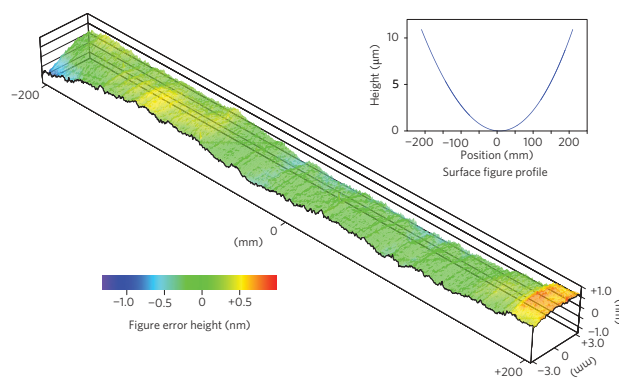

Figure 20. SACLA mirror substrate profile from [179] Reproduced with permission from *Nature Photonics*, Copyright (2013) Nature Publishing Group.

substrates with sub-nm peak-to-valley figure errors. The surface profile of a mirror in use at SACLA is shown in Figure 20. These optics can then be coated using a low-Z material, such as carbon or B_4C, which allows for a larger penetration depth of the X-rays into the coating and distributes the photon flux over a larger volume while still maintaining high reflectivity (>97%). Metal coatings can also be used to enable the use of higher grazing incidence angles, which provides a larger beam acceptance but care must be taken when using these coatings since the damage thresholds are often an order of magnitude lower than low-Z coatings [177].

5.1.2. Monochromators

In general monochromator design for XFELs is similar to that used at storage rings [158]. However the operation of these devices is somewhat different since beamlines are often required to move between monochromatic and non-monochromatic modes (so-called pink beam operation) depending on the experiment. For hard X-ray beamlines one solution to this problem has been to employ two channel-cut monochromators (CCM), where the second CCM is a reversed copy of the first, thus allowing the normal CCM transverse beam deflection to be perfectly compensated [184]. This assembly can then be removed from the beam, allowing the pink beam to follow the same path as the monochromatic beam. Other solutions include using two mirrors to mimic the beam path deviation of the two crystals in a monochromator [185].

One novel approach taken at LCLS has been to use the monochromator as a beam-sharing device where one experiment uses the monochromatic beam diffracted through the monochromator, while a second experiment uses the pink beam which is transmitted through the thin first crystal [186, 187]. This so-called

multiplexing approach allows two experiments to take place simultaneously [188], with the restriction that the X-ray photon energy cannot be changed during the measurement.

The XFELs that operate with superconducting accelerating technology and produce periodic bursts of X-rays [1, 14, 168, 169, 175] have the additional problem of varying heat load on the monochromator elements. For a facility such as the European XFEL this has required the design of liquid-He cooled artificial channel-cut monochromators, where an estimated peak power of 2000 W is produced during the burst of 2700 pulses in an interval of 0.6 ms [189].

An aspect of monochromators that should be mentioned is their effect on the X-ray pulse duration. Since monochromators generally restrict the bandwidth of the photons that pass through them, they can impact the time-bandwidth product of the pulses, stretching them in time. In general this only affects high energy resolution measurements using very short pulses but as XFEL pulse durations decrease towards the attosecond regime (see Section 3.3) this becomes more of an issue for both crystal [190–193] and grating [194] monochromators.

5.2. Photon Diagnostics

Due to the combination of machine instabilities and the stochastic mechanism behind the SASE operation of an XFEL the variation in properties from pulse to pulse can be enormous. This leads to variation in pulse energy, photon energy, pulse duration and even pulse shape for every shot, making an XFEL a very unstable source of photons. Two approaches taken to solve this problem are: a) to stimulate preferentially the FEL process using one of a variety of seeding techniques, resulting in more stable photon properties and b) to characterize fully the properties of each pulse, allowing the experimenter to filter or normalize their measurement properly. Seeding was briefly described in Section 3, here the focus is on the photon diagnostics that have been developed to provide single-shot information on XFEL pulses. Note that though the XFEL beam's transverse (spatial) coherence is an attractive property, and several techniques have been devised to measure this property pulse-to-pulse [173, 174, 195, 196], no facility has yet implemented a diagnostic that can be operated simultaneously with the experiment to enable its measurement.

5.2.1. Pulse Energy
Several devices exist to measure pulse energies shot-to-shot in a non-destructive manner. These include tools based on photoelectron generation in a gas [197, 198] and scattered X-rays from a thin film [199–201]. By using the spatial distribution of these signals it is also possible to measure the position of the X-ray beam. The absolute pulse energy can also be measured using a calorimeter [202, 203] but as this takes the full XFEL beam it cannot be used simultaneously with another experiment.

5.2.2. Photon Energy
Several single-shot spectrometers have been developed for both the soft [201] and hard [204, 205] X-ray regimes. Both LCLS [206, 207] and SACLA [208] have online hard X-ray spectrometers which use a portion of the X-ray beam for the measurement, providing pulse-to-pulse information on the variation of the SASE spectrum. SACLA has also demonstrated the ability to perform transient X-ray absorption experiments to measure the spectrum of a sample in transmission using single-shot spectrometers both before and after the sample position [209, 210]. This has the advantage of requiring no monochromator scanning but is very sensitive to differences in the spectrometer elements. For lower photon energies FLASH has developed a non-destructive photon energy monitor based on ion and electron measurements from noble gases [211].

5.2.3. Pulse Duration
XFEL pulse duration measurements are difficult [212] not only due to the ultrashort nature of the pulses but also because using standard autocorrelation techniques developed for femtosecond optical lasers are not straightforward at X-ray photon energies. There are several techniques that have been demonstrated at XFELs to provide information on the pulse duration. LCLS has installed a transverse RF deflecting cavity to measure the longitudinal electron energy profile of the spent electron bunch after it has lased [213, 214]. This tool, called the XTCAV, shows where the electron bunch has lost energy due to the lasing process, allowing the photon pulse duration to be estimated. The XTCAV has proved to be an extremely useful tool for feedback on machine operation and is routinely used at LCLS during specialized modes such as two-pulse operation [215]. Data taken using the XTCAV showing a lasing-off reference measurement and the subsequent lasing measurement for 20 pC bunch charge is shown in Figure 21. A second technique that has demonstrated the ability to measure the XFEL pulse duration is the so-called THz streaking method. In this technique the XFEL pulse generates photoelectrons from a gas jet and these photoelectrons are streaked by a single-cycle THz pulse (0.5-1 THz) that is generated by an optical laser and spatially overlapped with the X-rays. By measuring the energy of the photoelectrons using a time-of-flight spectrometer it is possible to extract several details about the X-ray pulse, such as the timing jitter between the optical laser and the X-

ray pulse [216], and the pulse duration of the X-ray pulse [217]. This streaking technique has also been demonstrated using an IR laser field [218], which has proved capable of resolving X-ray pulse durations to below 10 fs. A similar technique using laser-assisted Auger decay in Ne has also been demonstrated to be sensitive to both the X-ray pulse duration and the optical laser/X-ray jitter [219]. Finally SACLA has demonstrated a technique where they use a high-resolution spectral measurement of the SASE spikes to extract the X-ray pulse duration [220].
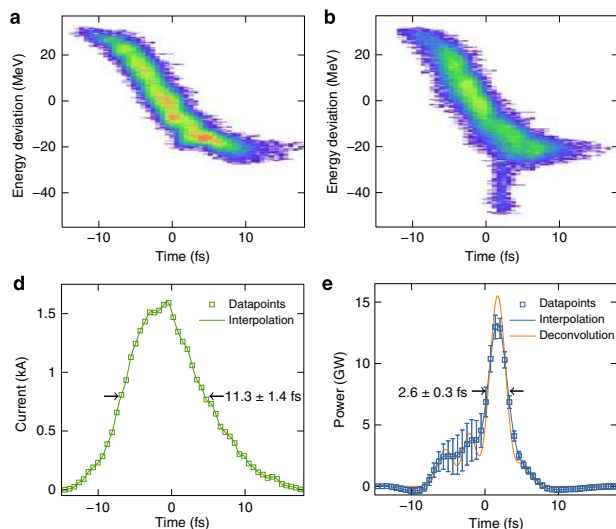
Figure 21. XTCAV data showing 2.6 fs X-ray pulse from [214] Reproduced with permission from *Nature Communications*, Copyright (2014) Nature Publishing Group.

5.2.4. X-ray Pulse Arrival Time

Due to the finite length of the electron bunch (20 fs to 1 ps), which is longer than the cooperation length of the SASE process (~1 fs), lasing can take place in multiple locations within its longitudinal extent, resulting in variance in both pulse shape and arrival time shot-to-shot. This can be seen in Figure 21 where the lasing process has taken place in a 2.6 fs section around the middle of the approximately 15 fs electron bunch. The XFEL photon pulse arrival time with respect to the optical laser excitation (pump) pulse is also determined by the electron beam timing, which is dictated by the synchronisation and stability of FEL facility components including the photocathode laser system and RF linacs [221]. This includes via energy-jitter converting to time-jitter in the magnetic elements of the bunch compression and transport [17]. The combined result is an XFEL photon pulse arrival-time jitter of up to several hundred femtoseconds, pulse-to-pulse, though this can be improved by using all-optical synchronization techniques across the facility [222,

223]. This timing jitter has a significant impact on pump-probe experiments where control over the time delay between an optical laser and the X-ray pulse is crucial. One approach to avoiding this problem is to use an optical laser to seed the FEL using high harmonics of the optical laser (high gain harmonic generation, HGHG) which is possible at XUV to soft X-ray photon energies. This technique, which has been implemented at FERMI [4, 224, 225], uses the same laser as both the experimental pump source and FEL seed resulting in <10 fs jitter between pump and probe [226]. Several techniques have been developed to measure the relative arrival times between laser and X-ray pulses, allowing data to be corrected using this information. One example is the THz streaking tool which was described in the previous section [216], which has the advantage that it works through the entire soft to hard X-ray ranges. LCLS has implemented two tools, one used at the hard X-ray instruments (spectral encoding) and one at the soft X-ray instruments (spatial encoding). The spectral encoding tool [227] uses a chirped white light pulse, generated by the optical laser to probe the change in reflectivity of a thin membrane of Si_3N_4 caused by its transmission of the X-ray pulse. The result is a decrease in the transmission of the white light at a specific wavelength, which can be directly correlated to the time-delay between the optical laser and X-rays if the chirp of the probe is well-characterized. The spatial encoding technique [228, 229] uses the tilt angle between the laser pulse and the X-ray pulse to map the relative arrival time between the two pulses onto the spatial profile of the optical laser beam. Both tools have been tested against each other and against a time-resolved diffraction signal from a Bi crystal, demonstrating their ability to correct time-resolved signals down to <50 fs [230]. A schematic of the setup used at LCLS for this measurement is shown in Figure 22. Subsequent improvements have even demonstrated the ability to reach <1 fs using 10 fs optical pulses [231]. The SACLA facility has recently introduced a combined spectral/timing jitter photon diagnostic [208], allowing them to measure the relative timing jitter between laser and X-rays to ~50 fs using a spatial encoding technique.

6. Photon Science

6.1. Structural Biology

The discovery that radiation damage can be 'out-run' by using a sufficiently brief (femtosecond) X-ray pulse [232] (and a much larger dose therefore delivered, producing more intense Bragg spots without damage) addresses one of the fundamental constraints of X-ray crystallography, and so has created exciting new
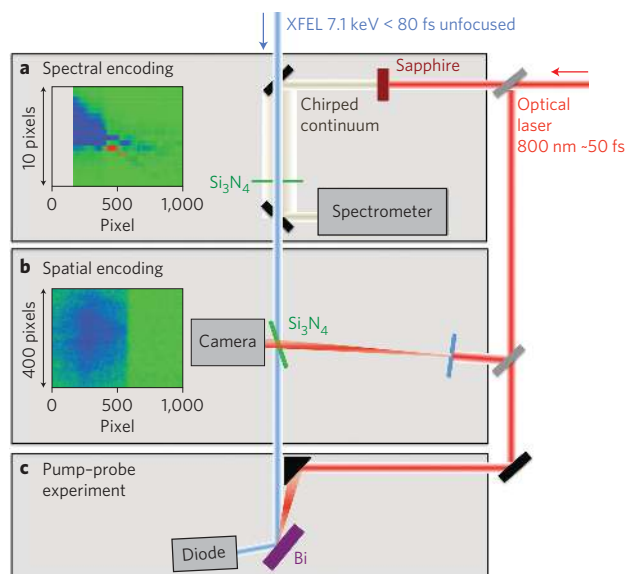
Figure 22. LCLS Timing tools schematic from [230] (Reproduced with permission from *Nature Photonics*, Copyright (2013) Copyright Nature Publishing Group).

opportunities for protein crystallography and the study of dynamics at room temperature. Structural Biology therefore has been a high profile activity on FELs since the first results appeared in 2009 [233]. In this 'diffract-before-destroy' process, following the production of a Bragg diffraction pattern in the first few tens of femtoseconds, the cascade of ejected photoelectrons from the extremely intense X-ray laser pulse vaporises the crystal, so that this is a 'destructive readout' method. The field has been extensively reviewed [11, 234–238]. An up-to-date overview is contained in the articles included in the write-up of the 'Biology with free-electron X-ray lasers' discussion meeting, organised by Spence and Chapman, contained in a special issue of the Philosophical Transactions of the Royal Society [239].

6.1.1. Protein Structure and Dynamics
Several new techniques have been developed for both static and time-resolved diffraction studies of proteins at XFELs, as shown in Figure 23. These include snapshot (femtosecond) fast solution scattering (FSS) or fast wide-angle X-ray scattering (WAXS), single-particle (SP) diffraction (with one particle, such as a single virus, per X-ray shot) and the study of 2D protein crystals. For SP imaging, in particular, it was appreciated that the challenges were immense, since even a virus as large as the mimivirus (about 0.3 μm in diameter) scatters only a few million soft X-rays when hit with the 10^{12} photons provided in each pulse from LCLS at SLAC. These pulses, with durations from 10 to 200 fs, are generated at 120 Hz, and the resulting

diffraction patterns are read out at the same rate, producing very large data sets. The beam diameters available at LCLS vary between a few microns and 0.2 microns. For crystallography, the intensity at the peak of a Bragg spot is proportional to the sixth power of the number of molecules on a side of the crystal, so even a $10 \times 10 \times 10$ protein nanocrystal produces a million times more scattered intensity at such a peak than one of its molecules. This accounts for the fact that the first successes in biology at XFELs have been in X-ray nanocrystallography, known as serial femtosecond crystallography, or SFX. It is found that resolution depends on pulse duration, and that near-atomic resolution can be obtained from crystals with 40 fs pulses or shorter [240].

Well before the first hard X-ray FEL was operational, both preliminary experimental developments and work on new algorithms were underway at various national laboratories, universities and X-ray FEL facilities. The SFX method and the first sample delivery systems, in which a stream of protein nanocrystals in random orientations runs in single file across the beam, was developed experimentally at Arizona State University and later tested at the Advanced Light Source in Berkeley [242]. A goniometer is not used, so that computer algorithms must be used to determine the crystal orientations and provide indexing, in order to merge at a later date thousands of shots. The underlying theory for protein nanocrystal diffraction at XFELs was first described in detail by Kirian *et al.* [243]. For single particles, the image reconstruction process involves two steps firstly determination of the orientation of the particles from the continuous 'diffuse' X-ray scattering of each of them (and merging of the data into a three-dimensional diffraction volume), followed by solution of the phase problem, and inversion to a three-dimensional single-particle charge-density map. This problem, which has built on earlier work in the field of coherent diffractive (lensless) imaging (CDI) forms the basis of a large literature, reviewed in Millane *et al.* [244], Hawkes and Spence [245] and Marchesini [246]. Software packages are now available to perform this analysis [247]. Two recent successful approaches are described in detail in Hosseinizadeh *et al.* [248] (manifold embedding) and Ayyer *et al.* [249] (expectation maximization and compression).

Since the times for molecular processes in biology are generally long (*e.g.* microseconds or longer) due to entropic and other factors, the femtosecond pulses of the XFEL are mainly used to outrun damage, rather than to provide high time resolution (this may nevertheless be needed in the study of fast processes triggered by light, such as the response of the eye (rhodopsin) or photosynthesis). Otherwise, this 'diffract-and-destroy' mode allows proteins to
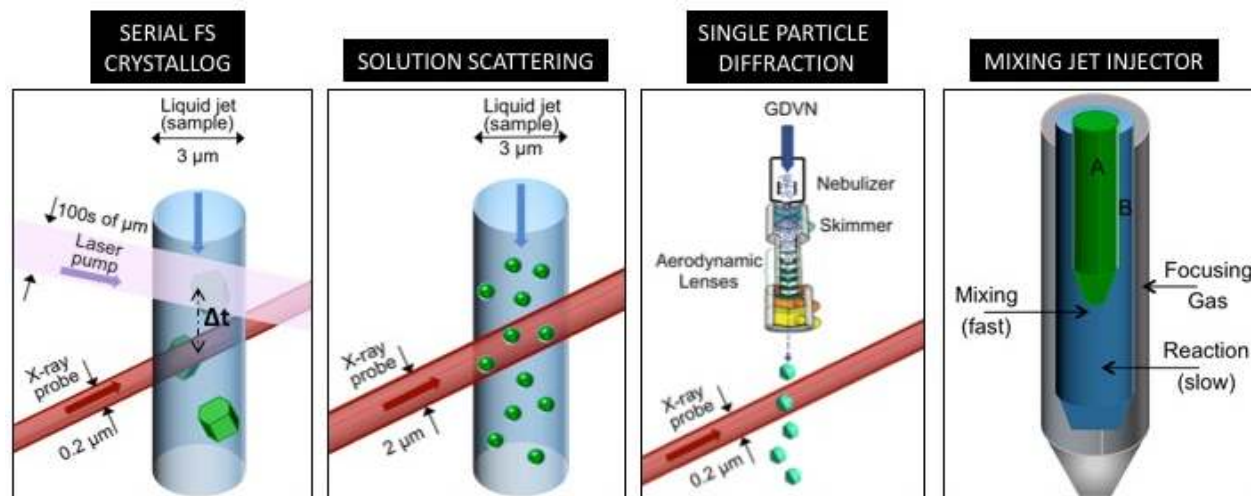
Figure 23. Sample-delivery modes for structural biology at XFELs. Time-resolved variants of these modes are also possible using pump-probe or mixing-jet methods. For time-resolved pump-probe crystallography, a gas-dynamic virtual nozzle is commonly used (GDVN) [241].

be studied at room temperature before damage, rather than at the low temperatures (which may introduce artifacts) used at synchrotrons to minimize radiation damage. The European XFEL therefore provides an important opportunity to study time-resolved protein dynamics at room temperature, with the correct physiological driving forces and energies available. Other situations in which the use of an XFEL may be preferred include: (i) Proteins which readily form showers of nanocrystals but for which it may take months or years to determine the chemical conditions to grow crystals large enough for conventional crystallography. Nanocrystals are readily fed to the beam as a suspension in various liquids, such as the lipidic cubic phase (LCP) used for membrane proteins. (ii) For the study of protein dynamics such as enzyme reactions, substrate and enzyme nanocrystals may be mixed in the sample delivery device, allowed to react for a measured time, then injected in a stream across the beam [250]. The small size of the crystals (about one micron) allows 'diffusive mixing' of substrate through the nanocrystal water channels in a time of tens of microseconds, much shorter than the chemical reaction time. Crystals small enough for diffusive mixing cannot be handled at synchrotrons, yet produce strong diffraction patterns at an XFEL. Each setting of reaction time (at which thousands of diffraction patterns are collected in random crystal orientations) then provides one frame of a 3D movie of the reaction. There may be more than one reaction pathway progressing among the molecules of the crystal. The response of the beta-lactamase enzyme to a small drug molecule (used against tuberculosis) has recently been studied in this way [251]. (iii). The

use of nanocrystals also facilitates optical pump-probe studies, since the size of these crystals is comparable with the absorption length of the pump light, so that the crystal may be fully saturated with pump light [252]. Studies of metalloprotein enzymes are reviewed in Kern *et al.* [253].

For SFX when using a liquid host medium and a gas-dynamic virtual nozzle (GDVN), the typical jet speed is very fast, perhaps 10 m/s, with micron-sized droplets passing at about 1 MHz, so that only one nanocrystal in every four thousand is hit by the beam, resulting in much wasted protein. The GDVN uses a coaxial sheath of faster-moving gas to speed up, and hence narrow, the liquid stream after emerging from a nozzle sufficiently large to avoid clogging. It later breaks up, according to Rayleigh's theory, into a droplet stream [254]. The droplets then form into a single-file beam of perfectly spherical micron-sized spheres, which eventually freeze by evaporative cooling at about 10^6 °C/s. A large reduction in the amount of sample required can be achieved by reducing the speed of the jet, either by using higher viscosity host liquids (forming a 'toothpaste' jet) or by injecting much larger droplets than can be synchronized with the FEL pulses. ('On-demand' droplet formation, perhaps with one virus or nanocrystal in each droplet, is not possible with droplets smaller than about 30 micron diameter.) This has raised the possibility of delivering nanocrystals in the same viscous medium, namely Lipidic Cubic Phase, in which they are grown, thus addressing the important problem of how to make nanocrystals for XFEL work and greatly reducing the amount of protein needed. Membrane proteins are well suited to growth in LCP and there have now

been several structures of these solved at XFELs (see, for example Zhang *et al.* [255] for angiotensin, and drugs related to control of blood pressure). The LCP injection device [256] has now also been used at many synchrotrons, so that new structures are now being reported using serial crystallography for submicron crystals at synchrotrons [257], in the absence of a goniometer. In this viscous medium, sample rotation during the millisecond exposure times possible using the new detectors now available at synchrotrons, is negligible. Other viscous fluids have been used to accommodate both soluble and membrane proteins, including agarose [258] and mineral oil (grease) [259]. This approach was used to obtain the structures of lysozyme, glucose isomerase, thaumatin and fatty acid-binding protein type 3 at a resolution of better than 2 Å. The relative merits of the various jet approaches have been reviewed by Weierstall [260]. The LCLS is typically focused to a spot of approx. 5 μm in diameter (FWHM) and, for hard X-rays, delivers about $7x10^{10}$ photons μm^{-2} in the centre of the beam (assuming a Gaussian profile). Studies to date have used photons of around 8 keV, however the upper limit of beam energy has also allowed selenium SAD (single-wavelength anomalous dispersion) phasing at 12.6 keV. An illustration of one continuous-jet sample-delivery method, based on electrospinning, is shown in Figure 24 [261].

A second alternative approach is to fire the FEL beam at microcrystals held on a solid support which is scanned across the beam ('fixed targets'). Such as a Micro-Liquid Enclosure Array (MLEA) which can, for example, hold samples in solution behind silicon nitride windows or exposed to a humid atmosphere [262–265]. Depending on the X-ray background levels required, these may or may not be used in vacuum, where liquids freeze by evaporative cooling. This 2D array of perhaps 50×50 such windows must then be raster scanned across the beam (which cannot be moved) at high speed (for example matching the 120 Hz repetition rate of the LCLS) as the beam destroys each sample in turn, releasing water to freeze in the vacuum. (The focused LCLS beam immediately drills a hole in stainless steel sheet metal.) Robots may need to be designed to fill and encapsulate these cells. Future XFELs will operate at kHz camera-readout speeds, providing challenges for the design of both viscous jets and scanned fixed-target systems. The rate of particle delivery in the GDVN, when free-running (*i.e.* not driven by piezo oscillator) is about 1 MHz, exactly matching the European XFEL repetition rate, which will open at DESY (Hamburg Germany) in 2017. However camera read-out speeds are expected to be about 20 kHz. It seems likely that stage-scanning will be possible at a few kHz speeds, with accurate (nm) beam positioning on few-micron

sized crystals, thus providing higher hit rates than jets but smaller data sets. Robotic loading and liquid sealing of cells against background are issues yet to be fully resolved, except in the case of the 'Road-runner' system[262].

Structural reports have included studies on; Photosystem-I [233], photosytem II [266, 267], G protein-coupled receptors [268, 269], photoactive yellow protein [252, 270] and rhodopsin-arrestin complexes [271, 272]. Additional reviews of this area include, for example, those by Patterson [273], Spence [235], Fromme and Spence [274], and Neutze [275].

Whilst the majority of X-ray crystal structure determinations give a static (*i.e.* time and spatially averaged) picture of the system under study, SFX using pump-probe techniques allows dynamical information to be obtained. A review of approaches to time-resolved diffraction using XFELs can be found in [276]. Key dynamical processes may be probed over timescales of femtoseconds to microseconds.

Several dynamical studies upon large biomolecules have been reported since the first pump-probe study, on Photosystem I ferredoxin [277]. Most recently, remarkable density maps of the cis-trans transformation in Photoactive Yellow Protein (PYP) have been captured as a movie at 100 fs time resolution (out to 3 picoseconds) and 0.16 nm spatial resolution [252], a process that is akin to the first event in the detection of light by the human eye. The time-resolved density maps obtained for this process are shown in Figure 25. This was done using the GDVN liquid injection system with laser pumping synchronized with the X-ray pulses to record snapshot diffraction patterns alternately from illuminated and un-illuminated protein nanocrystals. Laser illumination, simulating the effect of sunlight on a plant or organism, causes a small change in structure factors, which can be phased by the molecular replacement method, to produce a difference electron density (DED) map between the bright and dark states. Since each crystal is destroyed in turn, the bright and dark data are collected from successive nanocrystals of different size, complicating scaling in data analysis (see below). Thousands of diffraction patterns must be collected for each pump-probe delay, which provide one frame of a 3D movie. The photocycle includes several stable intermediate molecular species, and two reaction paths in the nanocrystals, whose appearance and disappearance, described by rate equations, can by extracted from the data by single-valued decomposition (SVD). This project followed earlier work on the same system over a longer time interval using the same method [270]. A second example can be found in the lower-resolution
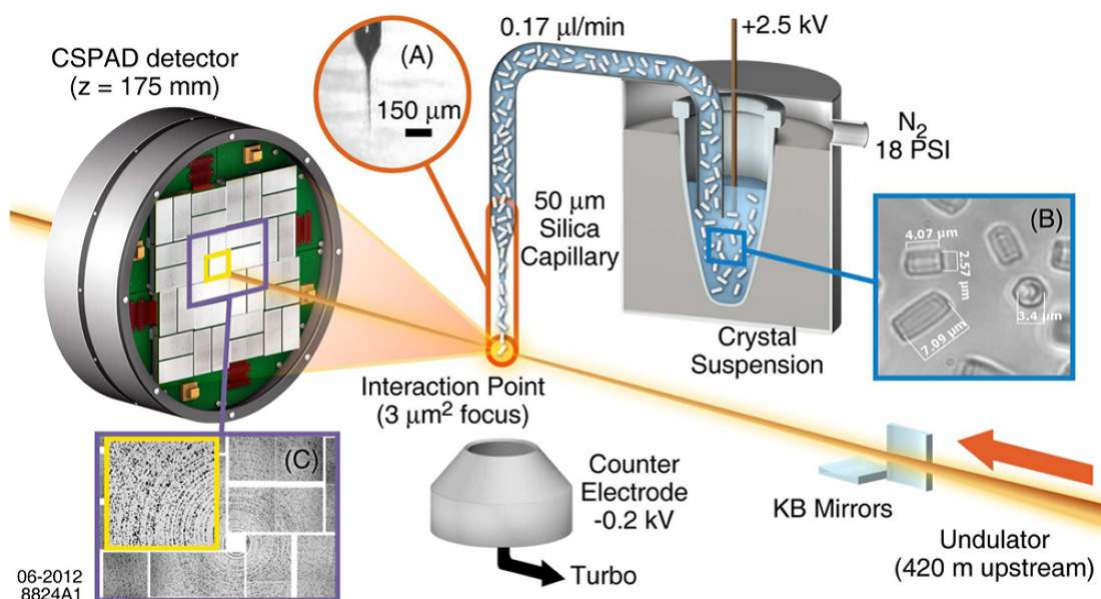
Figure 24. Schematic experimental arrangement of the electrospinning sample delivery system [261]. LCP viscous jets and the GDVN liquid jet system used for time-resolved diffraction are similar but use different host media and feed systems.

study of the important Photosystem II macromolecule, responsible (with Photosystem I) for photosynthesis in all green plants, and hence for life on earth. Contained within Photosystem-II is the so-called oxygen-evolving complex (OEC) at which the photolysis of water occurs *via* a series of photon pumped redox reactions. By determining the structure of Photosystem-II (PS-II) in the dark state (S_0 state) and then after double laser excitation (supposed S_3 state) structural changes in the Mn_4CaO_5 cluster at the core of the OEC and in electron acceptor areas of the protein have been established [266]. This XFEL pump-probe approach to the study of photosynthesis becomes even more powerful when the X-ray snapshots are combined with X-ray emission spectra from the heavy atoms present (Mn), which can provide information on the oxidation state of these atoms at each point in the cycle [278].

Data analysis for SFX is the subject of an extensive literature. Because of the large fluctuations in XFEL intensity from shot-to-shot, the large variations in nanocrystal size, and the chance variations in diffraction conditions (orientation) for each shot, the earliest publications used the so-called Monte-Carlo method [243]. The SASE mode of operation is essentially amplified noise (see Section 2.8) and is therefore not optimal for crystallography. At the same time, integrating detectors optimized for the large dynamic range needed were not available. In the Monte-Carlo method a simple average is taken over stochastic variations in all experimental parameters, which are very difficult to characterize accurately and

may have to include such things as variations in sample to detector distance, background due to stray X-ray scattering, readout noise and pixel saturation. The resulting error in structure factor measurement then falls off inversely as the square root of the number of shots, with a certain proportionality constant K. Detector metrology proved particularly difficult, requiring accurate measurement of the position of each pixel with respect to the flying samples with near micron accuracy. The 'partially problem' is the subject of many papers: a single shot provides only a thin slice of the Ewald sphere through the angular range over which a crystal diffracts around any Bragg condition (the rocking curve), whereas an angular integration over this is required to provide a structure factor. With a large data set in the Monte-Carlo approach, there is likely to be a good sampling of crystal orientations around any particular Bragg condition (each from an individual nanocrystal of distinct size) so that the sum of these will provide the wanted angular integration across the rocking curve. A summary of all these issues, describing the incremental progress that has been made on all of them (resulting in a large reduction in the value of K over the past seven years), can be found in Sauter [279], Oghbaey *et al.* [265] and White *et al.* [280], this latter also describes a leading software package for SFX data analysis. This reduction in K has meant that new structures have now been solved at XFELs using a few thousand patterns, in favourable cases, which can be collected in minutes. Most current algorithms start with a
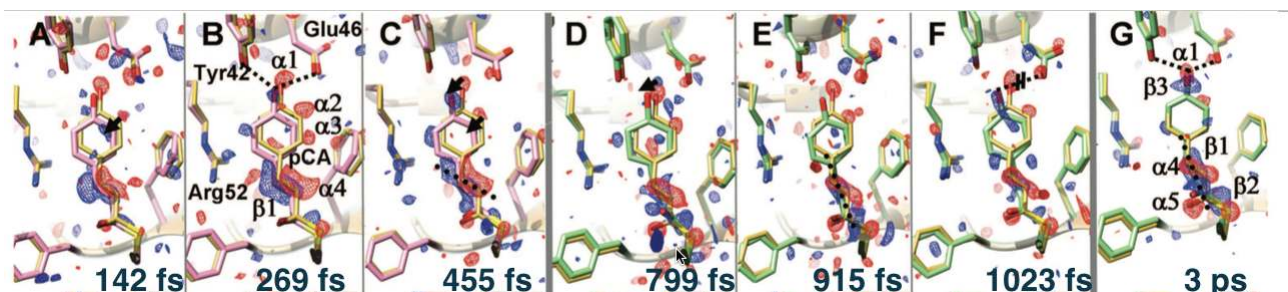
Figure 25. Trans- to cis-isomerization in PYP. Weighted DED maps in red (-3σ) and in blue (3σ). The reference structure is given in yellow; structures before the transition and still in the excited state are in pink, those after the transition and thus in the ground state are in green. Important negative DED features are denoted α, important positive features are dentoted β. Pronounced changes are emphasised by arrows. A-C) Time-delays before the transition. Dotted line: direction of C2=C3 double bond feature near β1. Dashed lines: hydrogen bonds of the ring hydroxyl to Glu46 and Tyr42. B) Chromophore configuration from 100 to 400 fs pump-probe delay. D) Chromophore configuration at 799 fs after transition. E-F) Chromophore configuration at longer times from 800-1200 fs. G) 3 ps chromophore configuration; dotted line near β1: direction of C2=C3 double bond [252]. Reproduced with permission from *Science*, Copyright (2016) The American Association for the Advancement of Science.

Monte-Carlo average, then use iterative optimization to refine further the experimental parameters. In practice, data analysis is normally done in two stages. During acquisition, software such as Cheetah [281] is used to discard blank shots and identify good hits containing an indexable number of Bragg spots, correct detector artifacts, subtract background and generate a virtual powder pattern (the sum of all good patterns, showing Debye-Scherrer rings) for a quick indication of data quality, resolution, and possibly to assist with indexing, generate statistics on hit rate and resolution, and convert the cleaned output to a standard file format such as HDF5.

Of general interest and physiological relevance, myoglobin and some of its derivatives have been actively studied at the LCLS [282, 283]. Building on a large foundation of structural and spectroscopic investigations built up over a number of years by a wide range of groups, Levantino and co-workers have used visible pump/X-ray probe solution-scattering techniques, with pulses in the fs regime and a time range of 50 fs to 100 ps, to reveal details of the initial structural rearrangements of CO-myoglobin upon photolysis. Using green laser pump pulses in a nearly co-linear geometry with LCLS X-ray probe pulses, structural changes were monitored by a combination of Fe K-edge XANES [283] and small and wide angle X-ray scattering [282]. The time-resolved Fe K-edge XANES [283] measurements following photolysis revealed structural changes on two timescales, one fast (70 fs) the other rather slower (400 fs). The fast rearrangement was tentatively attributed to photolysis of the haeme-CO bond and the start of haeme doming. The slower rearrangement was assigned to further motion of the Fe centre out of the haeme plane towards the proximal histidine (see Figure 26) coupled with myoglobin F-helix displacement. The small and wide

angle X-ray scattering study (pump beam 250 fs at 538 nm and 0.3 nJ mm^{-2}; probe beam 30 fs at 9 keV) revealed direct evidence for an increase in the myoglobin radius of gyration followed by protein expansion. The expansion was preceded by a change in the mass distribution of the protein and its timescale (complete in 1 ps) was consistent with a so-called proteinquake [284]. Oscillations in the radius of gyration and the volume, with a 3.6 ps period, were observed indicating the importance of underdamped low frequency vibrations in proteins. Portions of the molecule involved in the collective motion are highlighted in red in Figure 27. They include the haem, helix F which is bound to the haem, and parts of helices A, C, E, G and H.

Remarkable results from the photosynthetic reaction centre have also been obtained by the method of fast solution scattering (FSS) at LCLS by the Neutze group [285]. In their study of the 'quake' motion by which photosynthetic proteins absorb the very large amount of energy ($>>$ kT) provided by solar photons, and which must be dissipated without unfolding the protein, it was found possible to separate the heating contribution from the atomic motions and to assign time constants to each. This fast solution scattering study of a protein of known structure achieved picosecond time resolution at about 0.4 nm spatial resolution.

6.1.2. Live Cell Studies

The SACLA facility has been used to generate coherent diffraction patterns from multiple 2μl samples of living *Microbacterium lacticum* cells [286]. It must be appreciated that single-particle data can only be merged if the particles destroyed by each shot were identical. Each shot, providing one projection at limited resolution to synthesize a high resolution image in three dimensions, requires a huge data set
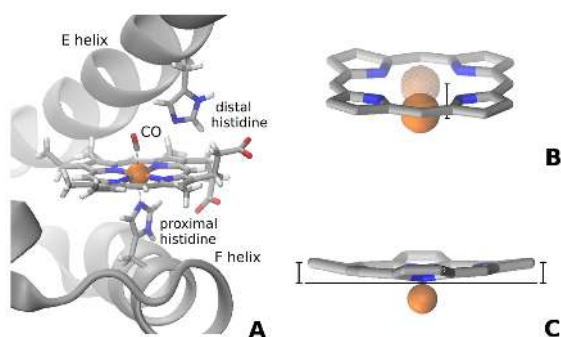
Figure 26. Schematic of the active site of CO-myoglobin showing, in blue, the four in-plane N atoms of the porphyrin and the N atom of the proximal histidine. The remaining coordination site is occupied by the CO which is bonded to the iron atom *via* the carbon atom [283]. Reproduced with permission from *Structural Dynamics*, Copyright (2015) American Crystallographic Association, Inc.
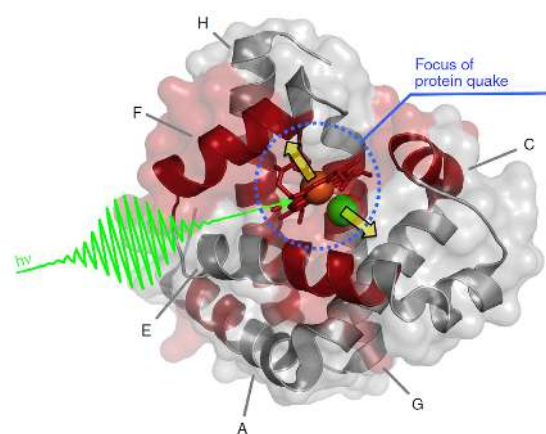

Figure 27. Schematic representation of the 3D stucture of carboxymyoglobin indicating the haem, amino acid helices and the focus of the protein quake [282]. Reproduced from *Nature Communications*, Open Access Nature Publishing Group.

from identical particles, for which DNA provides a prescription in many cases. While it would be highly desirable to image whole cells in 3D, since they all differ slightly no method has yet been developed to merge single-cell diffraction data without loss of resolution. Here, 5.5 keV photons were focused to a 1.5 μm $\times$ 2.0 μm spot on the sample, the repetition rate was 10 Hz, the pulse duration was approximately 10 fs and the average pulse energy (after the undulator) was 260 μJ. After averaging 119 similar data sets, image reconstruction involved first refining the rectangular support area using the relaxed averaged alternating reflection method (RAAR) [287] with shrinkwrap [288] (2,000 steps) and then using the noise-tolerant hybrid input-output method (HIO) [289] with the fixed support (1000 steps). This resulted in the image of a rod shaped cell, see Figure 28, of approx.
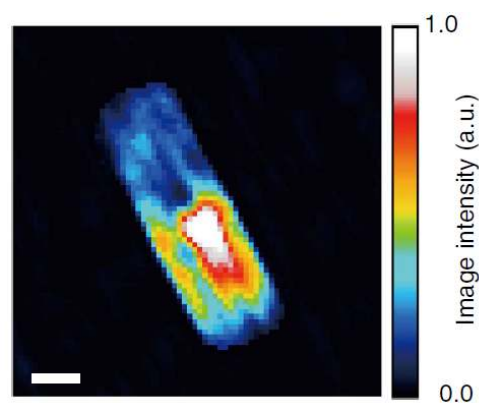
Figure 28. Reconstructed image of a living *Microbacterium lacticum* cell. Linear scale with the white scale bar is equal to 100 nm. [286]. Reproduced from *Nature Communications*, Open Access Nature Publishing Group

570 nm by 194 nm. Notably, as shown in the Figure, some of the cells internal structure was visualised *without* the benefit of staining. The upper, low image density (shades of blue), part of the cell structure was attributed to mainly proteins. The lower, high image density (white, red and orange), part was attributed to mainly nucleic acids [286]. Live cyanobacteria have been imaged using LCLS [290, 291]. By comparison, cryo-electron SP microscopy, while providing excellent single-particle images also merged from many copies (with dramatically improved resolution to between 0.2 and 0.3 nm when using the new direct-electron detectors) is normally limited by the onset of multiple scattering to bioparticles (embedded in vitreous ice) smaller than about 0.05 microns. (More limited information is available by a different method TEM electron tomography – from thicker samples, such as the edges of a flattened cell or a virus.) The ability to image much larger structures than is possible by cryo-electron microscopy (due to the greater penetrating power of X-rays) is a potential advantage of the XFEL SP method.

In-vivo crystallography has recently been performed with the LCLS FEL beam [292]. The study involved diffraction from Cry3A toxin crystals within cells of *Bacillus thuringiensis*. Structural information at 2.9 Å resolution was obtained and the structure of the crystalline protein as found in the living cell was established to be essentially the same as that of the extracted and recrystallised material.

6.1.3. Heterogeneous, Non-Crystalline Cell Organelle
In studies demonstrating the feasibility of obtaining and analysing data on heterogeneous, non-crystalline samples Hantke *et al.* [293, 294] have reported imaging carboxysomes from *Halothiobacillus neapolitanus*. These particular organelles have a mean diameter of
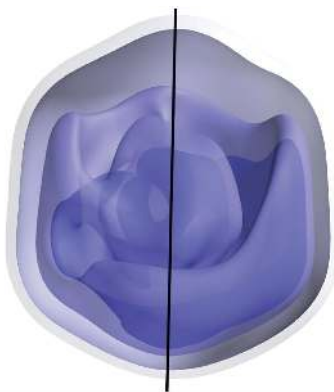
33

Figure 29. Reconstructed electron density of the mimivirus (full-period resolution 125 nm). A pseudo-fivefold axis is indicated with the vertical black line and the internal structure is clearly non-uniform. The isosurfaces are white (lower density) to blue (higher density) [296]. Reproduced with permission from *Physical Review Letters*, Copyright (2015) American Physical Society

115 ± 25 nm and a roughly icosahedral shape. Data analyses were complicated by both the distribution of carboxysome sizes and their random orientation with respect to the photon pulses. The high-throughput sample delivery enabled close to 70,000 diffraction patterns to be obtained in 12 minutes of beamtime, followed by automated analysis.

6.1.4. Viruses
Because their similarity may allow merging of large data sets, viruses have been of interest to FEL scientists for some time [295] however it was only in early 2015 that the first example of a 3D structure was obtained [296]. Based on electron microscopy evidence, it is generally believed that while the virus capsids and protein coating of all examples of a particular icosahedral virus may be identical, the packing of the genome inside the capsid may differ between instances of the same virus. In this study an aerosol of mimivirus (*Acanthamoeba polyphaga*, mimivirus) particles were focused to a narrow stream and crossed with pulse trains from the LCLS [296]. Diffraction data were used to retrieve both the photon fluences appropriate for the interactions and the relative orientations of the particles. Retrieval was achieved using a modified version of the EMC (expand, modify and compress) algorithm [297, 298]. Though at low resolution, primarily due to the small number of diffraction patterns processed, the study clearly showed that the internal structure was asymmetric, see Figure 29.

Since the above report, data have been obtained on other samples, *e.g.* Sinbis virus [299] and Rice Dwarf virus [300].

6.1.5. Looking to the Future
The technique of SFX is at an active stage of development and has yielded an impressive array of results so far, to the point where new groups can submit beamtime proposals to the existing XFEL facilities in Japan and USA (soon Germany, Switzerland and South Korea) and expect to obtain data with the help only of the local staff scientists. The NSF's Science and Technology consortium of seven universities ('BioXFEL') exists to provide education, some support for beamtime and the development of new ideas in the field, including data analysis and sample delivery (https://www.bioxfel.org), and may be contacted by scientists entering the field. In the future SFX will benefit from an increase in pulse repetition rate as proposed for the European XFEL and LCLS-II, and the additional XFEL facilities nearing completion in Switzerland and Korea. There is some evidence of greater resolution from XFEL SFX data than from synchrotron data on similar crystals, however this issue requires careful systematic study. Much work is needed to develop sample delivery methods to operate at kHz speeds, and to better characterize all the experimental parameters in SFX in order to take more accurate account of the degree of partiality in each reflection recorded.

We can also expect the maturation of all the experimental modes shown in Figure 23, and their time-resolved variants (*e.g.* TR-SP). The method of time-resolved fast solution scattering (TR-FSS, *e.g.* Arnlund *et al.* 2014 [285]) for structures previously solved at high resolution by crystallography in their ground state, in combination with lattice dynamics simulations, appears to have a strong future. There has been a considerable effort to extend this work on snapshot WAXS patterns (FSS) to the anisotropic patterns which are expected from XFELs because the 'exposure time' is much less than the rotational diffusion time for the molecules in solution. (This anisotropy is clear if we consider the pattern to be expected from, say, three randomly oriented particles per shot but the anisotropy persists for very large numbers of identical particles per shot.) Even if we ignore coherent interparticle interference, the resulting FSS patterns develop two-dimensional structure, which has now been seen experimentally for inorganic samples [301, 302]. Kam proposed long ago that these patterns could be analysed using angular correlation functions (see Kirian [302] for a review and discussion of the best number of particles per shot) and this has now been demonstrated in several cases [303–305]. It will be clear that reconstruction to a 3D density map from 2D FSS patterns is preferable to present efforts for 3D reconstruction from one-dimenionsal SAXS and WAXS patterns. We are also

certain to see an explosion of papers using a wide variety of methods for triggering reactions beyond optical pumping and chemical mixing, including light and pH triggered release of caged molecules, temperature pulses, and terahertz pumping (which couples to water dipoles in the hydration shell). The methods of optogenetics [306] allow mutants to be made from important proteins which are light-sensitive. For single particles, the least mature of the methods, recent work with viruses at LCLS has shown scattering out to about 0.5 nm in individual shots, however the hit rates (typically 1 percent or less) with the best current system (electrospray source driving aerodynamic stack) are too low to provide enough data for a three-dimensional reconstruction. Thus hit rate, background, and the 'plating-out' of precipitates and salts onto the particles (causing them to differ in size, preventing merging of data) during the drying phase in the aerodynamic stack are the current limiting experimental problems. Otherwise, resolution improves with number of shots, which effectively increases the dynamic range. However, X-ray scattering from a dielectric sphere falls off as the inverse fourth power of the scattering angle, a severe penalty against higher resolution. For Poisson noise processes under the Monte Carlo averaging process, 100 times more data are needed to add one significant figure. In addition, resolution after merging and 3D reconstruction is significantly worse than in individual shots, indicating the difficulty in accurately sorting continuous diffraction patterns (with Friedel symmetry) into orientation classes, and in distinguishing small changes in orientation from changes in conformation or particle shape – a problem successfully tackled in the cryo-EM community [307].

Given the cellular sub-structure already hinted at in Figure 28, time-resolved X-ray imaging of cells has the potential to reveal information on genome replication and cell division [286] once these experimental issues are addressed. For viruses too large to be imaged by cryo-EM this will be a fertile field of endeavour, particularly as key algorithms mature. Potential primary targets include HIV, influenza and herpes viruses [296]. The extension of the mixing-jet ('mix-and-inject') method (which, because it uses nanocrystals, can provide time-resolved atomic resolution images) to all the enzymes, providing time-resolved imaging at the molecules level of enzyme mechanisms, and a method of structural enzymology, is a particularly exciting prospect [251].

6.2. Atomic, Molecular and Cluster Physics

The ultrashort, intense, high-energy photon pulses available at FELs have led to a number of – now classic – studies on atoms, molecules and clusters.

Experiments on FLASH at DESY led the way with pioneering work on, for example, coulomb explosion of clusters [308], multiphoton ionization of noble gases [309, 310] and time-dependent studies of atoms and molecules using traditional laser/FEL pump-probe techniques. With first lasing of LCLS and more recently SACLA these early experiments have been revisited and pushed to higher photon energies, shorter pulse durations and larger systems.

Atomic and molecular work on short-wavelength FELs has been the focus of a number of recent reviews, for example work at FLASH is reviewed in [5], that at LCLS can be found in [10, 311] and that at SCSS and SACLA are covered in [8].

6.2.1. Atoms

Multiphoton processes in atoms in the EUV to X-ray regimes have been investigated extensively at all the short-wavelength FEL facilities. The main motivation for these studies has been to reveal the pathways of multiphoton multiple ionization that have been newly enabled by the availability of intense pulses in the EUV to X-ray regimes. Some of this work is reviewed below.

A few-photon absorption leading to single ionization of helium atoms may be the simplest single-color multiphoton process that can be well compared with theory. At SCSS, Hishikawa *et al.* [312] investigated a few-photon single ionization of He employing a magnetic bottle electron spectrometer (MBES). The photon energy was ~24 eV and the FEL power density was ~10^{13} W/cm^2. Under these conditions one electron was promoted to the Rydberg manifold by single photon absorption and at the same time another electron was promoted to the Rydberg manifold by two-photon absorption. As a result, three-photon single ionization *via* autoionization of the doubly excited states was anomalously enhanced. Ma *et al.* [313] investigated two-photon single ionization of He in the photon energy range between 20 and 24 eV, at SCSS by velocity map imaging electron spectroscopy (VMIES), and discussed the coexistence of resonant versus direct two-photon ionization pathways following theoretical predictions [314]. At FERMI 3, Zitnik *et al.* [315] investigated two-photon excitation of even-parity doubly excited autoionizing states, taking advantage of a very narrow photon bandwidth of fully coherent FEL pulses.

FERMI can not only provide longitudinally-coherent single-colour pulses but also phase-coherent two-colour pulses. This characteristic feature of FERMI has brought a new aspect to the investigation of two-photon processes, *i.e.*, coherent control of two-photon ionization. The Ne atom can be ionized by an intense pulse at 20 eV *via* resonant two-photon ionization. Adding a weak 40 eV pulse with an intense 20 eV pulse, Prince *et al.* [316] showed that the

asymmetry of the photoelectron angular distribution of Ne can be controlled to a temporal resolution of 3 as by adjusting the relative phase of the two-colour pulses. This work demonstrated that a fully coherent FEL can not only open new pathways of multiphoton processes but can also be used to coherently control the processes.

In the photon energy range $20-24$ eV available at SCSS, another process that could be fully analyzed and intensively studied was three-photon double ionization of argon [317–320]. In this photon energy range, single photon ionization of Ar first takes place followed by two-photon ionization of Ar^+. Hikosaka *et al.* [318] investigated by MBES the role of an intermediate resonance in the two-photon ionization of Ar^+. Gryzlova *et al.* [320] have studied the role of doubly excited autoionizing states in Ar^+ populated *via* two-photon absorption of the ionic ground state of Ar^+ by VMIES and ab initio theory calculations.

At SCSS, at 24 eV and with a FEL power density $\sim 10^{14}$ W/cm^2, formation of Ar^{7+} and Kr^{8+} was found [321]. The total energies required to remove seven electrons from the Ar atom and eight electrons from the Kr atom are ~ 434 eV and ~ 508 eV, respectively, *i.e.* more than 18 and 21 times the photon energy of 24 eV. Such multiple ionization is likely to be due to sequential stripping of the outermost electrons [322]. With this assumption, the total numbers of photons absorbed by single Ar and Kr atoms should be 22 and 26, respectively. Details of these multi-photon multiple-ionization pathways, however, have not been fully analysed.

At FLASH, at a photon energy 44 eV, Kurka *et al.* [323, 324] performed a kinematically complete experiment for sequential two-photon double ionization of neon atoms, by measuring the momenta of both electrons in coincidence with Ne^{2+} ions. A reaction microscope was used and the process fully characterized. At the higher photon energy of 93 eV, Rouzée *et al.* [325] identified sequential three-photon triple ionization of Ne with VMIES. For Xe, a photon energy of 93 eV coincides with a giant resonance, where the 4d subshell photoionization cross section is hugely enhanced. Ion spectrometry by Sorokin *et al.* [326] evidenced the formation of Xe^{21+}. Though it is clear that multiple cycles of 4d photoionization and subsequent Auger decay play a role in multiphoton multiple ionization of Xe *via* the giant resonance, it is still under the debate whether collective effects play a role [310, 327, 328].

The first experiment performed at LCLS [2] was multiphoton multiple ionization of Ne using ~ 2 keV photon energy and at $\sim 10^{18}$ W/cm^2 power density. By measuring the ions produced, Young *et al.* [329] demonstrated that all ten electrons of Ne were stripped

away *via* multiple cycles of inner-shell photoionization and Auger decay. Young *et al.* also noted that rapid photo-ejection of inner-shell electrons produced hollow atoms (which result after both 1s electrons have been ejected and before the core holes can be filled by Auger decay) and an intensity-induced X-ray transparency. Importantly, inner-shell lifetimes change as the photon pulse progresses.

The electron dynamics of hollow Ne atom formation has been revealed in great detail using the technique of partial covariance mapping [330] further details of which can be found at the following locations [331, 332]. This experimental work was undertaken at the Atomic, Molecular and Optical science instrument at the LCLS. Electron energy spectra recorded shot-by-shot from over 480,000 X-ray pulses (of photon energy 1062 eV, nominal duration 8 fs and pulse energy 0.11 mJ) were analysed to reveal the presence of correlations. The interactions result in a range of single-photon absorption, sequential multi-photon absorption and decay processes, examples of which are shown in Figure 30. In this figure, and
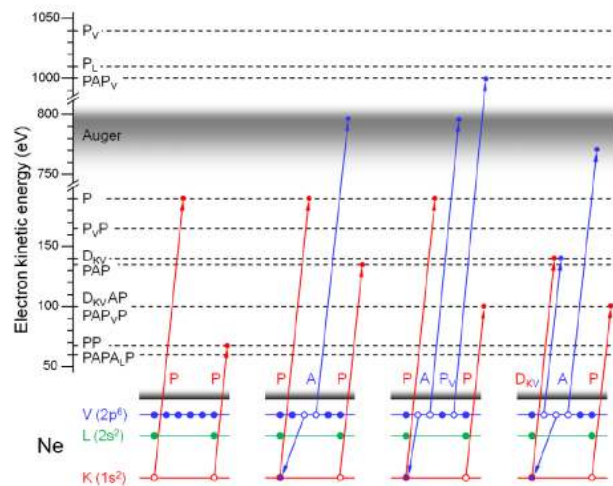

Figure 30. Ne ionization processes following X-ray FEL photon absorption. [330]. Reproduced from *Physical Review Letters*, Open Access American Physical Society.

in Figures 31 and 32; P indicates core electron emission, P_L indicates inner-valence shell emission and P_V indicates valence shell emission. A and A_L are valence and inner-valence shell electron emission, respectively, following filling of a core hole, *i.e.* in the Auger process. D_{KV} is core electron stimulated valence electron emission.

The maps reveal a range of phenomena. For example;

a) The rise in intensity towards the ends of the D_{KV} line in Figure 32 shows that the two emitted electrons tend to share the available energy unequally.

b) The presence of non-linear sequences that lead

to the same final state and the competition between them on the fs timescale, notably $P_V P$ and PP_V are separate as are $PAP_V P$ and $PAPP_V$.

The full Ne partial covariance map together with conventional 1D electron energy spectra (along the x and y axes) are depicted in Figure 31. The main (core) Ne photoelectron line is clearly visible labelled (j) in the 1D electron energy spectra, however, region (a) of Figure 31 reveals that it has several components; note this region is magnified and replotted in 3D on the LHS in Figure 32.
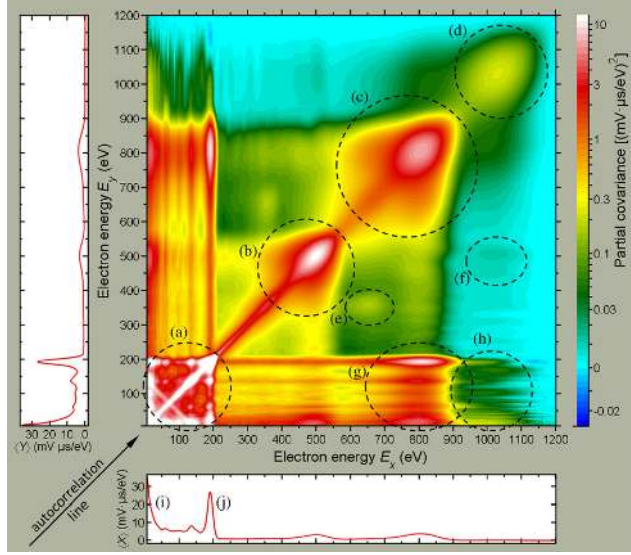
Figure 31. Ne ionization processes following X-ray FEL photon absorption. [330]. Regions (a) to (h) correspond to the following ionization sequences: (a) Ne core-core; (b) H_2O core-core, core-Auger and Auger-Auger; (c) Ne Auger-Auger; (d) Ne valence-valence; (e) N_2 core-Auger; (f) H_2O core-valence; (g) Ne core-Auger and (h) Ne core-valence. Peak (i) is the result of electrons arising from electrode surfaces within the apparatus. Peak (j) is the main (core) Ne photoelectron line. Reproduced from *Physical Review Letters*, Open Access American Physical Society.

Analysis of the yields (from integrated volumes) of double core hole (DCH) covariance features, for example *PP*, *PPA* and *PAP*, (in Figure 32) together with estimates of the shot-to-shot maximum pulse duration (see Section 2.8 on SASE FEL pulse structures) shows that core ionization followed by Auger-process filling of the core vacancy, *PA*, is relatively unaffected by the pulse duration whereas *PP*-based processes become increasingly probable as the pulse length is shortened. The variation of yields with X-ray pulse energy was also investigated.

Rudek *et al.* [333] measured ion and fluorescence yields for Xe at photon energies of 1.5 and 2 keV, and found that production of highly charged ions, up to 36+, was significantly enhanced at the lower photon energy. The results also differed from theoretical
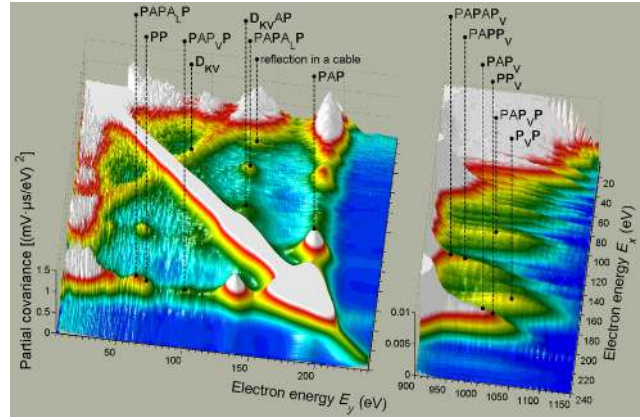
Figure 32. Core-core (left) and core-valence (right) correlation regions showing Ne ionization processes [330]. The notation is given in the text. The top of the autocorrelation line (top left to bottom right of the left hand image) has been removed to show the high value areas behind. Reproduced from *Physical Review Letters*, Open Access American Physical Society.

predictions available at that time. The discrepancy was attributed to the resonance-enabled X-ray multiple ionization (REXMI) mechanism neglected in the theory. Later, an improved simulation [334] taking account of REXMI well-reproduced this surprising experimental result.

These early LCLS experiments were, however, limited to photon energies below 2 keV due to the optical design of the AMO end station. SACLA provides hard X-rays above 5 keV and one of the first experiments there was also multiphoton multiple ionization of Xe. Fukuzawa *et al.* [335] observed *via* ion spectrometry the production of high charge states of Xe, up to 26+, at ∼5.5 keV photon energy, with power density of ∼10^{16} W/cm^2 and pulse width of ∼10 fs. Such high charge states can be produced by five cycles, or more, of L-shell photoionization and subsequent Auger cascades. In spite of the very demanding task of dealing with so many configurations, theory succeeded in reproducing the observed charge distributions fairly well, and at the least semi-quantitatively.

At SACLA, at the highest photon energy (15 keV) ever achieved [336], double core hole formation (and thus X-ray transparency) was identified in Kr by detecting hypersatellites in the X-ray fluorescence spectra.

Investigations of multiphoton multiple ionization of atoms at high photon energies opened up by LCLS and SACLA have received broad interest in connection with electronic radiation damage in X-ray imaging. Indeed the above described investigations provided benchmarks for theoretical attempts to describe charge densities of atoms irradiated by very intense X-ray pulses. It should also be noted that photon energies and fluences used for the SACLA experiments were

those commonly used for coherent X-ray imaging at the same facility.

6.2.2. Molecules

The intense FEL pulses strip off so many electrons from an isolated atom (as seen in the previous section) that one can readily imagine that exposure of an isolated molecule to such a pulse leads to a violent Coulomb explosion. Here, the main questions are how fast the charges are accumulated then distributed over the molecule, and how fast the molecular dynamics sets in. Again only a subset of the literature will be briefly reviewed.

At SCSS, using a photon energy of 24 eV and a power density close to 10^{14} W/cm^2, Yamada *et al.* [337] found Coulomb breakup of N_2 to $N^{m+}-N^{n+}$ and of O_2 to $O^{m+}-O^{n+}$ (with $m + n$ up to 5) by employing momentum-resolved ion-ion coincidence. At this photon energy, each ionization step except the first one needs absorption of 2 to 3 photons. To reach the 5+ charge state, 10 photons should be absorbed. Yamada *et al.* suggested that electrons were emitted sequentially in competition with the elongation of the bond length, based on the charge-state dependence of the kinetic energy release distributions.

At FLASH, using 44 eV photons, and a power density of $\sim 10^{13}$ W/cm^2, Jiang *et al.* [338] performed momentum-resolved ion-ion coincidence measurements. At this photon energy each multiple ionization step of N_2 and O_2 discussed above mostly requires absorption of only a single photon. Under these conditions Jiang *et al.* fully characterized few-photon sequential ionization pathways. At the higher photon energy of 91 eV, Kornilov *et al.* [339] observed Coulomb break up of N_2 up to $N^{4+}-N^{5+}$ by combining single shot time-of-flight ion spectrometry with partial covariance mapping of two ions. They also performed classical trajectory simulations with a sequential ionization model taking account of the temporal evolution of the Coulomb breakup and reproducing well the observed ion-pair ratios and kinetic energy releases for each ion-pair production. Here, the key parameters were the FEL intensity ($\sim 10^{14}$ W/cm^2) and the duration of the FEL pulse (~ 100 fs), which determine the number of ionization sequences that occur in competition with Coulomb breakup of the molecule. The 91 eV photon energy is close to the giant resonance of iodine-containing molecules, where the I 4d subshell photoionization cross section is enhanced. At this photon energy, Kornilov *et al.* [339] also observed Coulomb breakup of I_2 up to $I^{8+}-I^{9+}$. This highest-charge channel was unexpected when only sequential ionization processes from the ground state ions were considered.

Work at FLASH has also revealed interesting,

ultrafast, photo-fragmentation dynamics when using XUV pulses as both pump and probe [340]. Using a split mirror and a 38 eV photon beam Jiang *et al.* probed the dissociation channels of acetylene (HCCH) and obtained data supporting the importance of sequential two-photon absorption as the principal double-ionization mechanism but with branching ratios significantly different from those obtained in synchrotron studies.

Extending investigations into the X-ray range generated a renewal of interest in multiphoton multiple ionization of molecules, partly in connection with radiation damage during exposure of targets to XFEL pulses. At LCLS, the investigations with photon energies up to 2 keV indeed revealed novel phenomena intrinsic to high energy photons. Using N_2 as a target, Hoener *et al.* [341] found a molecular mechanism of frustrated absorption that suppresses the formation of high charge states at short pulse duration. This observation highlights the benefit of very short FEL pulse for X-ray 'imaging before destruction' of targets. Fang *et al.* [342] investigated competition between inner-shell photoionization, Auger cycles and molecular dissociation in N_2, where the Auger lifetime gave an internal clock to elucidate the time scale of Coulomb breakup.

Double core-hole creation in molecules [342, 343] has received attention in part because of its potential application to chemical analysis [344–346]. X-ray two-photon photoelectron spectroscopy and partial covariance mapping of two core-level photoelectrons have been used to investigate double core-hole states of some small molecules and this has provided a proof-of-principle confirmation for the high sensitivity of double core-hole spectroscopy to the chemical environments of specific two atomic sites whose core electrons have been ejected [311, 347–350]. That DCH spectroscopy provides a sensitive test of chemical environment has implications for single-pulse imaging of biomolecules described above as well as on work on solids described below.

Another LCLS experiment to be noted is that by Erk *et al.* [351] who investigated ionization and fragmentation of methylselenol (CH$_3$SeH) molecules by intense ($\sim 10^{17}$ W/cm^2), very brief (5 fs) X-ray pulses at 2 keV, using momentum-resolved ion coincidence techniques. They noted signatures of ultrafast charge redistributions from the inner-shell ionized Se atom to the entire molecule together with significant displacements of atoms in the course of multiple ionization *via* Auger cascades *in spite* of the briefness of the X-ray pulses.

Investigations have been extended further into the hard X-ray regime at SACLA. For example, at 5.5 keV photon energy with a power density of $\sim 10^{17}$ W/cm^2
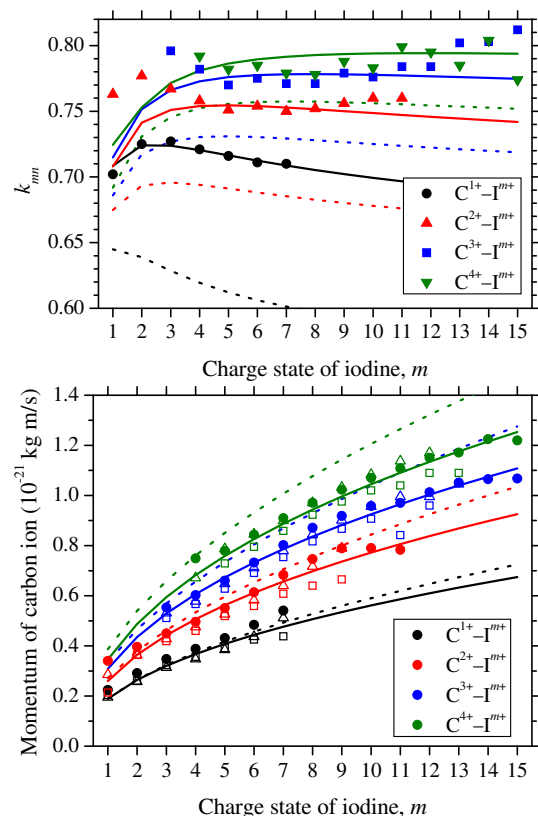
Figure 33. (Top) Momentum correlation coefficient k_{mn} for $I^{m+}-C^{n+}$ coincidences in iodomethane [352]. Closed symbols indicate the coefficients determined from experimental data. Solid lines and dotted lines of the same colour indicate $|p(C^{n+})/p(I^{m+})|$, calculated in the charge build-up and the instant charge creation scenarios, respectively. (Bottom) Momentum of carbon ions in $I^{m+}-C^{n+}$ coincident pairs. Lines: predictions of the models as in (Top). Different symbols indicate the results different methods of analysis for the same experimental data illustrating the accuracy of the analysis. Reproduced with permission from *Journal of Physical Chemistry Letters*, Copyright (2015) American Chemical Society.

and a pulse width of $\sim$10 fs, Motomura *et al.* [352] performed momentum-resolved ion coincidence for iodomethane (CH_3I). They demonstrated that charge states up to $+22$ were produced and that both the C-H and the C-I bonds were broken on sub-10 fs timescales [352]. The authors stressed the importance of the inclusion of realistic charge dynamics when analysing molecular coulomb explosion experiments and when undertaking molecular imaging using FELs.

Here the main interest was the time-scale of charge redistribution and fragmentation. Momentum correlation coefficients $k_{mn} = p(C^{n+})/p(I^{m+})$ (where $p(I^{m+})$ and $p(C^{n+})$ are the momenta of I^{m+} and C^{n+}, respectively) as well as the absolute values of I^{m+} and C^{n+} were extracted and the results are depicted in Figures 33 (a) and (b).

The dotted lines in the figures represent an instantaneous charge-creation scenario in which the final charge is created instantaneously on all atoms at the ground-state equilibrium structure of neutral CH_3I. These simulations clearly show discrepancies when compared with the experimental results. Erk *et al.* [351] noted similar discrepancies for CH_3SeH. The discrepancies indicate the fact that interatomic distances have considerably increased before the atoms reached their final charge states. Therefore, it is essential to include a charge build-up time even when considering very brief X-ray pulses.

In the model simulation of Motomura *et al.*, the exponential function; $Q^{tot} = Q^{max}[1 - \exp(-t/\tau)]$ was assumed for the charge buildup (where Q^{max} is the final charge and τ is the charge build-up time that represents the time scale of the Auger cascades when the X-ray pulse is sufficiently brief).

To reproduce the momentum correlation coefficients $k_{mn} = p(C^{n+})/p(I^{m+})$ in Figure 33 (a), however, it turned out that the charge redistribution rate should also be taken into account. In the model by Motomura *et al.*, the charge redistribution was expressed by the rate equation $dQ^{CH3}(t)/dt = R \times Q^{I}(t)$. The best agreement between the model simulations (solid lines) and the experimental results in the figures was achieved using a charge build-up time $\tau = 9$ fs and a charge redistribution rate $R = 0.37$ fs^{-1}. Although the model by Motomura *et al.* was empirical and did not concentrate on the physical mechanisms behind the charge redistribution, they noted that this typically happens during the later stages of the Auger cascade that involve molecular orbitals not localized on the iodine atom.

Nagaya *et al.* [353, 354] extended momentum-resolved ion coincidence studies at SACLA to 5-iodouracil $C_4H_3IN_2O_2$ (5IU), which is an analogue of uracil, one of the four canonical nucleobases of ribonucleic acid (RNA). They derived kinetic energy distributions and momentum correlations of fragments from the measured momentum vectors of each fragment ion recorded in coincidence. Comparing the simulation results (derived using a model analogous to that of Motomura *et al.*) with the experimental data, they found that the charge build-up takes $\sim$10 fs while the charge redistributes from the I atom to the other atoms in a couple of fs. To gain insights into motions of the individual atoms in real space they employed model simulations validated by comparison with experimental observables. Figure 34 depicts the results of simulations. It is clear that, within the 10 fs XFEL pulse duration, the C-H bonds are significantly elongated (by a factor of two or more) but the other bonds are elongated only by 5 to 10 %. This finding may be very general for similar nucleobase molecules and thus validates that, if the
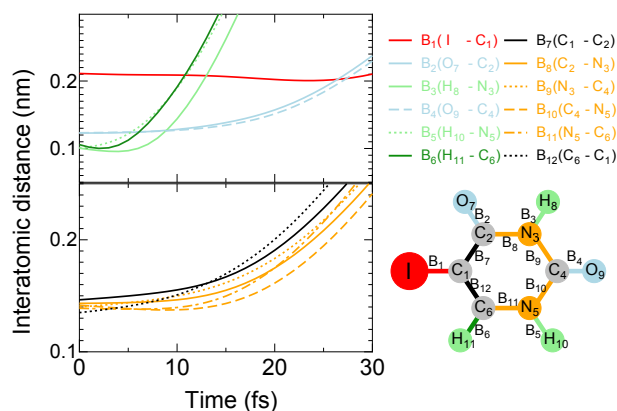
Figure 34. Time evolution of interatomic distances in 5-iodouracil (5IU) obtained by model simulations [353]. Upper panel: Interatomic distance of I–C (red line), O–C (sky-blue lines), H–C (dark-green line), and H–N (light-green lines) pairs. Lower panel: Interatomic distance of C–C (black lines) and C–N (orange lines) pairs. Reproduced from *Physical Review X*. Open Access American Physical Society.

XFEL pulses are sufficiently brief, the single-shot coherent diffraction imaging approach of single bio-macromolecules will interrogate a target sample left practically unperturbed.

Although many gas-phase studies at FELs are performed on randomly oriented molecules there have been a number of experimental studies on fixed-in-space molecules and several groups are actively working on the techniques necessary to generate ensembles of oriented or aligned molecules. Recent work by Kierspel *et al.*, for example, has demonstrated a high degree of molecular alignment ($< \cos^2 \theta_{2D} = 0.85 >$) on interacting few mJ Ti:Sa laser pulses of 94 fs duration with 2,5-diiodothiphene ($C_4H_2I_2S$) [355]. Although this technique was demonstrated at LCLS, where the pulse repetition rate was 120 Hz, its applicability to the future European XFEL where the number of pulses per second will be in the tens of kHz was highlighted.

Another important type of experiment not yet discussed is that of time-resolved measurements of photoexcited molecules. When an optical laser is used to provide pump pulses, however, temporal jitter between these and the FEL probe pulses can be as large as several hundred femtoseconds. Therefore, for pump-probe measurements of this type with fs temporal resolution, simultaneous measurement of relative pulse arrival times are essential [356]. Employing the arrival timing monitor tool available at LCLS, Erk *et al.* [357] successfully imaged charge rearrangement dynamics in gas-phase iodomethane molecules during dissociation induced by a near infrared (NIR) laser. Mapping the electron transfer between the methyl and iodine fragments as a function of their interatomic separation

set by the NIR/X-ray delay, they found that electron transfer can take place for distances up to 20 Å. Nowadays, arrival timing monitor tools are available at other facilities and optical-laser-pump/FEL-probe experiments with femtoscond resolution are becoming mainstream for the investigation of ultrafast molecular and charge dynamics in real time.

6.2.3. Clusters

Understanding the dynamics of matter exposed to intense FEL pulses is not only of fundamental interest but also crucial to the rapidly emerging field of dynamic structure retrieval from X-ray scattering data [358–360]. In the previous Section, we saw how fast a molecule blows up after many electrons are removed by an intense FEL pulse but the size of the molecule considered was still relatively small comparised to macromolecules and nano-structured samples. To investigate FEL-induced dynamics of matter beyond small molecules, atomic clusters are ideal objects because their size can be varied from very few atoms to a bulk-like macroscopic object and still there is no energy dissipation into a surrounding medium. Again only some of the works on rare gas clusters will be very briefly reviewed.

The very first short-wavelength FEL experiments were indeed on xenon atomic clusters. Using the VUVFEL at the TTF at DESY, with ∼13 eV photons and a power density of up to 7×10^{13} W/cm^2, Wabnitz *et al.* observed [308] very energetic (∼ keV) highly charged (up to 8+) atomic ion fragments from Xe clusters of up to 30,000 atoms. Such violent Coulomb explosion of clusters was known for intense IR laser experiments [361, 362]. For example, when an atomic cluster is irradiated by infrared laser at $> 10^{16}$ W/cm^2, electrons are stripped from the individual atoms in the cluster by the strong electric field of the laser but are trapped by the Coulomb potential of the highly charged ionic cluster thus forming a nanoplasma. The trapped quasifree electrons are further heated by the IR laser *via* inverse bremsstrahlung (IVS). The parent ionic cluster is further ionized by electron collisions and eventually leads to violent Coulomb explosion. In spite of this, the observation of violent Coulomb explosion of xenon clusters irradiated by intense VUV pulses [308] was surprising. Though the heating mechanism was unclear, it was evident that a nanoplasma was formed. This surprising result invoked a series of theoretical studies [363–369]. Electron spectra recorded under similar conditions were also reported [370], providing evidence of thermal emission from the nanoplasma. Later, Ziaja *et al.* [371, 372] showed that these VUV results could be fully explained by a unified model that includes heating of quasifree electrons due to enhanced

IVS [363, 368], increased photoionization within the sample (inner ionization) due to a lowering of the interatomic potential barriers [364, 369], and heating due to many-body recombination processes [366].

At SCSS, over the photon energy range 20 and 24 eV, with the FEL power density in the range $10^{11} - 10^{14}$ W/cm^2, Nagaya and coworkers investigated extensively EUVFEL-induced dynamics of various rare gas clusters [373–380]. Under these experimental conditions they found (*via* ion spectrometry) frustration of direct cluster photoionization stemming from the strong Coulomb potential of the highly ionized cluster but no indication for heating mechanisms other than sequential photoionization of the individual atoms in the cluster [373, 374, 377]. They also discussed charge redistribution in both xenon clusters [375] and in argon-core–neon-shell clusters [376]. Applying VMIES to neon clusters and tuning the photon energy to the 2p to 3d excitation at 20.3 eV below the ionization threshold and with a power density $2 \times 10^{13} - 2 \times 10^{14}$ W/cm^2, they found evidence of very efficient nanoplasma formation and by way of explanation proposed an exciton-Mott transition *via* excitation of many atoms in the cluster [379]. Reducing the FEL intensity below 5×10^{11} W/cm^2 they found novel decay pathways of multiply exited neon clusters [380]. In these novel decay pathways, de-excitation of an atomic 3d excited state to a close-lying 3p or 3s state leads to the emission of an electron from a neighboring Rydberg atom. This is a variant of interatomic Coulombic decay (ICD) [381, 382] and may be called intra-Rydberg-ICD. Intra-Rydberg-ICD quenches the direct ICD to the ground state and is followed by ICD cascades yielding more ions.

At FERMI, at a photon energy of 21.4 eV and with FEL power densities up to 10^{13} W/cm^2, applying ion spectrometry and VMIES to helium droplets, LaForge *et al.* [383] and Ovcharenko *et al.* [384] respectively found collective autoionization (another variant of ICD) of multiply excited He clusters in which at least three 2p excited atoms exchange energy.

At FLASH, Bostedt and coworkers observed electron spectra (photon energy of ∼38 eV and power density up to 5×10^{13} W/cm^2) of Ar clusters with an average cluster size of ∼100 atoms and they found that the cluster ionization process is a sequence of direct electron emission events in a developing Coulomb field and that a nanoplasma is formed only at the highest investigated power densities where ionization is frustrated due to the deep cluster potential [385]. They also observed electron spectra at a photon energy of ∼90 eV and an intensity up to 6×10^{16} W/cm^2 for Xe clusters with an average cluster size of ∼2,000 atoms and found emission of very fast thermal electrons whose energy was larger than that of 4d photoelectrons

(20 eV), providing evidence for efficient thermalization of nonequilibrium plasma [386, 387].

However, the most important experimental achievement at FLASH may be that they opened up a new avenue for the study of FEL-induced dynamics of atomic clusters by simultaneous X-ray scattering and ion detection [388]. Figure 35 depicts a schematic layout of this experiment [389]. FEL pulses are focused on the cluster beam. Ions produced at the crossing point are detected by a time-of-flight ion spectrometer. Femtosecond FEL pulses with ∼90 eV photon energy and power densities up to 10^{14} W/cm^2 are scattered by single xenon clusters and detected by an X-ray detector. Such X-ray scattering images allow one to study, for example, cluster morphology. A selection of experimen-
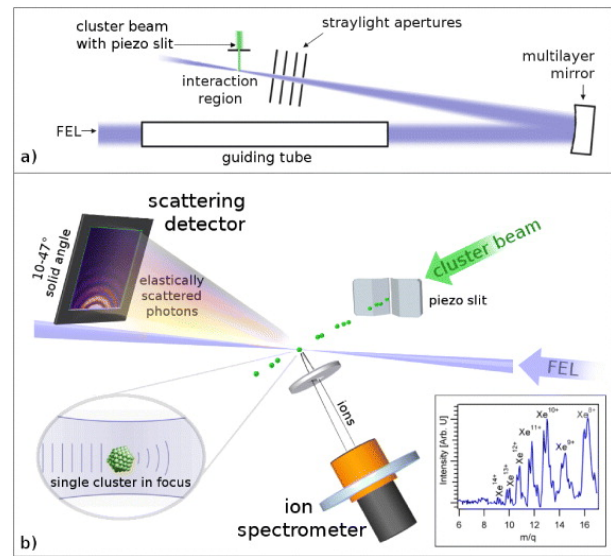

Figure 35. Schematic layout of the experiment [389]. (a), schematic layout of optics. (b) schematic layout of the interaction region. A cluster beam is skimmed down to one cluster in the focal volume by a piezo slit. The micrometer focal spot is optimized using a time-of-flight ion spectrometer. By moving the multilayer mirror along the bisecting line between the incoming and focused FEL beams, one can scan on power density-dependent non-linear processes in xenon ion spectra (displayed for highest power density in the inset). A fast readout X-ray detector detects the elastically scattered photons from single xenon clusters. Reprinted from *New Journal of Physics*, Open Access Institute of Physics Publishing Ltd.

tal patterns that snapshot the cluster morphology are displayed in the first row of Figure 36 [389]. A comparison with the simulated patterns shows that very good agreement can be obtained and that the fine structure is reproduced when the size and degree of fusion are taken into account (middle row). The masks used for the Fourier transformations as well as the yielded parameters are displayed in the third row. The finding of various degrees of fusion of two clusters in direct contact into one slightly non-spherical structure indicates

that inter-stages of the cluster growing process driven by coagulation of particles can be frozen out and be detected milliseconds after the expansion. It should also be noted that the scattering patterns carry not only the structural information of the individual clusters as described above but also the information of transient electronic configurations of highly excited states of the cluster [390], which cannot be accessed by other spectroscopic methods.
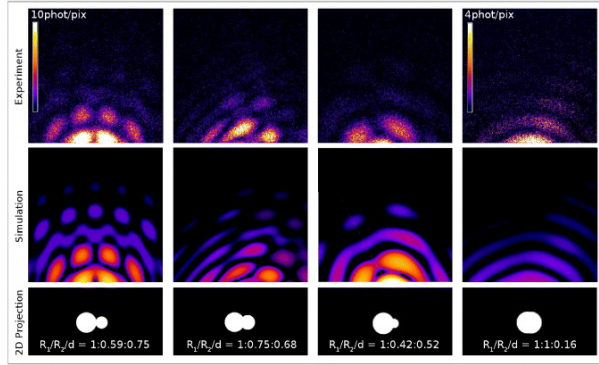

Figure 36. Snapshots of cluster morphology: a selection of typical experimental patterns (first row). Simulated patterns considering different sizes and degree of fusion are in good agreement (second row). Corresponding 2D projections with ratios of bigger radius to smaller radius to the distance between the centers (third row). Reprinted from *New Journal of Physics*, Open Access Institute of Physics Publishing Ltd.

At LCLS, Thomas *et al.* [391] investigated explosions of Xe clusters of ∼11,000 atoms using a photon energy of 850 eV and power density of up to 10^{17} W/cm^2, and employing ion spectrometry and electron spectroscopy. They found evidence for the formation of a nanoplasma whose plasma temperature (∼125 eV) was determined by photoionization heating. The dominance of the Xe$^+$ ions in the charge-state distribution was attributed to efficient three-body recombination. Gorkhover *et al.* [392] investigated the nanoplasma dynamics of single mesoscopic Xe clusters irradiated with XFEL pulses exceeding 10^{16} W/cm^2 at ∼800 eV, recording simultaneously X-ray scattering patterns and ion spectra with a setup similar to that in Figure 35. This approach allowed them to eliminate the influence of the laser focal volume intensity and particle size distribution. The ion yield spectra from single clusters recorded in coincidence with the scattering patterns are depicted in the top panel of Figure 37. In addition, in the bottom panel of Figure 37, focal-volume integrated ion spectra are presented for two different power densities. It can clearly be seen that highly charged ions are created for clusters illuminated with the intense XFEL pulses. This finding illustrates that nanoplasma recombination is efficiently suppressed with the intense XFEL pulses
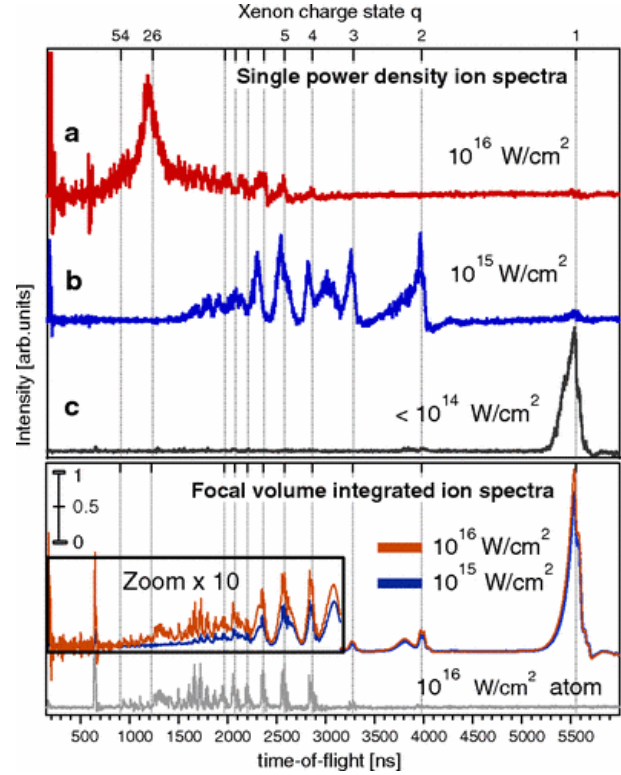

Figure 37. Top panel: Single shot ion spectra recorded in coincidence with the scattering images that include the information of the FEL power density [392]. Bottom panel: Focal volume integrated ion yield spectra for the cluster and atomic targets. The single-shot spectra strongly correlate with the position of the cluster in the FEL focus and are strikingly different from the integrated spectra. Reprinted with permission from *Physical Review Letters*, Copyright (2016) the American Physical Society.

and contrasts to the observation by Thomas *et al.* where all signals were accumulated without eliminating low-fluence events that dominate the accumulated signals.

At SACLA, at photon energy of ∼5 keV and power density of ∼10^{17} W/cm^2, Tachibana *et al.* [393] investigated nanoplasma formation of Ar clusters in the range of 100 - 1000 atoms using VMIES and found evidence of nanoplasma formation. Dedicated theoretical simulations utilising molecular dynamics well reproduced the observed electron spectra. They found – in contrast to nanoplasma formation by FEL pulses in the VUV to soft X-ray ranges (described above) that nanoplasma formation by *hard* X-ray pulses is a highly-indirect processes. Here, secondary electrons are generated either by inelastic scattering, of the electrons ejected in the cascade of relaxation steps of the deep core-holes initially created on individual atoms, or in the later stages of the cascade itself. These low-energy electrons are trapped by the highly charged cluster forming the nanoplasma. This plasma

formation mechanism is specific to the hard X-ray regime and may, thus, also be important for XFEL-based molecular imaging studies.

6.3. Photochemistry

The field of femtochemistry [394] has also been explore... ...ng and spe... techniq... ...03]. In ma... these e... ...ary to time... optical... ...ditional inf... of stru... ...first time... XFEL... ...upon deve... establis... ...e rings ove... decade...

6.3.1. Molecular Photochemistry

Figure 3... ...ed at SACLA for RuCo [41... ...*unications*, Open Access Na...

Ma... ...rmed on molecular spec... ...and soft X-ray regimes, ...and scattering tools. O... ...aches has been the use ... ...imultaneously. This ha... ...e rings where both X-... ...o called wide-angle so... ...esonant X-ray emission (XES) have been combined to probe simultaneous... ...electronic changes in the s... ...[414, 415]. The layout of su... ...show in Figure 38. Recentl... ...t SACLA to investigate el... ...llic RuCo system, which is... ...stem [413]. This molecul... ...center attached to a Co^{3+}(... (where bpy is the bipyrid...

Up... ...ue light the Ru moiety ... ...gh the bridging ligand t... ...electronic changes in the metal centers. $Ru... \to Ru...$ and $Co^{3+} \to Co^{2+}$. In addition there is an expected structural change in
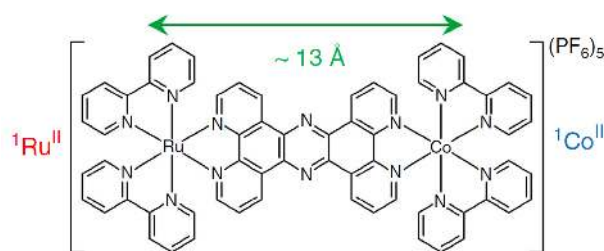
...as the bp... ...n the ...By combining XDS, which provides a pair-distribution function of all atoms in the sample, and XES, which is sensitive to the oxidation state of the metals, the experiment resolved the electron arrival on the Co moiety. In addition the XDS signal also clearly showed the slower evolution of energy into the surrounding solvent molecules. The time evolution of the various signals are shown in Figure 40.

...matic of th... ...duced ...*municatio*... ...lishing

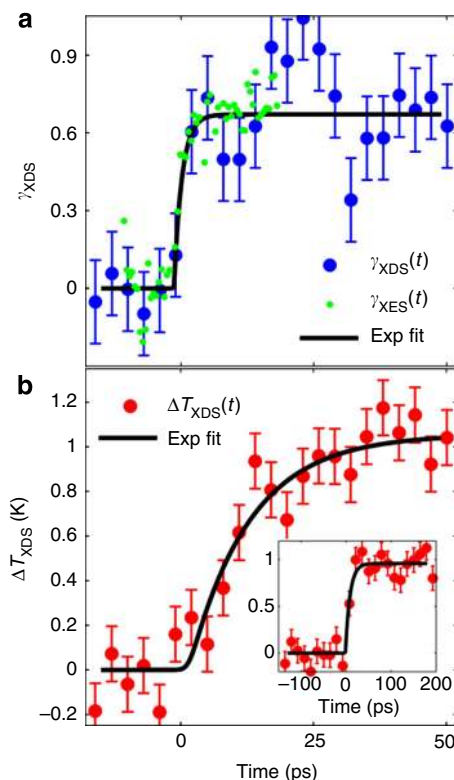**Figure 40.** XDS and XES time scans for the RuCo experiment [413]. Reproduced from *Nature Communications*, Open Access Nature Publishing Group.

In addition to molecular species in solution, gas-phase molecular dynamics have also been investigated.

An example of this was an investigation of the dissociation of gas-phase 1,3-cyclohexadiene upon excitation with UV light (see Figure 41 for the experimental setup used) [416, 417]. This photoreaction can lead to several excited state species, with a final product of 1,3,5-hexatriene and the principal goal was to resolve the bond-breaking event and subsequent structural rearrangement into the dissociated species. To probe this femtosecond X-ray scattering at 8.3 keV, measured with a 2D CSPAD detector was used [418]. A molecular-dynamics simulation with 100 trajectories was required to simulate all the various reaction pathways the molecule can undergo during the ring-opening reaction. The experimental results showed the transformation occurs on an 80 fs timescale and 8 trajectories were required to fit the data accurately. From these trajectories the following physical pictures emerged: upon absorption of the UV photon the carbon-carbon bonds of the cyclohexatriene expand rapidly, after 1-2 vibrational periods the C1-C6 bonds break, all of which occurs within 30 fs.
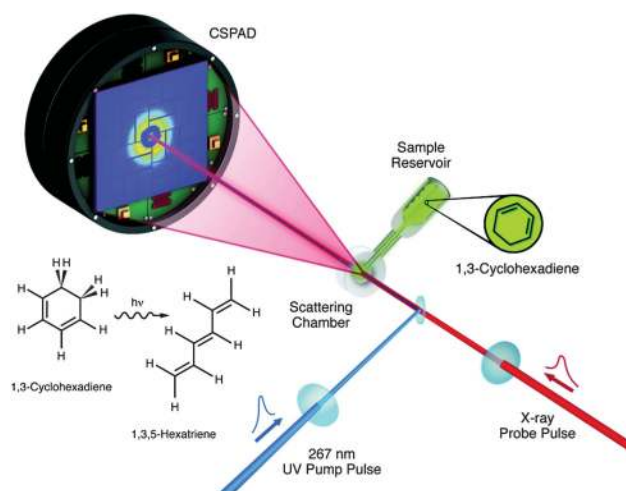

Figure 41. Using X-ray scattering to image the ring-opening photoreaction of 1,3-cyclohexatriene [416]. Reproduced with permission from *Physical Review Letters*, Copyright (2015) Americal Physical Society.

6.3.2. Surface Photochemistry

An area of research that has received significant attention at XFELs has been surface photochemistry [419–424]. Many chemical reactions take place on surfaces or interfaces, including many important catalytic reactions, but the ability to trigger these reactions for ultrafast experiments has not been straightforward. One approach has been to adsorb the molecules onto a metal surface and then to photoexcite the metal, the expectation being that the metal will transfer energy to the adsorbed species thus triggering a reaction [423]. By using X-ray absorption spectroscopy at the oxygen K-edge (530 eV), Östrom and co-workers were able to probe the transition state of CO oxidation (CO + O) on a Ru metal surface after photo-excitation of the Ru metal with a 400 nm laser pulse. The results indicate that after electronic excitation of the substrate there is a rapid increase in adsorbate-substrate vibrational excitations, which drive the CO oxidation reaction. The reaction sequence extracted from the XAS measurements and predictions from a quantum oscillator model are shown in Figure 42.
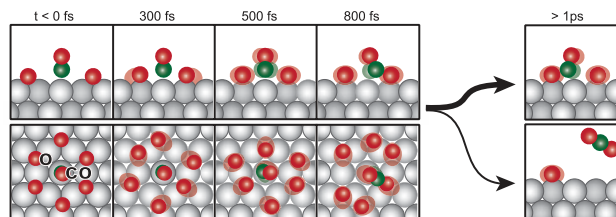

Figure 42. Pictorial representation of the CO + O oxidation reaction triggered by photo-excitation of the metal substrate [421]. Reproduced with permission from *Science*, Copyright (2015) American Association for the Advancement of Science

6.4. Surfaces and Materials

Though reactions to the suggested use of X-ray FELs for dynamical studies of materials were initially often negative, avoiding sample damage by fine-tuning the X-ray flux at the sample has led to considerable progress over recent years.

In particular, it is now possible to extend the well-established X-ray spectroscopy and scattering techniques for the investigation of the static electronic structure of matter like for example photoelectron spectroscopy, X-ray emission spectroscopy or resonant X-ray scattering to probe the evolution of electronic structure after controlled excitation in the time domain.

6.4.1. Time-Resolved Photoemission

In principle, FELs are well suited for the study of non-equilibrium processes at solid surfaces and although this topic can be extended to many potential spectroscopies here the focus is on time-resolved photoelectron spectroscopy (tr-PES). This is an important but challenging spectroscopy as was realized during the first experiments with soft X-ray FELs.

Until the advent of the first X-ray FELs, tr-PES was limited by the use of table-top laser sources and the generation of high harmonics starting from ultrafast lasers. Most of the experiments were performed on gas phase systems and only recently has FEL-based tr-PES been performed on solid surfaces and interfaces with sub-ps time resolution [425]. At the same time

the theory and modelling of ultrafast phenomena at solid surfaces probed by ultrafast X-ray time resolved spectroscopies has made important progress; an interesting update can be found in reference [426]. However, only after the introduction of the X-ray free-electron lasers FLASH and LCLS was it possible to perform experiments at the resonant energies of the core levels of elements such as carbon, nitrogen and oxygen. Though with these it became abundantly clear that the most important technical questions to be addressed were control of the photon density in the FEL pulse, the jitter in energy and bandwidth of the FEL pulses and the pointing stability of the FEL light spot on the sample. After the very first experiments, the complex and challenging aspects of tr-PES on solid surfaces became very clear, as shown for example by the measurement of the W-4f shallow core-levels in a W(110) single crystal [427]. This experiment clearly revealed the dramatic effects induced by space charge as the FEL fluence was increased, see Figure 43.

Later it was clear that the space charge problem was also affecting the results of spin-resolved PES experiments. In particular, by performing a spin resolved PES experiment at different fluences it

Figure 43. W 4f photoemission as a function of incident X-ray intensity, focal size $395 \pm 23 \times 274 \pm 14 \mu m^2$ [427]. Reproduced from *New Journal of Physics*, Open Access Institute of Physics Publishing Ltd.

was observed that at higher photon intensities the measured spin polarisation was reduced [428]. The question of space charge, along with appropriate statistics is, even now, the principal challenge for meaningful and unique tr-PES experiments with FELs. In other terms the electron spectroscopy of deep core levels in the time domain is still problematic.

In the literature several models concerning space charge effects in PES have been reported and in Figure 44 a cartoon taken from [429] indicates the essentials of the problem. The most important parameter is the integrated photon flux on the solid surface. The numerical simulation shown here provides some information about the electron cloud (grey circles) and about the primary electrons electrons (black circles). The calculations clearly suggest that the space charge effects depend on the source parameters and the sample properties [429]. In summary, for effective tr-PES on solids the photon density of the FEL pulse must be controlled and space charge effects minimized, without this the measured overall energy and momentum resolution will be degraded. Although momentum resolution is above-all important for angle resolved PES measurements involving the band dispersions, angle-resolved PES of core levels may prove to be important for time-resolved photoelectron diffraction experiments. Nevertheless, the primary aim is to achieve the possibility of performing tr-PES of deep core levels with the statistics and energy resolution typical of conventional PES. Overall, controlling the photon density in the FEL pulse while performing tr-PES and achieving suitable signal statistics remain mandatory for the cases where time and frequency spectroscopic information are critical for an understanding of the ultrafast processes at a surface. This issue can be addressed only by controlling the repetition rate and the photon pulse energy and bandwidth. Now, it is clear that to limit space charge effects while keeping good signal statistics, FEL sources at repetition rates of the order of several kHz are required. This is particularly challenging if the pulse duration, and hence the time resolution, required is of the order of 100 fs or less.

Consequently to-date tr-PES experiments at FELs have been mostly performed at FLASH where the superconducting technology used for the linear accelerator enables operation with up to 8000 pulses/s. In one of the first experiments core level photoemission was used to monitor the ultrafast melting of local charge-order in TaS_2, while the material was optically driven through an insulator-to-metal transition which is accompanied by a change in charge-order [430]. Later it was demonstrated that even spin- and tr-PES studies are possible with high repetition rate
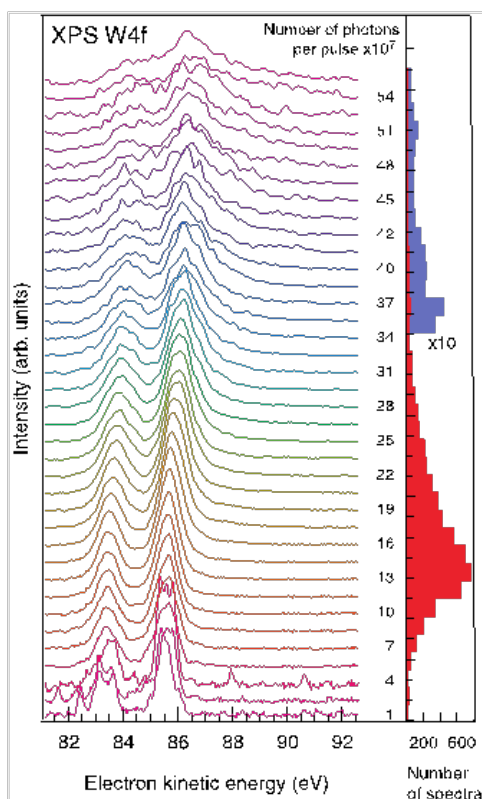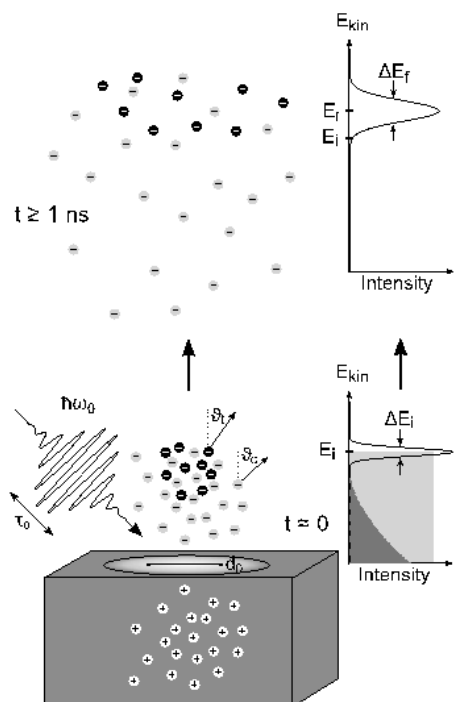
Figure 44. Cartoon of a solid-state photoemission experiment employing a pulsed photon source with photon energy $h\omega_0$ and pulse duration τ_0 [429]. Reproduced with permission from *Physical Review B*, Copyright (2009) American Physical Society.

FELs [431]. Charge transfer processes at the interface between dye molecules and semiconductor substrates have been studied at LCLS with tr-core-level PES [425]. Recently the first tr-HAXPES (Hard X-ray PES) results have been reported from SACLA [432]. In an attempt to study ultrafast electron dynamics at a surface it was demonstrated at FLASH that tr-PES experiments on core levels – in this case Ir 4f – can be performed under conditions where it is possible to follow the temporal changes of surface and bulk states separately by making use of surface core level shifts [433].

Clearly, tr-PES is of importance for studying ultrafast electronic structure changes and local charge rearrangement in processes, and ultra-fast dynamics at surfaces, interfaces and solids. Of importance for both fundamental studies and for applied problems such as catalysis, energy conversion storage and distribution [434], and also magnetism and ultra-fast switching processes in correlated electron systems. It should be emphasized that for tr-PES high repetition rate FELs are complementary to HHG laser sources and are, despite the limitations imposed by space charge considerations, the sources of choice when photon energies above *ca.* 100 eV are considered.

6.4.2. Ultra-Fast Magnetization Dynamics

An area of very intense research with FELs is ultra-fast magnetization dynamics using coherent imaging and scattering techniques in an attempt to combine fs-temporal and nm-spatial resolution. The fundamental physics behind ultra-fast optical switching of magnetic domains is an open question ever since the pioneering work by Beaurepaire *et al.* which showed that ultra-fast demagnetization induced by an ultra-short optical laser pulse occurs on femtosecond timescales [435]. More recent studies demonstrating that with circular polarised femtosecond laser pulses reversible all-optical switching of the magnetization can be realized in certain materials have led to increased interest in ultra-fast magnetization dynamics due to its application in magnetic data storage [436].

First experiments at FLASH demonstrated the possibility of recording single-shot resonant magnetic scattering images with FELs. These experiments were performed on a CoPt multilayer sample with the images taken with linearly polarised XUV pulses at the Co $M_{2,3}$-edges [437]. Soon after the soft X-ray beamline [438] became operational at LCLS magnetic X-ray holography experiments were performed on similar samples at the Co $L_{2,3}$-edges [439] using circular polarised light produced with a Co polariser (see Figure 45).

These experiments showed that for a certain range of X-ray fluences it was possible to accumulate spectroholograms with the short pulses from an FEL and to reconstruct the magnetic domain pattern afterwards.

The first time-resolved demagnetization study using a pump-probe approach, with an IR-pump pulse and an XUV probe pulse to record a resonant magnetic scattering pattern as a function of pump-probe delay, was performed at FLASH (see Figure 46) [440]. In this experiment production of the magnetic scattering signal in less than 300 fs was observed to be accompanied by an apparent increase in magnetic correlation length. This increase in correlation length has been attributed to softening of the domain walls due to super-diffusive spin currents across them. This study represents the first experiment were correlations between fs-demagnetization and nm-scale structural changes have been recorded.

At LCLS the element specificity of resonant magnetic scattering has been used to investigate the all-optical magnetization switching process induced by a circularly polarised, femtosecond laser pulse on a ferrimagnetic GdFeCo sample [441]. Recording the tr-magnetic scattering signal at the Gd-M_5-edge and the Fe-$L_{2,3}$-edge, respectively, the authors were able to disentangle the magnetization dynamics in Gd-rich and Fe-rich regions of the sample. They showed that
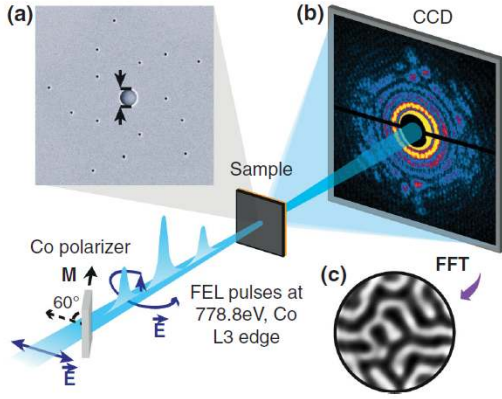
Figure 45. (a) Scanning electron microscopy image of a 15-reference gold holography mask, showing the aperture for the sample and the reference holes. (b) A CCD camera located downstream records the spectrohologram in the far field. (c) Reconstruction of the initial magnetic domain state from a low-fluence-accumulated spectrohologram with 58% circularly polarised X-ray pulses (<2mJ/cm^2). The dark and light regions are 100–150 nm wide domains with opposite out-of-plane magnetization directions [439]. Reproduced with permission from Physical Review Letters, Copyright (2012) American Physical Society.

the magnetization reversal is influenced by non-local transfer of angular momentum from Fe-rich to Gd-rich regions.

A very interesting observation in the single-shot imaging experiments on magnetic samples was the disappearance of the magnetic scattering signal even without a pump pulse before any changes in the charge scattering signal or even any sample damage was observed. So far this effect is not fully understood and two explanations based on transient X-ray induced changes of the electronic structure through the creation of multiply ionized atoms [442] and the influence of stimulated X-ray emission [443], respectively, have been invoked to explain the observations. With the increasing availability of circular polarised XUV [444] and soft X-ray [445] pulses from FELs, studies of the fs-temporal and nm-spatial magnetization dynamics will get an additional boost in the future.

6.4.3. Non-Equilibrium Dynamics in Strongly Correlated Electron Systems

Condensed matter systems where electronic correlations play an important role show extremely rich and interesting macroscopic physical properties like high temperature superconductivity and colossal magnetoresistance as well as a variety of phase transitions such as, for example, metal-insulator transitions and/or different magnetic phases. These fascinating emergent phenomena are caused by a subtle interplay between electronic (charge, orbital and spin) and lattice degrees of freedom. This interplay leads to various
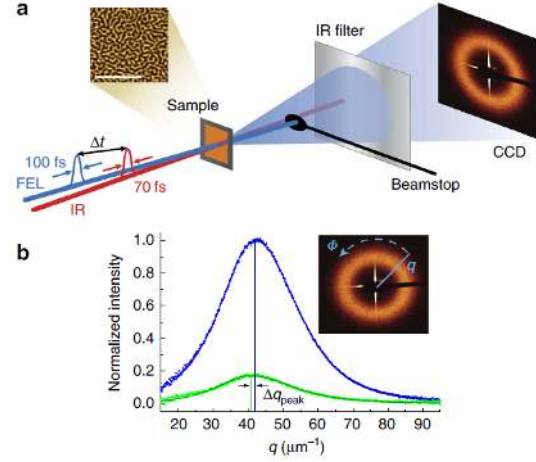

Figure 46. Figure 2 (a) The magnetic multilayer sample is pumped by an optical laser pulse and probed by a delayed X-ray pulse produced by the FEL. The magnetic SAXS pattern is recorded on an IR-protected (CCD) camera while the intense directly transmitted radiation is blocked by a beamstop. The inset shows a typical magnetic force micrograph of the sample in the probed labyrinth-domain state. The scale bar in the micrograph corresponds to μm distance. (b) By fitting the azimuthally integrated (see inset) SAXS intensity, the intensity maximum is determined. A decrease in the intensity and a shift of the peak position Δq_{peak}, when comparing unpumped (blue) and pumped (green) spectra (pump fluence: 14.2 mJ cm^{-2}, time delay: 1.3 ps) is observed [440]. Reproduced with permission from Nature Communications, Open Access Springer Nature.

nearly degenerate competing states and hence complex phase diagrams as a function of temperature, doping and external fields.

Driving strongly correlated systems out of equilibrium and studying their time-dependent relaxation will help the research community both understand and steer transitions between the different stable phases of these complex materials. It may also lead to the discovery of novel transient, metastable phases.

Tr-spectroscopy and scattering experiments have recently shown the great potential of X-ray FELs for such studies. In particular, the combination of element specific resonant excitation and elastic scattering has the unique potential to enable study of the coupled dynamics of charge, spin and lattice order in these complicated systems.

The first tr-resonant soft X-ray scattering experiments at the O-K-edge performed at FLASH on magnetite were aiming at investigating the driving force behind a photoinduced insulator-to-metal transition [446]. A detailed study at LCLS [447] on the same material using a combination of tr-resonant soft X-ray diffraction at the Fe-L$_3$-edge with tr-optical spectroscopy later revealed a fast quench of the trimeron charge order followed by a picosecond structural transition involving phase segregation of an insulating island embedded in a conducting network.

Tr-resonant X-ray diffraction at the Ni-L_3 edge was used to probe the coupled dynamics of charge- and spin-order in a stripe-ordered state of $La_{1.75}Sr_{0.25}NiO_4$ nickelate induced by photodoping [448]. In another experiment at LCLS photoinduced melting of charge- and orbital-order in a perovskite manganite – $Pr_{0.5}Ca_{0.5}MnO_3$ – was studied with tr-X-ray diffraction [449]. Even so the change in crystal symmetry associated with this transition occurred over different timescales for the electronic and vibrational degrees of freedom of the system, the authors were able to describe the dynamics of the phase transformation using a single time-dependent order parameter that depends only on the electronic excitation [449].

A very interesting approach in the context of these non-equilibrium dynamics studies is the use of THz pump pulses to drive the systems out of equilibrium *via* the excitation of specific phonon modes leaving the electronic system unchanged by the pump pulse. This has been used to drive the spin dynamics in a multiferroic material – $TbMnO_3$ – *via* resonant excitation of an electromagnon with an intense few-cycle THz pulse [450]. The resulting spin motion in the Mn 3d-shell was observed using time-resolved resonant soft X-ray diffraction at the Mn-L_2-edge. The results showed that atomic-scale magnetic structures can be manipulated with an electric field pulse on a sub-picosecond time scale [450].

An even more intriguing effect was observed in cuprates upon non-linear excitation of phonon modes with intense THz pulses. Upon excitation [451], these materials show transient features of superconductivity far above the equilibrium transition temperature. In a time-resolved X-ray diffraction study on $YBa_2Cu_3O_{6.5}$ performed at LCLS [452] it was demonstrated that this behaviour is induced by a lattice distortion (see Figure 47) where the inter-bilayer distance is decreased while the intra-bilayer distance is increased at the same time. Calculations show that this leads to an effective increased hole doping in the CuO_2 planes *via* charge transfer to the Cu-O chains as indicated in the Figure [452].

Making use of the ultra-short and very intense X-ray pulses from LCLS it was recently demonstrated that it is even possible to perform tr-resonant inelastic X-ray spectroscopy (tr-RIXS) with momentum resolution to probe the dynamics of elementary excitations in highly correlated materials [453]. In the specific experiment the dynamics of the magnetic correlations were probed after photo-doping the Mott insulator Sr_2IrO_4 [453].

A completely new approach to studing the dynamics of elementary excitations such as phonons by Fourier-transformation of the time-dependent diffuse scattering signal after photoexcitation has also been
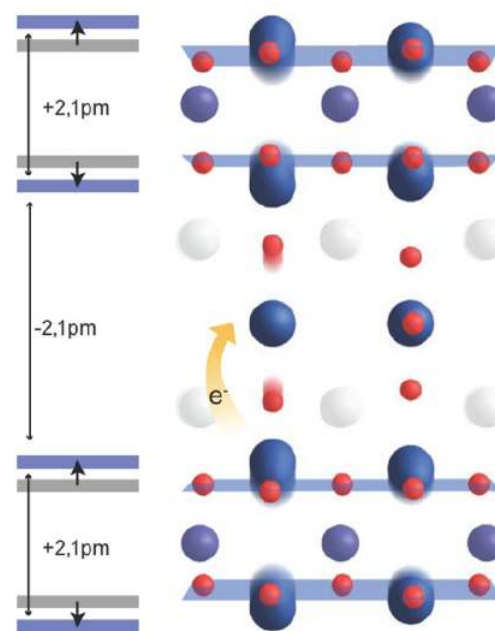

Figure 47. Sketch of the reconstructed transient crystal structure of $YBa_2Cu_3O_{6.5}$. The atomic displacements from the equilibrium structure involve a decrease in interbilayer distance, accompanied by an increase in intrabilayer distance. Adapted from [452]. Copyright (2014) with permission from Nature Publishing Group.

successfully demonstrated at LCLS [454].

Finally it should be mentioned that the very intense X-ray pulses from LCLS have recently been used to study the charge-density-wave order in $YBa_2Cu_3O_{6.67}$ in the presence of a very high magnetic field [455]. Here the intense X-ray pulses were synchronised with a pulsed high-field magnet enabling X-ray diffraction studies in magnetic fields up to 28 Tesla [455].

To conclude, the possibility of performing tr-resonant- and non-resonant X-ray diffraction studies with ultra-short X-ray pulses from an FEL provides many exciting opportunities for the study of the non-equilibrium dynamics of the coupled degrees of freedom in strongly correlated materials.

6.4.4. Non-Linear X-ray Spectroscopy

With the development of FEL radiation sources a new area of X-ray spectroscopy commenced that will, without doubt, have a comparable impact to that of lasers in the areas of non-linear optics and spectroscopy [456].

For non-linear, ultrafast, time-resolved techniques, state specific information is often provided through multi-photon resonances with various combinations of sequential photons [457]. Theoretically, combinations of multiple X-ray photons resonant with
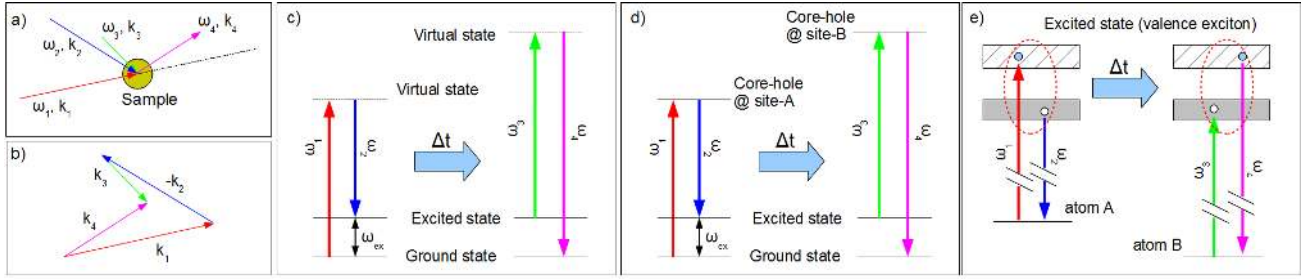
Figure 48. (a) Sketch of a FWM experiment. (b) Phase matching conditions. (c) CRS in the optical regime. (d) and (e) are the excitation processes and level scheme for an EUV/X-ray CRS experiment involving core transitions in both the excitation and probing process.

core transitions characterize different excitation processes due to specific sequences of light-matter interactions [458]. Thus, particular sub-processes can be enhanced by matching the pulse frequencies to transitions between molecular eigenstates. This provides both a high selectivity and flexibility due to momentum and energy conservation of the photons interacting with the material. The various possible non-linear processes are typically categorized according to the number of photons involved; for example, sum-frequency generation (SFG), and two-photon absorption and stimulated emission with two photons. Other non-linear X-ray phenomena include time-resolved transient gratings (TG) and four wave mixing (FWM) spectroscopy [456].

One of the first demonstrations of non-linear optics in the X-ray regime has been two-photon absorption [459], where an atom absorbs two incident photons either sequentially or simultaneously. This process is well know for short-pulse visible lasers, but has only recently been demonstrated for core-electron excitations [460–463], which has required the high peak powers available at XFELs.

Fluorescent decays in the soft X-ray region allow unique access to the structure of occupied valence states whilst keeping both the element selectivity and the chemical state specificity of soft X-ray spectroscopies [464]. Unfortunately, the probability of fluorescent decay, in the soft X-ray range, is below 1% and with a typical spectrometer acceptance of less than 10^{-5} of the full solid angle into which the fluorescence is emitted, soft X-ray emission spectroscopy (XES) or resonant inelastic X-ray scattering (RIXS) experiments require single photon counting for hours in order to obtain useful information.

Using stimulated emission spectroscopy with high intensity, small bandwidth, tunable soft X-ray beams of different color, a stimulated beam containing the same information as a fluorescence spectrum can be formed. In addition to mitigating the low acceptance angle of spectrometers, stimulated emission also suppresses the dominating Auger decays that create electronic damage to the sample. Quantitatively, with

such techniques, two to three orders of magnitude in signal levels can be gained through the suppression of Auger processes, and the quality of the beam directed into the spectrometer can potentially result in increases of around five orders of magnitude in signal levels. That is, the gains resulting from the use of stimulated emission techniques clearly have the potential to revolutionize how we study matter with XES or RIXS based spectroscopies [465].

An objective of more complex FEL-driven ultrafast X-TG experiments is to access wave-vectors at the nm scale [466]. Resonant time-resolved TG-spectroscopy is expected to provide information about ultrafast charge-carrier dynamics after excitation and about the subsequent energy dissipation into lattice vibrations and heating [467]. Due to the spatial and temporal dependence of the energy- and q- dependent TG signals, TG experiments, at XUV and X-ray wavelengths, reveal more information than standard pump-probe experiments. Moreover, exploring the role of resonances in non-linear-X-ray spectroscopy is an essential step towards the realization of more general X-ray FWM schemes such as degenerate four-wave-mixing and coherent anti-Stokes Raman spectroscopy [466].

The spatial resolution of the X-TG method is determined by the fringe spacing and the size of the interaction volume of the excitation and the probe beams, and thus reveals nanoscale dynamics [468]. A goal of FEL driven X-TG experiments is to access wavevectors that cover the full Brillouin zone. At grating periods shorter than the characteristic diffusion lengths, new ballistic transport phenomena are expected to be observed. Transient grating fringe spacings of $\Lambda = $ 1-100 nm, corresponding to coherent scattering wavevectors of $q = 2\pi/\Lambda$, extend to nearly the edge of the Brillouin zone and can be used to examine acoustic modes, non-oscillatory density dynamics, polarisation, and other order-parameter responses on the same length scales. Uniquely, the timescales possible in this kind of experiment map onto appropriate length-scales. Transport phenomena that may be investigated at the nanoscale are [469]: acoustic

phonons, optical phonons, resonant effects, charge carrier drift velocities and electron-phonon coupling.

FWM techniques are currently exploited to study different kinds of dynamics and fundamental processes ranging from, for example, chemical reaction dynamics [470] to light harvesting [471]. FWM is a 3rd-order non-linear process in which three coherent electromagnetic fields ($E_{1,2,3}$) of frequency/wavevector $\omega_{1,2,3}/k_{1,2,3}$ interact in a sample resulting in a fourth field $\{E_4(\omega_4, k_4)\}$, coherently coupled with the input fields; see Figure 48 (a). A large number of different FWM processes may occur depending on the input field parameters (ω_i, k_i, polarisation, time duration and delays, etc.), resulting in a wealth of interactions that can be exploited to study selectively a host of different dynamics.

In coherent Raman scattering (CRS; Figure 48 (c)) two time-coincident fields are used to excite, for example, vibrational modes of frequency $\omega_{\text{ex}} = \omega_1 - \omega_2$ and wavevector $k_{\text{ex}} = k_1 - k_2$. The time evolution of the excited modes is followed by a third time-delayed pulse (ω_3, k_3) that drives the emission of the fourth (signal) field with $\omega_4 = \omega_3 + \omega_{\text{ex}}$ and $k_4 = k_1 + k_{\text{ex}}$. The coherent nature of the CRS process leads to the in-phase addition of the non-linear fields radiated at different sample locations, which may result in a non-linear signal along the so-called phase-matched direction (*i.e.* k_4 in Figure 48).

In soft X-ray CRS one of the input photon frequencies is typically tuned to match the energy of a core-hole resonance ($\omega_{\text{res,A}}$) of a given atom A, while a second pulse ($\omega_2 = \omega_1 - \omega_{\text{ex}}$) generates a coherent population of, for example, valence band excitations with a selected frequency (ω_{ex} in the 1-10 eV range) and wavevector ($k_{\text{ex}} = k_1 - k_2$), see Figures 48 (d) and 48 (e) [458]. The excited electronic wave packet can be then detected after a given time-delay (Δt) by a third pulse, tuned to a core resonance of atom B ($\omega_3 \approx \omega_{\text{res,B}}$), which gives rise to the FWM beam ($\omega_4 = \omega_3 + \omega_x$ and $k_4 = k_1 + k_{\text{ex}}$). Due to the localization of core shells, the selected excitation is initially centered on atom A while the probe mainly interacts with the unoccupied states close to the core shell resonance at atom B. By tuning $\omega_{1,2,3}$ and Δt it is then possible to choose where a given excitation is created, as well as where and when it is probed, opening up the possibility of studying, for instance, the delocalization of electronic excitations and charge/energy transfer processes between different atomic sites.

In order to go beyond the theoretical framework presented in [458] (and references therein) a first demonstration of the real feasibility of FWM techniques involving sub-optical wavelengths has recently been made using FEL radiation at the FERMI facility [472]. In this experiment two ultrafast FEL pulses,

produced by splitting a single pulse using the edge of a flat mirror, were sent to a vitreous S_iO_2 sample. An incidence angle of about 6.2° produced a TG, whose time evolution was monitored using an optical pulse impinging under phase-matching conditions.

The detected signal allowed estimation of the efficiency of the process (namely the ratio of the intensity of the scattered signal (I_{FWM}) over that of the probing optical beam (I_{opt})) to be about 10^{-7}, *i.e.* of the same order as a typical efficiency in the optical range. Moreover, an appreciable soft X-ray TG signal (of $> 10^4$ photons/pulse) was observed throughout the entire probed time delay range. This shows modulations compatible with impulsively stimulated vibrational modes *i.e.* longitudinal acoustic phonons at $\omega_{\text{LA}} \sim 0.15$ THz, hyper Raman modes at $\omega_1 \sim 7.2$ THz (due to correlated rotations of S_iO_4 tetrahedra) and Raman modes at $\omega_1 \sim 25.5$ THz (due to tetrahedral bendings).

These results establish that soft X-ray pulses may be used to generate dynamic gratings using coherent FEL pulses and that the time evolution of resulting FWM response stimulated by sub-optical wavelength radiation can be monitored. Moreover, this experiment demonstrates that soft X-ray TGs can be used to drive selected excitations (molecular vibrations) that are coherently stimulated by non-linear processes in the sample. The resulting signal modulations have the form of a beam propagating downstream of the sample along the expected 'phase-matched' direction.

This was the first step towards the use of soft X-ray FWM for experiments with unprecedented chemical selectivity. Indeed, linear X-ray methods light-matter interactions necessarily occur on a single atomic site, preventing the possibility of detecting real-time coherent dynamics involving distinct atoms, while optical CRS cannot probe spatial coherence between different atomic sites, since only spatially homogeneous distributions of excitons (largely exceeding the exciton coherence length) can be detected. Furthermore, the ($\omega_{\text{ex}}, k_{\text{ex}}$)-range accessible by optical CRS is limited to the sub-eV and sub-10 μm^{-1} range, while X-ray CRS will allow to extension over a range to 100s eV or so and to the nm^{-1} range. In addition, transitions originating from core levels of well-defined symmetry also provide sensitivity (via linear/circular dichroism effects) to spin and orbital momenta together with spin wave creation and propagation. Finally, the possibility of applying an additional time delay between the ω_1 and ω_2 pulses will be a relevant step towards soft X-ray multi-dimensional spectroscopy. This approach will enable time-dependent correlations between electronic excitations to be probed, the analogue of optical multi-dimensional spectroscopy vibrational excitations [473].

6.5. Shock Physics

6.5.1. Background

An understanding of the mechanisms involved at the lattice level that mediate the response of solid-state matter when subjected to a high pressure shock wave has been sought for many decades. Particular goals include gaining insight into the timescales and paths of atomic rearrangement that allow a solid to rapidly flow – as it is observed that above a certain stress (the so-called Hugoniot elastic limit) the pressure-volume response is close to the hydrostat. Understanding is also sought to glean information about the mechanisms that allow polymorphic phase transitions on timescales short compared with the duration of the compression pulse. Dynamic compression on nanosecond or sub-nanosecond time-scales is also a burgeoning field in its own right, as the pressures that can be obtained greatly exceed those that can be produced statically in diamond anvil cells (these ultimately being limited by the strength of diamonds). An experimental capability to extend high pressure solid-state physics research into regimes well in excess of a TPa is also motivated by the torrent of new exoplanets being discovered, and the realisation that solid matter may exist under a wide range of previously unexplored conditions. In certain cases it may even be that such novel forms of matter would be metastable upon release to ambient conditions [474, 475]. Given the role of strength, enthalpy barriers and the associated kinetics, it is yet far from clear how observations from individual experiments on ultrafast timescales relate to long time-scale conditions, and despite its long history, from the perspective of being a routine method to produce high pressure states, in many ways the field is very much still in its infancy.

The first successful attempts to record lattice response under shock conditions used diodes as the source of X-rays, giving a temporal resolution of many nanoseconds [476, 477]. Since that time significant developments have ensued with significant reductions in exposure times [478–480] and the use of high power lasers as both ablative shock-drivers and synchronous generators of hot-plasmas which emit copious X-ray radiation [481–483]. However, it is the advent of 4th generation light sources such as LCLS that heralds significant new capability in this burgeoning area for a number of reasons, because the FEL as a source of X-rays for probing the shocked state has several key advantages over the utilisation of X-rays emitted from laser-generated plasmas. The peak spectral brightness of FEL sources is some nine orders of magnitude greater than a synchrotron source, or any incoherent laser-plasma source. In practice this translates to an X-ray pulse that can be tuned to be below 100 fs in duration, shorter than the period of the fastest phonon in the system: atomic motion is truly frozen during the diffraction process. The FEL sources are also tuneable in energy, and can now be monochromated to $\Delta\lambda/\lambda$ better than 10^{-4}. In contrast, quasi-monochromatic laser-plasma sources typically rely on emission from the set energies of the helium-like resonance lines of mid-Z elements, and suffer the disadvantage of being relatively broad (with $\Delta\lambda/\lambda$ typically 5×10^{-3}, due to emission from the intercombination line and dielectronic satellites), and also sit on a broad background of radiation produced by mechanisms such as bremsstrahlung. However, perhaps the greatest advantage of the FEL sources are that they are collimated and focusable. The geometric limitations of laser-plasma sources, where the X-rays are emitted into 4π steradians, constrain the shocked sample to be placed several cm from the source, and to limit divergence of the incident and diffracted X-rays, the shocked region (from which X-rays are to be diffracted) is typically 0.3 - 1 mm in diameter, with the laser beam for shock compression being focused to about 0.8 mm diameter. Dynamic compression of such a large area to high pressure for several nanoseconds requires considerable laser energy. Indeed, in the TPa experiments performed to date with such sources several kJ of laser energy have been required [484, 485]. The high brightness and focusability of the X-rays from FELs considerably reduces the requirements of the optical laser to produce a given shock pressure. Bright Debye-Scherrer rings can be obtained on a single shot from small X-ray spots whose size is in practice only limited by the grain size of the sample, and excellent data from 30-μm X-ray spots is common. This in turn means that the optical laser, used for ablative compression, can also be focused to a small spot and even allowing for considerable over-filling of the region probed by the X-rays can result in 2 - 3 orders of magnitude reduction in the laser energy needed. Indeed, in the work described in Section 6.5.2, close to 100 GPa pressures were reached for many tens of picoseconds with a laser energy of a mere 20 mJ [486], whereas recent experiments have attained diffraction from samples shocked for several nanoseconds to 0.35 TPa with just 25 J of laser energy [487].

6.5.2. Ultimate Strength under Compression

The vast reduction in required optical laser energy required for high pressure studies was evinced by the first shock experiment to be performed at LCLS, which had as its aim a measurement of the ultimate compressive strength of a simple crystal: copper. Copper is a face-centred-cubic crystal that does not undergo a solid-solid phase transition at any point on the Hugoniot. Although the standard Hugoniot plots of materials on a P-V curve will show the response
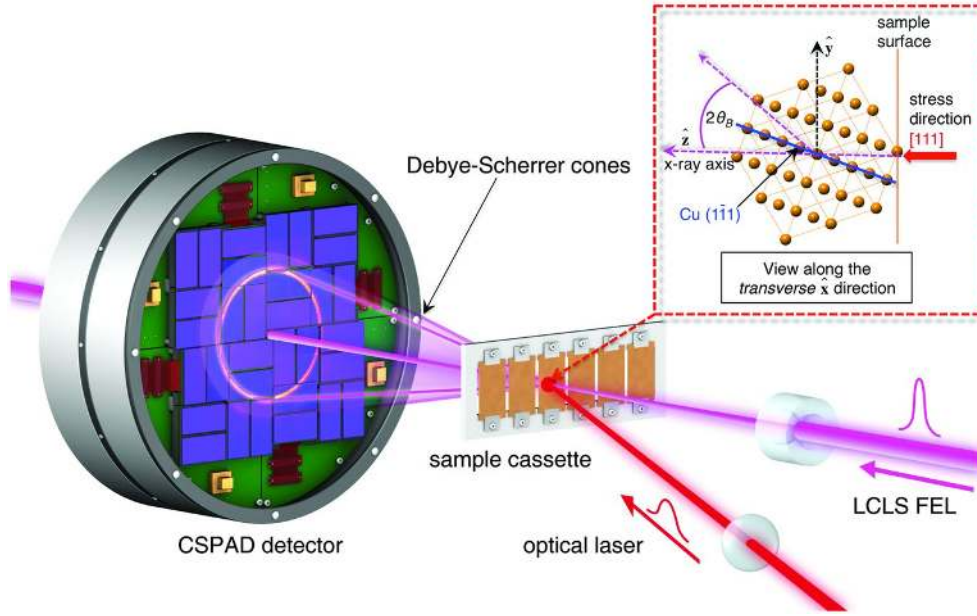
Figure 49. A schematic diagram of the experimental configuration for the experiment described in Section 6.5.2. An optical laser of pulselength 170 ps (FWHM) is focused to a 260 μm spot onto the surface a of 1 μm thick Cu film, which has been deposited on a silicon substrate. The polycrystalline Cu is textured such that the [111] directions are preferentially aligned along the surface normal. The short ($<$ 50 fs) pulses of X-rays (8 keV) from LCLS, in a spot 30-μm across, probe the lattice as it is compressed owing to laser-ablation of a surface layer of the Cu. A series of diffraction images are captured with differing delays between optical and X-ray beams, using a fresh area of the sample each time, building up a movie of the compression wave as it travels into the lattice. Figure (from [486]) reproduced with permission from *Science*, Copyright (2013) American Association for the Advancement of Science.

as being close to the hydrostat above the so-called Hugoniot Elastic Limit, the material must take some finite time to 'flow'. Indeed, the mechanisms by which such flow occurs is still a matter of active investigation. In a simple model of plasticity, due to Orowan, we assume the plastic strain rate is given by $\dot{\epsilon}^{\mathrm{p}} = N|\mathbf{b}|v$, where ϵ^{p} is the plastic strain, N the number of mobile dislocations moving at velocity v, and $\mathbf{b}$ their Burgers vector. However, it is known that the number of pre-existing defects is often too small to support the high plastic strain rates observed within a shock. Using multi-million atom molecular dynamics simulations, it was predicted that the time taken for the generation and motion of defects was such that if a metal could be compressed rapidly enough, the pre-existing defects would be unable to relieve the shear stress, and thus the material would compress elastically to extremely large compressions, at which point the lattice would 'fail' in a fundamental way (*i.e.* the ultimate elastic compression would be reached) with the generation of copious homogeneous dislocations [488]. Simulations indicated that this ultimate compressive strength corresponded to a one-dimensional compression of the unit cell of copper of order 15 - 17% (depending upon crystallographic direction) [489] and a purely elastic response up to this limit would be observed if the associated stress ($\approx$75

GPa) could be applied within a few tens of picoseconds.

The experiment undertaken to test this prediction, performed at LCLS, is shown schematically in Figure 49. A short laser pulse of 170 ps (FWHM) duration, containing just 20 mJ of energy, was focused onto the surface of a 1 μm thick layer of polycrystalline Cu, deposited in such a way that the crystallites had their [111] directions preferentially oriented along the normal to the target surface. The 8 keV X-rays were tuned to diffract from the [1$\bar{1}$1] planes. The change in Bragg angle upon compression leads to an expansion of the Debye-Scherrer ring. Elastic response (*i.e.* 1D compression of the unit cell) can be separated from plastic response (which for full relief of shear stress leads once more to a cubic lattice with reduced lattice spacing), owing to a large difference in the associated shifts in Bragg angle for the two different types of response. The shifts in Bragg angle are sensitive to elastic strains, and for an elastic strain along the shock direction, $\epsilon_{\mathrm{n}}^{\mathrm{e}}$, or perpendicular to that direction, $\epsilon_{\mathrm{t}}^{\mathrm{e}}$, the new Bragg angle, θ_{B}, is given by the solution to the quartic

$$\sin^4\theta_{\mathrm{B}}[(1+\epsilon_{\mathrm{n}}^{\mathrm{e}})^2-(1+\epsilon_{\mathrm{t}}^{\mathrm{e}})^2]+\sin^2\theta_{\mathrm{B}}[(1+\epsilon_{\mathrm{t}}^{\mathrm{e}})^2] = \sin^2\theta_0 \tag{39}$$

where θ_0 is the Bragg angle for the unshocked lattice [490].

For purely elastic response ($\epsilon_{\mathrm{t}}^{\mathrm{e}}{=}0$) in the limit

of small strains, taken to be positive in compression, the shift in the Bragg angle is given by $\Delta\theta = \sin^2\theta_0 \tan\theta_0 \ \epsilon_n^e$, whereas when sufficient plastic flow has occurred that the material is under close to hydrostatic conditions (*i.e.* $\epsilon_n^e = \epsilon_t^e$) the shift in Bragg angle is given by $\Delta\theta = \tan\theta_0 \ \epsilon_n^e$. Hence, as in the experiment $\sin^2\theta_0 = 0.115$, we see that the set-up is far more sensitive to strain once plastic flow occurs. A series of diffraction images, each taken with ≈ 50 fs X-ray pulses, delayed by the amount indicated with respect to the optical drive pulse, is shown in Figure 50. The initial elastic response can be observed as the distinct diffraction ring of slightly larger radius that is clearly visible at the time delays marked between 100 and 140 ps. Diffraction from the initially unshocked material (the inner ring) is still present as the compression wave has not traversed the full 1 μm thickness of the sample. The two snapshots, at 160 and 180 ps, show a much broader diffraction feature extending to far higher angles which is associated with the plastic response of the crystal.

The experimental data were extremely well-modelled by a very simple hydrocode [491] that included the non-linear elastic constants of the material and a generic Taylor-type model for plastic flow [492]. The agreement between the observed and predicted diffraction patterns demonstrates that the material had indeed reached the ultimate compressive strength at a strain of order 15-17% and then underwent plastic flow such that close to hydrostatic conditions were reached on a time-scale of order 60 ps – results that are also in good agreement with the type of response predicted from molecular dynamics simulations [488].
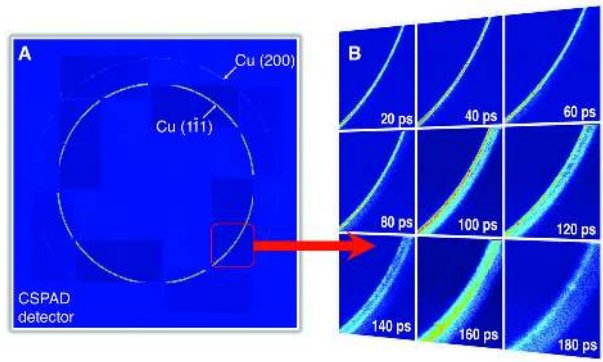

Figure 50. A series of Debye-Scherrer rings from 50 fs pulses of 8 keV X-rays diffracting from the [1$\bar{1}$1] planes of 1-μm thick copper samples depicted in Figure 49. In each inset the delay between the X-ray pulse and optical drive pulse is indicated. Figure (from [486]) reproduced with permission from *Science*, Copyright (2013) American Association for the Advancement of Science.

6.5.3. Phase Transitions, Melting and Recrystallization

The capabilities afforded by the femtosecond duration X-ray pulses are also ideal for studying shock-induced phase transitions and melting, and initial work has started in this area. Gorman and co-workers have studied the melting of Bi [493]. In this experiment the molten phase was not generated on compression but on release. The phase diagram of Bi is complex, with five distinct solid phases existing in the first few GPa above ambient pressure. The Hugoniot (the locus of states reached upon the passage of a single shock) is such that Bi shocked into the body-centred-cubic phase V is sufficiently heated that when released (which is deemed to be isentropic) it could relax into the liquid phase. The indirect nature of previous measurements had meant that the time scale of melting in Bi was poorly constrained, with inferred melting times ranging from tens to hundreds of nanoseconds [494, 495], much longer than the few nanoseconds typical of laser-shock experiments.

The experimental data was obtained by laser-shocking the Bi to pressures of between 8 and 14 GPa. A few nanoseconds after release the diffraction pattern was dominated by a broad diffuse ring of scattering from liquid Bi. A weak Bi-V (110) peak was also observed, which originates from the remaining higher-pressure region of the sample as the release wave travels back towards the driven surface, together with a weak Bi-I (012) peak that most likely originates from that sample material that has been fully released to zero pressure by the rarefaction wave. Interestingly, the smoothness of the Deybe-Scherrer rings from the fully released Bi-I was very different to the highly textured rings of the starting material suggesting that the rapid release to ambient pressure results in the creation of very small, sub-micron, crystallites. Thus the experiment conclusively demonstrated the transformation from the solid state to the liquid on time-scales very much faster than previously believed.

More recently LCLS has been used to probe the shock-compression of graphite up to pressures in excess of 120 GPa. Evidence was seen of the conversion of the graphite to both the diamond and lonsdaleite phases [496], although this inference presently relies on the disappearance of diffraction signatures associated with graphite and on the persistence of a single Bragg peak associated with each of the other two phases of carbon respectively. Whilst more detailed structural information is required to understand fully this transition, the experiment once more provides evidence for the transformative capabilities that fourth generation sources are bringing to the field.

Reliable claims on the details of structures under dynamic compression require the collection

of diffraction data from multiple reflections, which can only be fully elucidated with improvements in experimental design and execution (and, in the future, with increases in X-ray energies, corresponding to sampling larger volumes of reciprocal space). With better target designs (for example using ablator materials to steepen-up a shock before it impinges upon the sample of interest) and better quality laser spot profiles, data of remarkable quality can now be collected. For example, Figure 51 shows a Rietveld refinement, of an incommensurate host-guest structure, to diffraction data collected from shock-compressed Sc at 51 GPa and ≈2000 K [497, 498]. The diffraction data were collected on the MEC beamline at LCLS using a single 80 fs X-ray pulse. The incommensurate structure, which comprises a 'host' framework and linear chains of 'guest' atoms that lie in channels through the host structure, was known to be the stable phase of Sc above 21 GPa at 300 K, but it was unknown whether phases with such complex structures could form on the nanosecond timescales of a shock compression experiment. Using the high-quality diffraction data it was not only possible to show that the host-guest structure was indeed formed at pressures above 46 GPa but also to show that the 1D chains of guest atoms were disordered at these P-T conditions, resulting in the disappearance of specific 'guest-only' Bragg peaks in the diffraction pattern. This is illustrated in the inset to Figure 51, which shows the locations of these reflections, which have indices $(hk0m)$ in the superspace formulism used to analyse aperiodic structures. The calculated diffraction patterns using both ordered and disordered models for the chains are shown, and it is clear that the fit of the data to the disordered model is significantly better. It should be noted that the quality of these data rivals that obtained on synchrotrons, and clearly demonstrates that complicated phase transitions can complete in the short timescale available under laser-shock compression. It is interesting to note that one advantage of the dynamic compression technique is the lack of the diamonds present within a static compression cell – the Compton scattering from which can often degrade the quality of the data.

The high temperatures and pressures generated upon the passage of a shock have also been shown to be capable of transforming an amorphous solid to a crystalline phase, again on nanosecond time-scales. Gleason and co-workers performed pump-probe X-ray diffraction measurements on shock-compressed fused silica, revealing an amorphous to crystalline high-pressure stishovite phase transition [499]. Using the size broadening of the diffraction peaks, the growth of nanocrystalline stishovite grains was resolved during the nanosecond timescale of the laser-shock

compression. The pertinent data are shown in Figure 52, where time-resolved diffraction patterns are shown for shock pressures ranging from 4 to 34 GPa. From an analysis of the peak widths as a function of time, it was concluded that the functional form of the grain growth was suggestive of homogeneous nucleation as the growth mechanism.

The experiments described above have enabled investigation of the response of relatively macroscopic pieces of matter to laser radiation, generally resulting in a shock. However, it should also be noted that the excellent temporal and spatial resolution afforded by FELs is also opening up study of the response of individual nanoparticles. To date the response of such nanocrystalline matter has been investigated under a variety of optical laser intensities, which, with increasing intensity, result in oscillations in strain within the particles [500], melting [501], and their disintegration [502]. In addition, the experiments described above have concentrated on an understanding of the mechanisms that occur at the lattice level and thus have centred on the use of in situ diffraction as the primary diagnostic. However, short pulse FELs do afford other means to investigate the response of matter to rapid compression, such as phase-contrast imaging [503].

6.5.4. Future Experiments and Quasi-Isentropic Compression

In the experiments published to date, little attention has been paid to the texture of the target – that is to say the orientation distribution function that describes the probability, in a polycrystalline sample, of finding a crystallite with a particular crystallographic orientation. In the experiments on the ultimate strength of copper, described in Section 6.5.2, the sample was highly textured, and polar plots were taken to ensure that, whilst the [111] axis of the grains was preferentially aligned along the surface normal, the range of angles around the normal over which a significant number of grains could be found was still sufficient to obtain a good diffraction signal under compression.

However, unless the texture of the target is taken into account and a good understanding of the mechanisms which can lead to texture changes in shocked targets is appreciated, given the limited coverage in solid angle that current detectors afford the loss of diffracted signal could potentially be misinterpreted. For example, in the experiment described in Section 6.5.2, the texture was used to ensure that diffraction from the [1\bar{1}1] planes would always occur, but this resulted in very weak diffraction from the [200] type planes, as can be seen in the left hand part of Figure 50. On the other hand, a
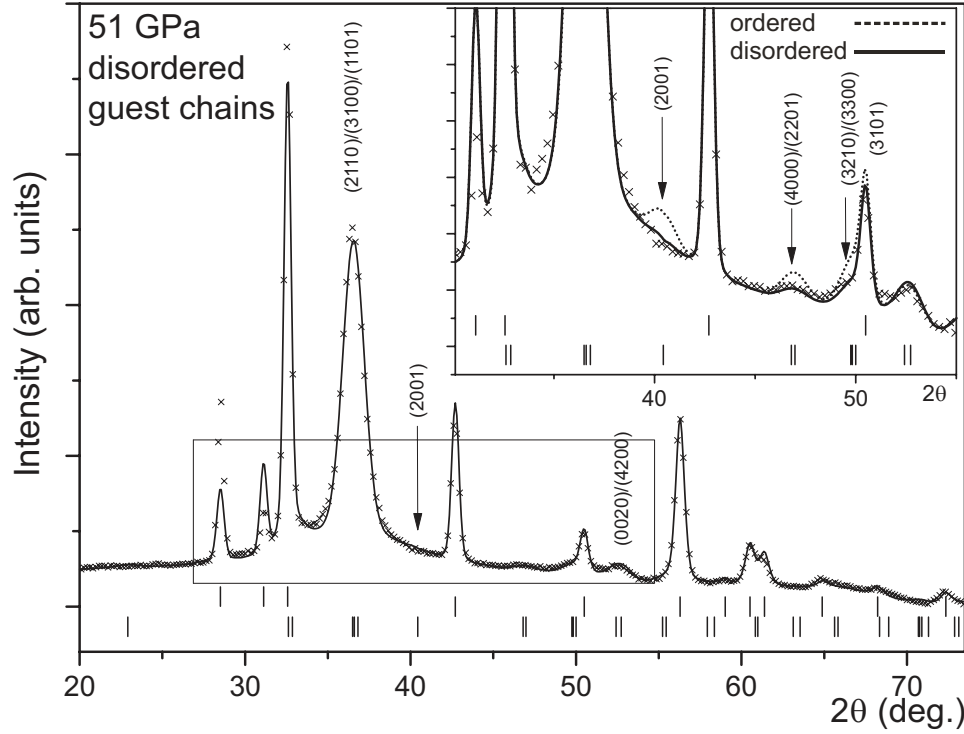
Figure 51. Diffraction of a single 80 fs pulse of 8.8 keV X-rays from Sc shock-compressed to 51 GPa, along with the associated Rietveld refinement. Image courtesy of reference [497].

target with known texture may aid in interpretation of the underlying physics. Indeed, it has recently been noted that much can be learnt about both deformation mechanisms and the pathways for phase transitions by deliberately choosing targets with certain textures.

An example of this is what can be learnt by the use of so-called fibre-geometry, where, owing to the underlying physics of the deposition mechanism, a polycrystalline film exhibits grain orientation. For example, grains with a particular lattice direction preferentially align along the sample surface normal but azimuthally around the surface normal the crystallite orientation is approximately random. For a completely randomly textured polycrystalline sample a particular set of Miller indices is distributed evenly over a sphere in reciprocal space (of radius the corresponding reciprocal lattice vector and named the Polanyi sphere). However, for a fibre-textured sample, rather than being distributed evenly over the Polanyi sphere, the regions of high diffraction probability form rings on its surface. It is where these rings intersect the Ewald sphere (the sphere of radius the k-vector of the incident X-rays) that diffraction occurs, leading to a distinct azimuthal dependence of the diffraction within the Debye-Scherrer rings. The azimuthal position of these diffraction spots can contain extremely useful information about plasticity (*e.g.* the degree of twinning) or the pathway for a phase transition, especially if the sample is aligned such that the surface normal of the target is not parallel or anti-parallel to the direction of the incident X-rays [504].

When considering future experiments, there is clearly much to be learnt in the field of shock physics. However, it should be noted that owing to the large temperature rises associated with the entropy rise across the shock front, the vast majority of solids melt upon shock compression at a pressure typically between 100 and 300 GPa, depending upon the material. In order for dynamic compression to be useful for studying solids at higher pressures, samples need to be compressed more slowly, such that the compression paths stay closer to an isentrope.

Such considerations lead naturally to the questions of how slow must compression be to prevent the full entropy (and thus heat) associated with the Hugoniot jump conditions being generated, and whether such timescales are compatible with the laser-compression facilities extant or envisaged at fourth generation light sources? That is to say, for a compression wave travelling in a solid, when is a wave a shock? If the response of a material were purely elastic in nature, the answer would be relatively simple. In such a case there are only two time-scales of relevance: the rise time of the shock and the minimum period of vibration within the solid (represented by the inverse of the Einstein or Debye frequencies). In

this case we have a simple physical picture: if a pair of atoms change their mean equilibrium position due to compression over many vibrational periods, the compression is close to isentropic. If, however, the thickness of the shock front approaches atomic dimensions, the change in mean spacing occurs on a timescale comparable to the shortest phonon period. In this case with the passage of the shock wave each atom in turn 'overshoots' its new mean position, resulting in a large rise in temperature. The validity of this interpretation has been verified by molecular dynamics (MD) simulations of shock propagation in copper [505]. Whilst such a simple physical picture can be painted for elastic response, in practice the defects present (and generated) within a material subjected to the high stresses of uniaxial compression allow the material to flow plastically or to change phase, as we have seen in the previous sections. In this case, it is envisaged that close to isentropic conditions can be met if the sample is compressed on a time-scale that is slow compared with the rise time of the shock for that given shock pressure. Shock rise-times are known empirically

Figure 52. Time-resolved X-ray diffraction patterns demonstrating the transformation of amorphous fused silica to Stishovite on nanosecond timescales. The Miller indices of the stishovite peaks are labelled at the top; ambient condition positions (grey dashed lines). Traces are clustered according to applied pressure where each colour indicates a different delay time (grey is X-ray only). Offset along the y axis is arbitrary for viewing clarity. Figure reproduced from reference [499]

(though without as yet a full explanation) to obey a fourth power law between stress and strain-rate known as the Swegle-Grady relation [506], and from such considerations in most cases tailored compression over a few nanoseconds should suffice to keep the sample solid. Indeed, this has already been confirmed using laser-plasma sources of diffraction, where samples of tin have been subjected to pressures of 1.2 TPa by ramp loading and have been shown to be still solid [485]. The results of experiments aimed at such ramp or quasi-isentropic compression, along with diagnosis *via* femtosecond diffraction using an X-ray FEL, have yet to be published. However, there can be little doubt that this is an area that will be explored in the future as the drive lasers and targets used become more sophisticated.

The present characteristics of high-power optical lasers placed at fourth generation sources is far from optimal. Although the optical laser at the MEC end-station at LCLS can deliver 30 J of laser energy in several nanoseconds, this not yet sufficient to obtain pressures in excess of a TPa over large enough sample areas to consider the system to be uniformly compressed. Furthermore, the laser is pumped by flash-lamps, limiting the shot rate to once every few minutes – a repetition rate that must be contrasted with the 120 Hz maximum repetition rate of the X-ray beam itself.

As a result, several facilities are looking for improved performance of the optical lasers. For example, the High Energy Density Science end-station at the European XFEL will be equipped with the DiPOLE system [507]. This is a diode-pumped laser, capable of producing shaped nanosecond pulses containing 100 J of 1030 nm light at a repetition rate of 10 Hz. Such parameters should allow the generation of solid state matter at pressures in excess of a TPa on a routine basis and will no doubt spur efforts to design systems to reach even more extreme conditions.

6.6. Solid Density Plasmas

6.6.1. Background
The study of high energy-density plasmas, characterized as systems at temperatures above 1 eV ($\sim$11600 K) and at densities at or above that of a typical solid (10^{22}–10^{23} atoms cm^{-3}), is of fundamental importance to pure and applied research ranging from geoscience and planetary physics to astrophysics, relativistic laser-matter interactions and fusion science. This is because dense plasmas are common throughout the universe (forming the cores of giant planets, brown dwarfs and stellar interiors), are commonly created transiently in all forms of intense laser-matter interactions and because of the importance of understanding the equation of state, material response and
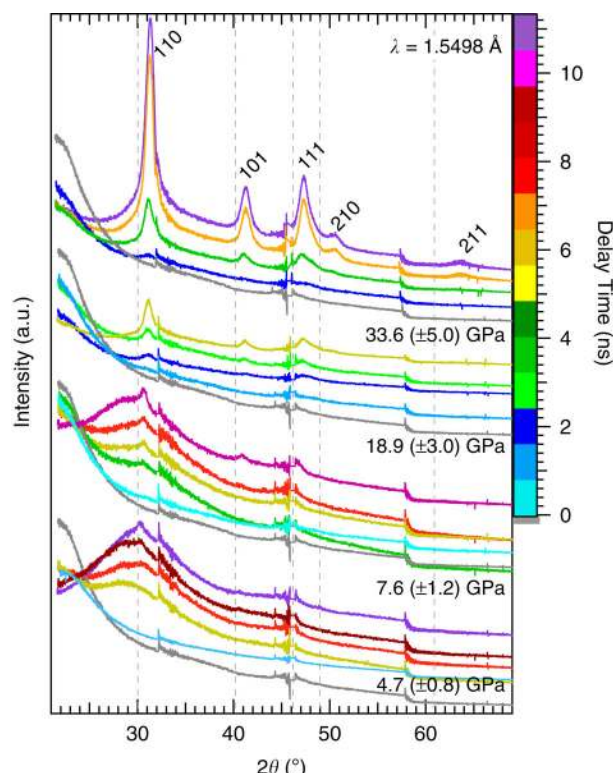
transport properties of systems in extreme conditions of temperature and density in the modelling, design and interpretation of inertial confinement fusion experiments.

Experimental research investigating the fundamental properties of high energy-density plasmas has historically been confronted by two major challenges. The first is the difficulty of creating simultaneously hot and dense plasmas, controllably, in homogeneous conditions over thermodynamically meaningful scales. The second is the requirement for diagnostics with sufficient spatial and temporal resolution to study the vast range of transient plasma dynamics ranging from attosecond electron processes all the way through to large atomic displacements and compressions taking place on nanosecond timescales. The requirement for diagnostics to be able to penetrate deep into a dense system further limits the available set of experimental techniques and makes (hard) X-rays particularly suitable for this line of research. In this context, the advent of high-brightness X-ray FELs has enabled a new class of experimental investigations into the physics of dense plasmas by providing novel ways to both create and diagnose plasmas, bridging the gap between plasma generation methods using high-power lasers and the refined diagnostic capabilities typical of synchrotron light sources [11, 508].

The first high energy-density experiments on FELs were conducted primarily on the XUV FLASH facility in Hamburg [1] and on the hard X-ray LCLS at SLAC [2]. The work undertaken has explored a range of systems driven to high temperatures on ultra-fast time scales by employing a variety of diagnostic techniques, from absorption and emission spectroscopy to inelastic X-ray scattering, thus providing novel insight into the structure and dynamics of dense plasmas. Here we review some of the recent achievements made in the field and highlight opportunities that FEL light sources offer to further our understanding of the physics of matter in extreme conditions.

6.6.2. X-ray Isochoric Heating

In terms of volumetric energy deposition, X-rays hold a key advantage over other energy sources (such as optical light or charged particle beams) due to their ability to penetrate deep into dense systems and their relatively straightforward interaction with matter. Heating systems with X-rays is therefore a promising method to generate high energy-density systems relatively homogeneously over large volumes. Although X-rays can penetrate dense systems, in the absence of non-linear effects such as saturable absorption, the energy deposition still decreases exponentially with depth inside an irradiated sample.

Therefore, to create longitudinally homogeneous samples *via* X-ray heating, either very thin targets or hard X-rays with low absorption cross sections must be used. X-ray FELs contain a sufficient number of photons in a single pulse to deposit on the order of a mJ of energy into a micron-sized sample, sufficient to create warm- and hot-dense plasmas. Because the pulse lengths of a typical FEL are below 100 fs, such an energy deposition process is also isochoric, taking place on time scales much shorter than that of hydrodynamic expansion, and the density of the system exposed remains unchanged during the X-ray absorption process. This opens new possibilities to create hot plasmas at precisely known densities, by irradiating solids, liquids or gases with the focused output of a bright X-ray FEL pulse.

The mechanism of X-ray isochoric heating and the homogeneity of the produced warm-dense plasma, was first experimentally investigated at LCLS by measuring the hydrodynamic expansion of a high energy density sample using space and time-resolved interferometry [509]. Here, a 0.5 μm thick Ag foil was irradiated by 8.9 keV photons at intensities around 5×10^{15} W cm^{-2} and heated to temperatures of order 10 eV at solid density. The expansion of the warm-dense system from the front and the back surfaces of the foil was measured and seen to be comparable within experimental uncertainty, indicating similar pressures throughout the target. The longitudinal homogeneity of the plasma was estimated to be on the order of 10%, providing the first direct experimental validation of X-ray isochoric heating using a femtosecond X-ray pulse and illustrating a new method to interrogate the equation of state of warm-dense systems in well-defined conditions.

The first hot-dense plasma experiments using an X-ray FEL were performed on the SXR (soft X-ray) beamline [511] of LCLS, where thin foils of aluminium were irradiated at photon energies between 1.5–2.0 keV at peak intensities up to 10^{17} W cm^{-2} [510]. This experiment successfully illustrated that ultra-short X-ray FEL pulses, when focused down to micron-sized spots, are capable of volumetrically heating plasmas to electron temperatures up to 200 eV in less than 100 femtoseconds, thus demonstrating X-ray isochoric heating to be an effective technique to create controllably extreme hot-dense plasmas. In these experiments the heating process is so fast that the ions remain relatively cold during the process, having little chance to move by an appreciable distance, so that the ion density of the system is well constrained to that of the solid sample during the X-ray pulse. The electron density, in turn, is determined by ionization and, at the densities of a typical metal, is sufficiently high to ensure that as soon as the system starts heating *via* X-ray
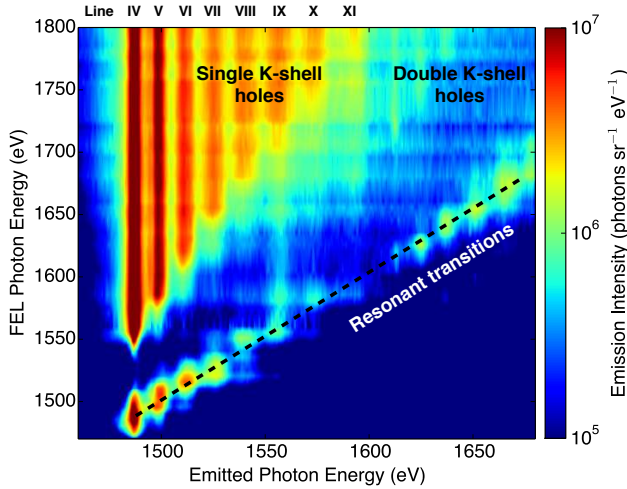
Figure 53. Charge-state-resolved measurement of the electronic structure in a hot-dense Al plasma *via* X-ray-driven emission spectroscopy [510]. Figure reproduced from ref. [508] with permission from the *Journal of Plasma Physics*, Copyright (2015) Cambridge University Press.

photo-absorption, electron collisional dynamics quickly starts dominating the various ionization processes (such as photoionization and Auger decay) in the system. Hence it was observed that a well-defined two-temperature plasma could be efficiently created on very short time scales containing cold ions, hot electrons, and a local thermodynamic equilibrium (LTE) ground-state ion charge distribution. These observations were supported by extensive non-LTE atomic kinetics modelling, which was able to simulate accurately the entire absorption and heating process with good predictive capability [512].

6.6.3. X-ray-driven Emission Spectroscopy

Diagnostic techniques based on X-ray emission and X-ray absorption spectroscopy form a cornerstone in plasma physics, capable of providing detailed information on radiative properties and on atomic and plasma structure over an extended range of temperatures and densities. The advent of X-ray FEL sources has not only made it possible to improve the quality of spectroscopic data using established methods but has also allowed for the development of new spectroscopic techniques which make use of the unique characteristics of the FEL pulse, namely the fine wavelength tunability, high brightness and small bandwidth. X-ray-driven emission spectroscopy is one such technique, where the X-ray photons can pump the core states of a plasma allowing core-level emission to take place in systems where (thermal) self-emission would otherwise not be observable. The narrow bandwidth can then be tuned to excite or ionize specific charge states or elements in the plasma,

providing a way to study selectively individual atomic or plasma processes.

This method was initially applied to isochorically heated Al plasmas on LCLS and provided a way to measure the electronic structure of individual Al charge states in the hot-dense plasma regime for the first time [510]. The main diagnostic used was K_α emission spectroscopy (2p→1s radiative recombination) in thermal plasmas at temperatures around 150 eV. While such temperatures are sufficient to create a hot-dense plasma, thermal ionization of the 1s state remained negligible leading to an absence of observable self-emission in the X-ray regime. However, by creating vacancies in the 1s states directly with the FEL pulse the charge state distribution (CSD) could be revealed as the plasma recombined, leading to very detailed spectroscopic information of the plasma structure. Importantly, as the core hole lifetimes are in the femtosecond regime, the measured spectrum corresponded to emission from a plasma at a well-known (solid) density, before any thermal expansion could occur. The experimental result of such a measurement in Al is shown in Figure 53. This illustrates the emission from ions of increasing ionization depending on the photon energy of the X-ray FEL pump. Here, line IV corresponds to emission from a core-hole Al ion with a full L-shell (all 8 electrons present in the 2s and 2p orbitals in the initial state) and all ions up to line XI, which corresponds to a He-like ion with only one electron left in the L-shell are observed. Resonance emission is observed when the FEL is tuned to the energy separation between two bound states, and, among others, provides further proof that the CSD is generated collisionally rather than dictated by X-ray photoionization [513].

The capability to determine the structure of a well-defined plasma system using X-ray spectroscopy enabled the first direct experimental measurement of ionization potential depression (IPD) due to a dense plasma environment [514]. This is a fundamental plasma property determining the level by which neighbouring charges affect the binding energy of electrons in ions, crucial for determination of the electron equation of state and of all radiative and transport properties in the dense plasma regime. Importantly, the measurement showed significant disagreement with popular IPD models used in the broad plasma community and has spurred renewed theory effort [515–518] which is summarized in Figure 54. Subsequent experiments using the same diagnostic technique for Mg and Si have confirmed these findings and have elucidated further discrepancies in material compounds, illustrating the importance of accurate experimental data to guide theoretical and computational efforts [519].

The combination of high brightness and tuneable narrow bandwidth of the X-ray FEL pulse has enabled spectroscopic investigations not only into the structure of plasmas but also into ultra-fast processes governed by electron impact ionization. By tuning the pump X-ray photon energy to lie between the ionization thresholds of two ions of neighbouring charge, a method to measure ultra-fast electron collisional ionization rates was recently proposed based on gating collisions in core-hole ions by Auger decay [520]. The measured rates were reported to be several times larger than predicted by standard models for systems at solid density and temperatures in the range 30-40 eV. Given the ultrafast time scales of Auger decay, this technique illustrates a novel way to access the regime of attosecond electron interactions without requiring any specific time resolution in the spectroscopic instrumentation.

6.6.4. Non-linear X-ray Processes and X-ray Scattering

At X-ray wavelengths the ponderomotive energy remains small even for the highest achievable intensities approaching 10^{20} W cm^{-2}, and the plasma non-linearities and hot-electron generation commonly observed at optical wavelengths are negligible. However, the high X-ray intensities afforded by FELs have led to the observation of several novel non-linear processes in X-ray driven dense plasmas. Cho and collaborators observed resonant processes, in highly-charged core-hole and double core-hole ions, generated and pumped on femtosecond time scales [513]. Recent measurements of the opacity of thin foils have shown saturable absorption effects well into the X-ray regime in both Fe [521] and Al [522] systems for the first time, a process more commonly associated with optical wavelengths. Unlike in the UV spectral range, where transient transparency is achieved by beating the Auger recombination rate and which requires very short and intense pulses [523], it turns out that saturable absorption is simpler to achieve in the X-ray regime since recombination of any core hole state rarely leads back to the original electron configuration in a single iteration. Perhaps counterintuitively, because Auger cascades in atoms are far more likely to ionize the system further on the short time scales of a typical FEL pulse, heavy atoms relax back to their ground state at a much slower rate than that suggested solely by recombination timescales for specific core levels.

Alongside providing new opportunities to create extreme states of matter, the bright pulses of FELs have also led to new diagnostic capabilities of dense plasma systems investigated *via* X-ray scattering techniques. The high brightness and small bandwidth afforded by FEL pulses make them ideally
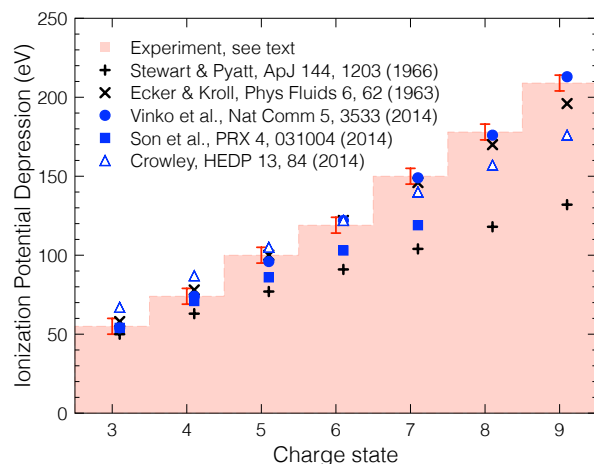

Figure 54. Comparison of ionization depression models and experimental measurements for a solid-density Al plasma. Experimental data taken from refs. [514, 519] and models from refs. [515–517, 524, 525]. Figure adapted from ref. [508].

suited to time-resolved elastic and inelastic X-ray scattering measurements of both plasma structure and dynamics. The first experiments using a FEL to probe dense plasma properties *via* Thomson scattering were performed on the FLASH FEL to investigate warm-dense hydrogen, both heated and probed by the extreme UV (EUV) pulse at a wavelength around 13.5 nm [526]. The scattering signal was used to determine the temperature and density conditions of the isochorically heated liquid H droplet and some insight was gained into the ultra-fast electron equilibration dynamics and impact ionization process. More recently, experiments successfully used a double EUV pulse configuration to perform a time-resolved measurement of isochorically heated warm-dense hydrogen, heated by the first pulse and probed by the second with a resolution of a few hundred femtoseconds. This generated not only a measurement of plasma conditions but also an electron-ion equilibration time of just under one picosecond [527]. Scattering experiments have now also been performed at LCLS using hard X-rays on systems both pumped by optical lasers or heated isochorically with the X-ray pulse itself, thus providing measurements of a range of plasma temperatures and densities, as well as of structure factors, transient phenomena, transport properties and phase transitions [528–530]. The recent development of self-seeding on LCLS allows bandwidths of $\sim 5 \times 10^{-5}$, 50 times smaller than that of a typical SASE FEL pulse [87], enabling not only the investigation of collective electron excitations (plasmons) in scattering experiments but also the capability to resolve ion-acoustic features directly [531].

6.6.5. Summary

The novel capabilities afforded by FEL light sources are having a significant impact on the study of dense plasmas, not only in terms of isochorically generating well-defined warm- and hot- dense systems, but also by enabling novel X-ray scattering and spectroscopic diagnostics to access the structure and dynamics of extreme states of matter with unprecedented spatial and temporal resolution. Further developments of both seeding techniques, to improve the power, coherence and bandwidth properties of FEL pulses, and of pump-probe schemes, exploiting either the FEL pulse itself or by combining it with high power laser sources, will be important in future investigations aimed at improving our understanding of hot dense plasmas.

6.7. Industrial Perspective

The use of short-wavelength FELs is presently dominated by fundamental research. Nevertheless there is huge potential for their application in industry. In this section an industrial perspective is given, with a focus on two particular areas. Section 6.7.1 gives a materials science and engineering viewpoint, highlighting the revolutionary capability provided by the high X-ray photon flux of FELs. Section 6.7.2 describes the direct application of short-wavelength FEL light for computer chip manufacture *via* EUV lithography, where FELs offer a significant power advantage over alternative sources.

6.7.1. Materials Science and Engineering

Globally, the metals industry is worth many billions of pounds, it directly employs hundreds of thousands of people and it includes a number of high profile, world-leading, aerospace, nuclear and automotive companies. Improving this position is far from trivial given the competitive nature of these global business sectors and the demand for improved environmental performance.

With respect to the aerospace sector specifically, the Advisory Council for Aeronautics Research in Europe (ACARE) has set a series of targets that industry and the regulatory bodies are committed to achieving [532]. Given the highly evolved nature of this sector it is clear that any technological advance requires significant scientific progress with respect to both experimental techniques and underpinning modelling work. This necessitates high levels of R&D spend. To this end in 2015 Rolls-Royce alone spent £1.2 bn on R&D [533] including longstanding critical activity on fundamental aspects of materials science [534, 535]. The potential market is large with ATI (the Aerospace Technology Institute) estimating market opportunities of > 30 bn *p.a.* in the 2020 to 2025 timeframe [536].

ACARE Flightpath 2050 targets are aggressive (relative to year 2000)

- Reduce overall CO_2 emissions per passenger kilometre by 75%.
- Reduce perceived noise levels by 65% of current average values.
- Reduce overall NO_x emissions by 90%.
- Aircraft taxiing movements to be emission free.
- Minimise the industries impact during manufacture, maintenance, overhaul, repair and disposal.

Engineering breakthroughs in these areas can only be achieved *via* a detailed and comprehensive understanding of the science that underpins the technology. Materials science is the prominent enabler for this and is dominated by the processes of phase transformation and deformation. During manufacture, these processes dictate the microstructure of the material. Since microstructure modification can typically increase the strength of a material by a factor of two-to-three, optimising the manufacturing route is clearly important with respect to subsequent component durability. The loading regimes in manufacture comprise complex combinations of strain (from uniaxial to tri-axial), temperatures (from cryogenic to $> 1400\,^\circ$C) and strain rates (spanning more than seven orders of magnitude). Dual phase flow and solidification during casting processes are also highly significant commercially but not well understood. Cooling rates on solidification or during solid-state processing span from sufficiently low to be near isothermal through to a rapid quench where 10^6 K s^{-1} is readily achievable. Towards the upper end of this range, transformations may not involve diffusion. The 10-100 nm length scales that often result from such transformations provide an important strengthening mechanism for most steels, nickel and titanium alloys. Similarly, machining processes provide an unusual combination of high strain-rate, high temperature gradient and high strain at the tool tip such that 'chip' formation is normally achieved by adiabatic shear. The ability to optimise tip geometry and coatings to achieve stable and robust machining process windows is of importance with respect to the surface condition of the substrate (particularly induced residual stress) and economics associated with manufacture.

For materials in-service the position is at least as complex with additional considerations of cyclic loading, environmental interaction (such as stress corrosion cracking), radiation damage / radio-chemistry (for nuclear power plant) and high strain rate events (including impact events such as bird strike or automotive crash). The main requirement for industry is predictive capability with an emphasis on mechanistic understanding of microstructure/property relationships.

Experimental techniques and instrumentation to enable this have seen outstanding progress in

recent years [537]. This has included *in-situ* loading experiments [538–540], the incorporation of electron backscatter detectors on scanning electron microscopes [541] and advances in, *inter alia*, high resolution transmission electron microscopy [542] and in Atom Probe Tomography [543]. Physics-based modelling is also making significant progress in this area but requires an understanding of the stack up of competing mechanisms often operating [544, 545]. However, with a few niche exceptions, all these techniques suffer from an inability to explore the important operative mechanisms with adequate temporal resolution. This is where X-ray FEL light sources are proving revolutionary [546].

Synchrotrons have enabled the *in-situ* measurement of strain evolution between, and within, crystals but the temporal resolution is limited as a result of the large test piece sizes that are required to capture relevant length-scale effects in the material. Sample sizes of several mm are not uncommon [547] and for X-ray dense materials very high photon fluxes are required in order to resolve subtle lattice strain changes under applied loading. This is particularly true for techniques that image microstructure in three dimensions and/or resolve lattice strain to high spatial resolution in volumes reasonably representative of bulk material that capture boundary and interface effects in poly-crystals [547, 548].

To capture pressure-induced phase transformations, twinning and dislocation motion, pump-probe experiments utilising an optical laser induced shock followed by diffraction imaging using an X-ray FEL offer the potential for revolutionary improvements in mechanistic understanding and, critically, development and validation of physics based models from atomistic to the crystal level [546].

From an industrial standpoint, the improved understanding and predictive capability arising from XFEL based study of engineering materials will enable improved product and reduced life-cycle cost. However, a significant and critical role exists for academia to provide the technical interface between large-scale facilities and industrial customers that lack the knowledge to configure the appropriate experiments and interpret the resulting data.

6.7.2. EUV Lithography

The drive towards ever smaller transistors over the last 50 years has led to extraordinary advances in the power of electronics, many examples of which are now woven into all aspects of every-day life and are considered indispensable. The decrease in transistor size has led to roughly a doubling of their chip packing density every two years – a trend commonly known as Moore's Law [549]. Though initially based on

observation, the continued fulfilment of Moore's Law became a major development target which has become increasingly difficult to meet.

The standard method for fabricating the components of integrated circuits is photolithography, whereby light is used to transfer a pattern from a mask to a light-sensitive chemical photo-resist on the surface of a semiconductor wafer. Present leading photolithography techniques use deep-ultraviolet excimer lasers typically operating at a wavelength of 193 nm, allowing minimum feature sizes down to approximately 30 nm [550]. To progress to successively smaller features below the scale of the laser wavelength requires increasingly complex and therefore slower and less cost-effective techniques. It has therefore been a long-standing goal to move to shorter wavelength sources and the next step has long been anticipated to be an EUV source operating at 13.5 nm [551]. The leading candidate for this is a laser-produced plasma (LPP) source [550] (as discussed in Section 6.5.1), which presently deliver power levels of $\gtrsim$100 W at 13.5 nm [552]. However, FELs are a very promising alternative due to their capability to deliver high average power (see Section 3.3) and their wavelength scaleablity (see Section 2.4), which would also offer a smooth upgrade path for potential future switches to even shorter wavelengths [550].

The possibility of using a FEL to generate 13.5 nm radiation for lithography is therefore of interest to both the accelerator community and semiconductor industry [137–139, 553, 554]. Due to the relatively high capital cost of accelerator facilities it is expected that a FEL would need to generate an average power output of tens of kilowatts to give overall cost advantages over an LPP source [554]. Though the step to construct a purpose built FEL for lithography has not been taken, it is clear that relevant technology already exists. High average power FELs at longer wavelengths have been demonstrated, for example the JLab IR Upgrade FEL achieved continuous >10 kW operation at 1.6 μm [555, 556], in an oscillator FEL configuration with efficiency > 1%. The wavelength range for EUV lithography is already easily demonstrated in FELs but in the single-pass high-gain mode with efficiency typically an order of magnitude lower than the JLab IR case. Producing a FEL for industry therefore presents a requirement to increase FEL efficiency and/or electron beam current, together with additional challenges in terms of long-term stability and reliability.

A new source of high intensity EUV radiation also presents major technical challenges in its integration with the required lithography techniques and its adoption will ultimately be a complex decision involving costs, timescales, and risk. Worldwide, the relevant communities have formed networks and

consortia and it is the role of these to identify, and address, the challenges of utilising short-wavelength FELs for this technical sector.

7. Concluding Comments

Clearly, the science, technology and applications of FELs have generated considerable developments on all fronts as evinced by the large annual publication rate and the wide-ranging and vibrant nature of the publications involved.

The aim of the review has been to present a representative sample of highlights and to provide references to enable those who want to know more with the information to help them pursue their interests further. It is inevitable that difficult choices have had to be made; some FEL application areas have not been included while others have not received the space that they perhaps merit. Nevertheless, a wide range of topics has received attention and experts who have worked on the design of FELs or who have performed experiments on a range of different FELs have been drawn-in to contribute in order to provide a balanced, diverse coverage. This leads to some variations in style but every attempt has been made to ensure clarity. Links between scientific applications and the fundamental properties of the FEL radiation that enables them have been highlighted where appropriate and markers have been laid where future developments can be foreseen.

In terms of FEL sources, since X-ray FELs first became available to users many new operating modes have been introduced. All of these in some way enhance the output properties of the light and enable new applications. However, there is still a catalogue of creative ideas for further manipulation of the FEL process, to enable for example, order-of-magnitude increases in the output power, reduction in the pulse duration towards the zeptosecond scale and further control of spectral properties and polarisation. Such potential future developments have been discussed in order to give a broad picture of how X-ray FELs may continue to evolve into unique, customisable, tools for driving scientific progress.

In terms of FEL science, there has been huge progress across all fields and further progress is anticipated as FEL technology and end-stations (including in detectors, algorithms and optical lasers) continue to mature. In particular though, studies of matter out-of-equilibrium stand-out and continued development of both seeding techniques (to improve the power, coherence and bandwidth properties of FEL pulses) and of pump-probe schemes will be important in future investigations.

It is significant to note that the rapid advancement of FEL science and technology has driven an increased worldwide demand for access to X-ray FELs. The governments of advanced economies recognising that national facilities lead not only to the advancement of science but also to the development of competitive advantage for the national industrial base, to the development of key technology and skills, and crucially that investment in this area is essential to remain competitive on the global stage [557].

References

[1] Ackermann W *et al.* 2007 Operation of a free-electron laser from the extreme ultraviolet to the water window *Nature Photonics* **1** 336 https://doi.org/10.1038/nphoton.2007.76

[2] Emma P *et al.* 2010 First lasing and operation of an angstrom-wavelength free-electron laser *Nature Photonics* **4** 641 https://doi.org/10.1038/nphoton.2010.176

[3] Ishikawa T *et al.* 2012 A compact X-ray free-electron laser emitting in the sub-angstrom region *Nature Photonics* **6** 540 https://doi.org/10.1038/nphoton.2012.141

[4] Allaria E *et al.* 2012 Highly coherent and stable pulses from the FERMI seeded free-electron laser in the extreme ultraviolet *Nature Photonics* **6** 699 https://doi.org/10.1038/nphoton.2012.233

[5] Feldhaus J *et al.* 2013 AMO science at the FLASH and European XFEL free-electron laser facilities *J. Phys. B: At. Mol. Opt. Phys.* **46** 164002 https://doi.org/10.1088/0953-4075/46/16/164002

[6] Piancastelli M N *et al.* 2010 Present trends and future perspectives for atomic and molecular physics at the new X-ray light sources *J. Elect. Spec. Relat. Phenom.* **181** 98 https://doi.org/10.1016/j.elspec.2010.05.010

[7] Bucksbaum P H and Glownia J 2013 Ultrafast AMO physics at the LCLS X-ray FEL *EPJ Web of Conferences* **57** 04001 https://doi.org/10.1051/epjconf/20135704001

[8] Yabashi M *et al.* 2013 Compact XFEL and AMO Sciences: SACLA and SCSS *J. Phys. B: At. Mol. Opt. Phys.* **46** 164001 https://doi.org/10.1088/0953-4075/46/16/164001

[9] Bostedt C *et al.* 2009 Experiments at FLASH *Nucl. Inst. Meth. Phys. Res. A* **601** 108 https://doi.org/10.1016/j.nima.2008.12.202

[10] Bostedt C *et al.* 2013 Ultra-fast and ultra-intense X-ray sciences: first results from the Linac Coherent Light Source free-elecon laser *J. Phys. B: At. Mol. Opt. Phys.* **46** 164003 https://doi.org/10.1088/0953-4075/46/16/164003

[11] Bostedt C *et al.* 2016 Linac Coherent Light Source: The first five years *Rev. Mod. Phys.* **88**(1) 015007 https://doi.org/10.1103/RevModPhys.88.015007

[12] Kang H S, Kim K W and Ko I S 2015 Status of PAL-XFEL *Proc. SPIE* **9512** 95120P http://dx.doi.org/10.1117/12.2183141

[13] Ganter R *et al.* 2012 SwissFEL Conceptual Design Report https://www.psi.ch/swissfel/CurrentSwissFELPublicationsEN/SwissFEL_CDR_V20_23.04.12_small.pdf

[14] Altarelli M *et al.* 2007 XFEL: The European X-ray free-electron laser technical design report https://doi.org/10.3204/DESY_06-097

[15] Schoenlein R W *et al.* New Science Opportunities Enabled by LCLS-II X-ray Lasers https://portal.slac.stanford.edu/sites/lcls_public/Documents/LCLS-IIScienceOpportunities_final.pdf

[16] Huang Z and Kim K J 2007 Review of X-ray free-electron laser theory *Phys. Rev. ST Accel. Beams* **10**(3) 034801 https://doi.org/10.1103/PhysRevSTAB.10.034801

[17] Barletta W *et al.* 2010 Free electron lasers: Present status and future challenges *Nucl. Instr. Meth. Phys. Res. Sect. A* **618** 69 https://doi.org/10.1016/j.nima.2010.02.274

[18] McNeil B W J and Thompson N R 2010 X-ray Free-Electron Lasers *Nature Photonics* **4** 814 https://doi.org/10.1038/nphoton.2010.239

[19] Pellegrini C, Marinelli A and Reiche S 2016 The physics of x-ray free-electron lasers *Rev. Mod. Phys.* **88**(1) 015006 https://doi.org/10.1103/RevModPhys.88.015006

[20] Schmüser P *et al.* 2014 *Free-Electron Lasers in the Ultraviolet and X-Ray Regime: Physical Principles, Experimental Results, Technical Realization* (Springer International Publishing, Switzerland) https://doi.org/10.1007/978-3-319-04081-3

[21] Saldin E L, Schneidmiller E A and Yurkov M V 2000 *The Physics of Free Electron Lasers* (Springer-Verlag Berlin Heidelberg) https://doi.org/10.1007/978-3-662-04066-9

[22] Freund H and Antonsen T 1992 *Principles of Free-Electron Lasers* (Chapman & Hall, London) https://doi.org/10.1007/978-94-011-2316-7

[23] Kim K J, Huang Z and Lindberg R 2017 *Synchrotron Radiation and Free Electron Lasers, USPAS lecture notes* (to be published in Cambridge University Press)

[24] Motz H 1951 Applications of the radiation from fast electron beams *J. Appl. Phys.* **22** 527 https://doi.org/10.1063/1.1700002

[25] Kulipanov G N 2007 Ginzburg's invention of undulators and their role in modern synchrotron radiation sources and free electron lasers *Phys. Usp.* **50** 368 https://doi.org/10.1070/PU2007v050n04ABEH006237

[26] Motz H 1953 Experiments on radiation by fast electron beams *J. Appl. Phys.* **24** 826 https://doi.org/10.1063/1.1721389

[27] Phillips R M 1960 The Ubitron, a high-power traveling-wave tube based on a periodic beam 20 interaction in unloaded waveguide *IRE Trans. Electron Devices* **7** 231 https://doi.org/10.1109/T-ED.1960.14687

[28] Madey J 1971 Stimulated emission of bremsstrahlung in a periodic magnetic field *J. Appl. Phys.* **42** 1906 https://doi.org/10.1063/1.1660466

[29] Madey J M J 2014 Wilson prize article: From vacuum tubes to lasers and back again1 *Phys. Rev. ST Accel. Beams* **17**(7) 074901 https://doi.org/10.1103/PhysRevSTAB.17.074901

[30] Elias L *et al.* 1976 Observation of stimulated emission of radiation by relativistic electrons in a spatially periodic transverse magnetic field *Phys. Rev. Lett.* **36** 717 https://doi.org/10.1103/PhysRevLett.36.717

[31] Deacon D *et al.* 1977 First operation of a free-electron laser *Phys. Rev. Lett.* **38** 892 https://doi.org/10.1103/PhysRevLett.38.892

[32] Colson W 1977 One-body electrodynamics in a free electron laser *Phys. Lett. A* **64** 190 https://doi.org/10.1016/0375-9601(77)90712-5

[33] Hopf F A *et al.* 1976 Classical theory of a free electron laser *Phys. Rev. Lett.* **37** 1215 https://doi.org/10.1016/0030-4018(76)90283-2

[34] Kroll N and McMullin W 1978 Stimulated emission from relativistic electrons passing through a spatially periodic transverse magnetic field *Phys. Rev. A* **17** 300 https://doi.org/10.1103/PhysRevA.17.300

[35] Bernstein I and Hirshfield J 1979 Amplification on a relativistic electron beam in a spatially periodic transverse magnetic field *Phys. Rev. A* **20** 1661 https://doi.org/10.1103/PhysRevA.20.1661

[36] Sprangle P and Smith R 1980 Theory of free electron lasers *Phys. Rev. A* **21** 293 https://doi.org/10.1103/PhysRevA.21.293

[37] Kondratenko A and Saldin E 1980 Generation of coherent radiation by a relativistic electron beam in an ondulator *Part. Accel. 10* **10** 207 http://cds.cern.ch/record/1107977/files/p207.pdf

[38] Colson W 1981 The nonlinear wave equation for higher harmonics in free-electron lasers *IEEE J. Quant. Electron.* **17** 1417 https://doi.org/10.1109/JQE.1981.1071273

[39] Kroll N, Morton P and Rosenbluth M 1981 Free-electron lasers with variable parameter wigglers *IEEE J. Quant. Electron.* **17** 1436 https://doi.org/10.1109/JQE.1981.1071285

[40] Bonifacio R, Casagrande F and Casati G 1982 Cooperative and chaotic transition of a free electron laser Hamiltonian model *Opt. Commun.* **40** 219 https://doi.org/10.1016/0030-4018(82)90265-6

[41] Bonifacio R, Pellegrini C and Narducci L 1984 Collective instabilities and high-gain regime in a free electron laser *Opt. Commun.* **50** 373 https://doi.org/10.1016/0030-4018(84)90105-6

[42] Kim K J 1986 Three-Dimensional Analysis of Coherent Amplification and Self-Amplified Spontaneous Emission in Free-Electron Lasers *Phys. Rev. Lett.* **57**(15) 1871 https://doi.org/10.1103/PhysRevLett.57.1871

[43] Orzechowski T *et al.* 1985 Microwave radiation from a high-gain free-electron laser amplifier *Phys. Rev. Lett.* **54** 889 https://doi.org/10.1103/PhysRevLett.54.889

[44] Hogan M *et al.* 1998 Measurements of High Gain and Intensity Fluctuations in a Self-Amplified, Spontaneous-Emission Free-Electron Laser *Phys. Rev. Lett.* **80** 289 https://doi.org/10.1103/PhysRevLett.80.289

[45] Babzien M *et al.* 1998 Observation of self-amplified spontaneous emission in the near-infrared and visible wavelengths *Phys. Rev. E* **57**(5) 6093 https://doi.org/10.1103/PhysRevE.57.6093

[46] Milton S V *et al.* 2001 Exponential gain and saturation of a self-amplified spontaneous emission free-electron laser *Science* **292** 2037 https://doi.org/10.1126/science.1059955

[47] Tremaine A *et al.* 2002 Experimental characterization of nonlinear harmonic radiation from a visible self-amplified spontaneous emission free-electron laser at saturation *Phys. Rev. Lett.* **88**(20) 204801 https://doi.org/10.1103/PhysRevLett.88.204801

[48] Ayvazyan V *et al.* 2002 Generation of GW Radiation Pulses from a VUV Free-Electron Laser Operating in the Femtosecond Regime *Phys. Rev. Lett.* **88**(10) 104802 https://doi.org/10.1103/PhysRevLett.88.104802

[49] Pellegrini C 2012 The history of X-ray free-electron lasers *The European Physical Journal H* **37**(5) 659 https://doi.org/10.1140/epjh/e2012-20064-5

[50] Clarke J A 2004 *The Science and Technology of Undulators and Wigglers* (Oxford Univer-

sity Press) https://doi.org/10.1093/acprof:oso/9780198508557.001.0001

[51] Institute of Free Electron Laser, Osaka University Free electron laser figure http://www.fel.eng.osaka-u.ac.jp/FEL.html

[52] Colson W B, Dattoli G and Ciocci F 1985 Angular-gain spectrum of free-electron lasers *Phys. Rev. A* **31**(2) 828 https://doi.org/10.1103/PhysRevA.31.828

[53] Brau C 1990 *Free-Electron Lasers* (Academic Press, London)

[54] Palmer R B 1972 Interaction of relativistic particles and free electromagnetic waves in the presence of a static helical magnet *J. Appl. Phys.* **43** 3014 https://doi.org/10.1063/1.1661650

[55] Courant E D, Pellegrini C and Zakowicz W 1985 High-energy inverse free-electron-laser accelerator *Phys. Rev. A* **32**(5) 2813 https://doi.org/10.1103/PhysRevA.32.2813

[56] Arecchi F and Bonifacio R 1965 Theory of optical maser amplifiers *IEEE Journal of Quantum Electronics* **1** 169 https://doi.org/10.1109/JQE.1965.1072212

[57] Bonifacio R, Caloi R and Maroli C 1993 The slowly varying envelope approximation revisited *Optics Communications* **101** 185 https://doi.org/10.1016/0030-4018(93)90363-A

[58] McNeil B W J and Robb G R M 2002 Self-amplified coherent spontaneous emission in the planar wiggler free-electron laser *Phys. Rev. E* **65**(4) 046503 https://doi.org/10.1103/PhysRevE.65.046503

[59] Xie M 1995 Design optimization for an x-ray free electron laser driven by SLAC linac *Proceedings of the 1995 IEEE Particle Accelerator Conference* 183 https://doi.org/10.1109/PAC.1995.504603

[60] Reiche S 1999 GENESIS 1.3: a fully 3D time-dependent FEL simulation code *Nucl. Instr. Meth. Phys. Res. Sect. A* **429** 243 https://doi.org/10.1016/S0168-9002(99)00114-X

[61] Saldin E, Schneidmiller E and Yurkov M 1999 FAST: a three-dimensional time-dependent FEL simulation code *Nucl. Inst. Meth. Phys. Res. Sect. A* **429** 233 https://doi.org/10.1016/S0168-9002(99)00110-2

[62] Fawley W M 2004 A User Manual for GIN-GER and its Post-Processor XPLOTGIN Tech. Rep. LBNL-49625 Rev. 1 Paul Scherrer Institut http://www-ssrl.slac.stanford.edu/lcls/technotes/lcls-tn-04-3.pdf

[63] Freund H and van der Slot P 2014 MINERVA, a new code to model free-electron lasers *Proc. of 36th Int. Free-Electron Laser Conf., Basel* p 408 http://accelconf.web.cern.ch/AccelConf/FEL2014/papers/tup020.pdf

[64] Freund H and Yu L 1997 Comparison of wiggler-averaged and non-wiggler-averaged free-electron laser simulations *Nucl. Inst. Meth. Phys. Res. Sect. A* **393** 308 https://doi.org/10.1016/S0168-9002(97)00499-3

[65] Biedron S *et al.* 2000 Multi-dimensional free-electron laser simulation codes: a comparison study *Nucl. Inst. Meth. Phys. Res. Sect. A* **445** 110 https://doi.org/10.1016/S0168-9002(00)00124-8

[66] Giannessi L *et al.* 2011 Self-amplified spontaneous emission for a single pass free-electron laser *Phys. Rev. ST Accel. Beams* **14**(6) 060712 https://doi.org/10.1103/PhysRevSTAB.14.060712

[67] Marcus G *et al.* 2014 FEL Code Comparison for the Production of Harmonics via Harmonic Lasing *Proc. of 36th Int. Free-Electron Laser Conf., Basel* p 451 http://accelconf.web.cern.ch/AccelConf/FEL2014/papers/tup031.pdf

[68] Campbell L T and McNeil B W J 2012 PUFFIN: a three-dimensional, unaveraged free-electron laser simulation code *Phys. Plasmas* **19** 093119 https://doi.org/10.1063/1.4752743

[69] Bonifacio R *et al.* 1994 Spectrum, Temporal Structure and Fluctuations in a High-Gain Free-Electron Laser Starting from Noise *Phys. Rev. Lett.* **73**(1) 70 https://doi.org/10.1103/PhysRevLett.73.70

[70] Bonifacio R, McNeil B W J and Pierini P 1989 Superradiance in the high-gain free electron laser *Phys. Rev. A* **40**(8) 4467 https://doi.org/10.1103/PhysRevA.40.4467

[71] Reiche S *et al.* 2008 Development of ultra-short, single coherent spike for SASE X-ray FELs *Nucl. Inst. Meth. Phys. Res. Sect. A* **593** 45 https://doi.org/10.1016/j.nima.2008.04.061

[72] Saldin E L, Schneidmiller E A and Yurkov M V 2010 Statistical and coherence properties of radiation from x-ray free-electron lasers *New J. Phys.* **12** 035010 https://doi.org/10.1088/1367-2630/12/3/035010

[73] Ratner D *et al.* 2011 Second and third harmonic measurements at the linac coherent light source *Phys. Rev. ST Accel. Beams* **14**(6) 060701 https://doi.org/10.1103/PhysRevSTAB.14.060701

[74] Ischebeck R *et al.* 2003 Study of the transverse coherence at the TTF free electron laser *Nucl.*

Inst. Meth. Phys. Res. Sect. A **507** 175 https://doi.org/10.1016/S0168-9002(03)00866-0

[75] Vartanyants I A *et al.* 2011 Coherence Properties of Individual Femtosecond Pulses of an X-Ray Free-Electron Laser *Phys. Rev. Lett.* **107**(14) 144801 https://doi.org/10.1103/PhysRevLett.107.144801

[76] Sikorski M *et al.* 2014 Single Shot Coherence Properties of the Free-Electron Laser SACLA in the Hard X-ray Regime *Scientific Reports* **4**(5234) https://doi.org/10.1038/srep05234

[77] Di Mitri S 2015 On the importance of electron beam brightness in high gain free electron lasers *Photonics* **2** 317 https://doi.org/10.3390/photonics2020317

[78] Andruszkow J *et al.* 2000 First observation of self-amplified spontaneous emission in a free-electron laser at 109 nm wavelength *Phys. Rev. Lett.* **85**(18) 3825 https://doi.org/10.1103/PhysRevLett.85.3825

[79] Ayvazyan V *et al.* 2006 First operation of a free-electron laser generating GW power radiation at 32 nm wavelength *The European Physical Journal D - Atomic, Molecular, Optical and Plasma Physics* **37** 297 https://doi.org/10.1140/epjd/e2005-00308-1

[80] Schreiber S, Faatz B and Honkavaara K 2008 Operation of FLASH at 6.5nm Wavelength *Proc. of EPAC08* p 133 https://accelconf.web.cern.ch/accelconf/e08/papers/mopc030.pdf

[81] Schreiber S 2011 First Lasing in the Water Window with 4.1nm at FLASH *Proc. of FEL2011* p 164 https://accelconf.web.cern.ch/accelconf/FEL2011/papers/tuobi2.pdf

[82] Yu L H *et al.* 2000 High-Gain Harmonic-Generation Free-Electron Laser *Science* **289** 932 https://doi.org/10.1126/science.289.5481.932

[83] Shintake T *et al.* 2008 A compact free-electron laser for generating coherent radiation in the extreme ultraviolet region *Nature Photonics* **2** 555 https://doi.org/10.1038/nphoton.2008.134

[84] Shintake T 2006 Status of the SCSS Test Accelerator and XFEL Project in Japan *Proc. of EPAC2006* p 2741 http://accelconf.web.cern.ch/AccelConf/e06/PAPERS/THOPA02.PDF

[85] Feldhaus J *et al.* 1997 Possible application of X-ray optical elements for reducing the spectral bandwidth of an X-ray SASE FEL *Opt. Commun.* **140** 341 https://doi.org/10.1016/S0030-4018(97)00163-6

[86] Geloni G *et al.* 2011 A novel self-seeding scheme for hard X-ray FELs *Journal of Modern Optics* **58** 1391 https://doi.org/10.1080/09500340.2011.586473

[87] Amann J *et al.* 2012 Demonstration of self-seeding in a hard-X-ray free-electron laser *Nature Photonics* **6** 693 https://doi.org/10.1038/nphoton.2012.180

[88] Lutman A A *et al.* 2013 Experimental demonstration of femtosecond two-color x-ray free-electron lasers *Phys. Rev. Lett.* **110**(13) 134801 https://doi.org/10.1103/PhysRevLett.110.134801

[89] Emma P, Huang Z and Borland M 2004 Attosecond X-ray pulses in the LCLS using the slotted foil method *Proc. of FEL2004* p 333 https://accelconf.web.cern.ch/accelconf/f04/papers/TUBIS01/TUBIS01.PDF

[90] Hara T *et al.* 2013 Two-colour hard X-ray free-electron laser with wide tunability *Nature Communications* **4** 3919 https://doi.org/10.1038/ncomms3919

[91] Allaria E *et al.* 2013 Two-colour pumpprobe experiments with a twin-pulse-seed extreme ultraviolet free-electron laser *Nature Communications* **4** 2476 https://doi.org/10.1038/ncomms3476

[92] Ratner D *et al.* 2015 Experimental demonstration of a soft x-ray self-seeded free-electron laser *Phys. Rev. Lett.* **114**(5) 054801 https://doi.org/10.1103/PhysRevLett.114.054801

[93] Svandrlik M *et al.* 2014 FERMI Status Report *Proc. of FEL2014* p 564 http://accelconf.web.cern.ch/AccelConf/FEL2014/papers/tup085.pdf

[94] Nuhn H D *et al.* 2015 Commissioning of the Delta Polarizing Undulator at LCLS *Proc. of FEL2015* http://accelconf.web.cern.ch/AccelConf/FEL2015/papers/wed01.pdf

[95] Lutman A A *et al.* 2016 Fresh-slice multicolour X-ray free-electron lasers *Nature Photonics* **10** 745 https://doi.org/10.1038/NPHOTON.2016.201

[96] Wang D *et al.* 2016 Soft X-ray Free-Electron Laser at SINAP *Proc. of IPAC2016* p 1028 http://accelconf.web.cern.ch/AccelConf/ipac2016/papers/tuza01.pdf

[97] Stupakov G 2009 Using the Beam-Echo Effect for Generation of Short-Wavelength Radiation *Phys. Rev. Lett.* **102** 1 https://doi.org/10.1103/PhysRevLett.102.074801

[98] Xiang D *et al.* 2010 Demonstration of the Echo-Enabled Harmonic Generation Technique for Short-Wavelength Seeded Free-Electron Lasers *Phys. Rev. Lett.* **115** 114801 https://doi.org/10.1103/PhysRevLett.105.114801

[99] Hemsing E *et al.* 2014 Beam by design: Laser manipulation of electrons in modern accelerators *Rev. Mod. Phys.* **86**(3) 897 https://doi.org/10.1103/RevModPhys.86.897

[100] Thompson N R, Dunning D J and McNeil B W J 2010 Improved Longitudinal Coherence in SASE FELs *Proc. of IPAC2010* p 2257 http://accelconf.web.cern.ch/AccelConf/IPAC10/papers/tupe050.pdf

[101] Wu J, Marinelli A and Pellegrini C 2012 Generation of Longitudinally Coherent Ultra High Power X-Ray FEL Pulses by Phase and Amplitude Mixing *Proc. of FEL 2012* https://accelconf.web.cern.ch/accelconf/FEL2012/papers/tupd07.pdf

[102] Xiang D *et al.* 2013 Purified self-amplified spontaneous emission free-electron lasers with slippage-boosted filtering *Phys. Rev. Spec. Top. Accel. Beams* **16** 010703 https://doi.org/10.1103/PhysRevSTAB.16.010703

[103] McNeil B W J, Thompson N R and Dunning D J 2013 Transform-Limited X-Ray Pulse Generation from a High-Brightness Self-Amplified Spontaneous-Emission Free-Electron Laser *Phys. Rev. Lett.* **110**(13) 134802 https://doi.org/10.1103/PhysRevLett.110.134802

[104] Clarke J A *et al.* 2014 CLARA conceptual design report *Journal of Instrumentation* **9** T05001 https://doi.org/10.1088/1748-0221/9/05/T05001

[105] Colella R and Luccio A 1984 Proposal for a free electron laser in the X-ray region *Opt. Commun.* **50** 41 https://doi.org/10.1016/0030-4018(84)90009-9

[106] Kim K J, Shvyd'ko Y and Reiche S 2008 A Proposal for an X-Ray Free-Electron Laser Oscillator with an Energy-Recovery Linac *Phys. Rev. Lett.* **100** 244802 https://doi.org/10.1103/PhysRevLett.100.244802

[107] Huang Z and Ruth R 2006 Fully Coherent X-Ray Pulses from a Regenerative-Amplifier Free-Electron Laser *Phys. Rev. Lett.* **96** 144801 https://doi.org/10.1103/PhysRevLett.96.144801

[108] McNeil B W J 1990 A simple model of the free electron laser oscillator from low into high gain *IEEE J. Quant. Electron.* **26** 1124 https://doi.org/10.1016/0168-9002(90)91237-6

[109] Faatz B *et al.* 1999 Regenerative FEL amplifier at the TESLA test facility at DESY *Nucl. Instr. Meth. Phys. Res. Sect. A* **429** 424 https://doi.org/10.1016/S0168-9002(99)00123-0

[110] McNeil B W J *et al.* 2007 A design for the generation of temporally-coherent radiation pulses in the VUV and beyond by a self-seeding high-gain free electron laser amplifier *New J. Phys.* **9** 239 https://doi.org/10.1088/1367-2630/9/7/239

[111] Nguyen D C *et al.* 1999 First lasing of the regenerative amplifier FEL *Nucl. Instr. Meth. Phys. Res. Sect. A* **429** 125 https://doi.org/10.1016/S0168-9002(99)00090-X

[112] Dunning D J *et al.* 2008 Short wavelength regenerative amplifier free electron lasers *Nucl. Instr. Meth. Phys. Res. Sect. A* **593** 116 https://doi.org/10.1016/j.nima.2008.04.045

[113] Dunning D J, McNeil B W and Thompson N R 2014 Towards zeptosecond-scale pulses from x-ray free-electron lasers *Physics Procedia* **52** 62 https://doi.org/10.1016/j.phpro.2014.06.010

[114] Ding Y *et al.* 2009 Measurements and Simulations of Ultralow Emittance and Ultrashort Electron Beams in the Linac Coherent Light Source *Phys. Rev. Lett.* **102**(25) 254801 https://doi.org/10.1103/PhysRevLett.102.254801

[115] Bonifacio R *et al.* 1994 Spectrum, temporal structure, and fluctuations in a high-gain free-electron laser starting from noise *Phys. Rev. Lett.* **73**(1) 70 https://doi.org/10.1103/PhysRevLett.73.70

[116] Saldin E L, Schneidmiller E A and Yurkov M V 2006 Self-amplified spontaneous emission FEL with energy-chirped electron beam and its application for generation of attosecond X-ray pulses *Phys. Rev. Spec. Top. Accel. Beams* **9** 1 https://doi.org/10.1103/PhysRevSTAB.9.050702

[117] Zholents A A and Zolotorev M S 2008 Attosecond x-ray pulses produced by ultra short transverse slicing via laser electron beam interaction *New J. Phys.* **10** 025005 https://doi.org/10.1088/1367-2630/10/2/025005

[118] Xiang D *et al.* 2012 Mode-locked multichromatic x rays in a seeded free-electron laser for single-shot x-ray spectroscopy *Phys. Rev. ST Accel. Beams* **15**(5) 050707 https://doi.org/10.1103/PhysRevSTAB.15.050707

[119] Ding Y *et al.* 2012 Femtosecond x-ray pulse characterization in free-electron lasers using a cross-correlation technique *Phys. Rev. Lett.* **109**(25) 254802 https://doi.org/10.1103/PhysRevLett.109.254802

[120] Giannessi L *et al.* 2011 Self-amplified spontaneous emission free-electron laser with an energy-chirped electron beam and undulator tapering

Phys. Rev. Lett. **106**(14) 144801 https://doi.org/10.1103/PhysRevLett.106.144801

[121] Marcus G *et al.* 2012 Time-domain measurement of a self-amplified spontaneous emission free-electron laser with an energy-chirped electron beam and undulator tapering *Appl. Phys. Lett.* **101** 134102 https://doi.org/10.1063/1.4754612

[122] Bonifacio R and Casagrande F 1985 The superradiant regime of a free electron laser *Nucl. Instr. Meth. Phys. Res. Sect. A* **239** 36 https://doi.org/10.1016/0168-9002(85)90695-3

[123] Giannessi L, Musumeci P and Spampinati S 2005 Nonlinear pulse evolution in seeded free-electron laser amplifiers and in free-electron laser cascades *J. Appl. Phys.* **98** 043110 https://doi.org/10.1063/1.2010624

[124] Watanabe T *et al.* 2007 Experimental Characterization of Superradiance in a Single-Pass High-Gain Laser-Seeded Free-Electron Laser Amplifier *Phys. Rev. Lett.* **98**(3) 034802 https://doi.org/10.1103/PhysRevLett.98.034802

[125] Labat M *et al.* 2011 High-gain harmonic-generation free-electron laser seeded by harmonics generated in gas *Phys. Rev. Lett.* **107**(22) 224801 https://doi.org/10.1103/PhysRevLett.107.224801

[126] Giannessi L *et al.* 2012 High-order-harmonic generation and superradiance in a seeded free-electron laser *Phys. Rev. Lett.* **108**(16) 164801 https://doi.org/10.1103/PhysRevLett.108.164801

[127] Giannessi L *et al.* 2013 Superradiant cascade in a seeded free-electron laser *Phys. Rev. Lett.* **110**(4) 044801 https://doi.org/10.1103/PhysRevLett.110.044801

[128] Zholents A A and Fawley W M 2004 Proposal for intense attosecond radiation from an x-ray free-electron laser *Phys. Rev. Lett.* **92**(22) 224801 https://doi.org/10.1103/PhysRevLett.92.224801

[129] Xiang D, Huang Z and Stupakov G 2009 Generation of intense attosecond x-ray pulses using ultraviolet laser induced microbunching in electron beams *Phys. Rev. ST Accel. Beams* **12**(6) 060701 https://doi.org/10.1103/PhysRevSTAB.12.060701

[130] Thompson N R and McNeil B W J 2008 Mode locking in a free-electron laser amplifier *Phys. Rev. Lett.* **100**(20) 203901 https://doi.org/10.1103/PhysRevLett.100.203901

[131] Dunning D J, McNeil B W J and Thompson N R 2013 Few-cycle pulse generation in an x-ray free-electron laser *Phys. Rev. Lett.* **110**(10) 104801 https://doi.org/10.1103/PhysRevLett.110.104801

[132] Prat E and Reiche S 2015 Simple Method to Generate Terawatt-Attosecond X-Ray Free-Electron-Laser Pulses *Phys. Rev. Lett.* **114**(24) 244801 https://doi.org/10.1103/PhysRevLett.114.244801

[133] Fawley W M 2015 FEL Prize Winner talk: Three-Plus Decades of Tapered Undulator FEL Physics *Proc. of FEL 2015* http://accelconf.web.cern.ch/AccelConf/FEL2015/papers/mob01.pdf

[134] Ratner D *et al.* 2013 FEL Gain Length and Taper Measurements at LCLS *Proc. of FEL 2009* p 221 https://accelconf.web.cern.ch/accelconf/FEL2009/papers/tuoa03.pdf

[135] Geloni G, Kocharyan V and Saldin E Scheme for generation of fully-coherent, TW power level hard X-ray pulses from baseline undulators at the European X-ray FEL https://arxiv.org/abs/1007.2743v1

[136] Fawley W M *et al.* 2011 Toward TW-Level, Hard X-ray Pulses at LCLS *Proc. of FEL 2011* p 160 http://accelconf.web.cern.ch/AccelConf/FEL2011/papers/tuoa4.pdf

[137] Pagani C *et al.* 2000 Design considerations of a MW-scale, high-efficiency, industrial-use, ultraviolet {FEL} amplifier *Nucl. Inst. Meth. Phys. Res. Sect. A* **455** 733 https://doi.org/10.1016/S0168-9002(00)00547-7

[138] Socol Y *et al.* 2011 Compact 13.5-nm free-electron laser for extreme ultraviolet lithography *Phys. Rev. ST Accel. Beams* **14**(4) 040702 https://doi.org/10.1103/PhysRevSTAB.14.040702

[139] Schneidmiller E A *et al.* 2012 Potential of the FLASH free electron laser technology for the construction of a kW-scale light source for next-generation lithography *Journal of Micro/Nanolithography, MEMS, and MOEMS* **11** 021122 https://doi.org/10.1117/1.JMM.11.2.021122

[140] Hajima R 2010 Energy recovery linacs for light sources *Reviews of Accelerator Science and Technology* **03** 121 https://doi.org/10.1142/S1793626810000397

[141] Rossbach J *et al.* 1997 Fundamental limitations of an X-ray FEL operation due to quantum fluctuations of undulator radiation *Nucl. Inst. Meth. Phys. Res. A* **393** 152 https://doi.org/10.1016/S0168-9002(97)00449-X

[142] McNeil B W J *et al.* 2006 Harmonic Lasing in a Free-Electron Laser Amplifier *Phys. Rev. Lett.* **96** 084801 https://doi.org/10.1103/PhysRevLett.96.084801

[143] Schneidmiller E A and Yurkov M V 2012 Harmonic lasing in x-ray free electron lasers *Phys. Rev. ST Accel. Beams* **15**(8) 080702 https://doi.org/10.1103/PhysRevSTAB.15.080702

[144] Lindberg R R *et al.* 2011 Performance of the x-ray free-electron laser oscillator with crystal cavity *Physical Review Special Topics - Accelerators and Beams* **14** 010701 https://doi.org/10.1103/PhysRevSTAB.14.010701

[145] Namkung W 2010 Review of third generation light sources *Proc. of IPAC 2010* p 2411

[146] Allaria E *et al.* 2014 Control of the polarization of a vacuum-ultraviolet, high-gain, free-electron laser *Phys. Rev.X* **4** 041040 https://doi.org/10.1103/PhysRevX.4.041040

[147] Fleischer A *et al.* 2014 Spin angular momentum and tunable polarization in high-harmonic generation *Nature Photonics* **8** 543 https://doi.org/10.1038/NPHOTON.2014.108

[148] Kfir O *et al.* 2015 Generation of bright phase-matched circularly polarized extreme ultraviolet high harmonics *Nature Photonics* **9** 99 https://doi.org/10.1038/NPHOTON.2014.293

[149] Hettel R 2014 Dlsr design and plans: an international overview *J. Synch. Rad.* **21** 843 https://doi.org/10.1107/S1600577514011515

[150] McPherson A *et al.* 1987 Studies of multiphoton production of vacuum-ultraviolet radiation in the rare gases *J. Opt. Soc. Am. B* **4** 595 https://doi.org/10.1364/JOSAB.4.000595

[151] Ferray M *et al.* 1988 Multiple-harmonic conversion of 1064 nm radiation in rare gases *J. Phys. B: At. Mol. Opt. Phys.* **21** L31 https://doi.org/10.1088/0953-4075/21/3/001

[152] Midorikawa K 2011 High-order harmonic generation and attosecond science *Jap. J. Appl. Phys.* **50** 090001 https://doi.org/10.1143/JJAP.50.090001

[153] Dromey B *et al.* 2007 Bright multi-kev harmonic generation from relativistically oscillating plasma surfaces *Phys. Rev. Lett.* **99** 085001 https://doi.org/10.1103/PhysRevLett.99.085001

[154] Popmintchev T *et al.* 2012 Bright Coherent Ultrahigh Harmonics in the keV X-ray Regime from Mid-Infrared Femtosecond Lasers *Science* **336** 1287 https://doi.org/10.1126/science.1218497

[155] Jakubczak K *et al.* 2011 Enhanced surface structuring by ultrafast XUV/NIR dual action

[156] Miao J *et al.* 2015 Beyond crystallography: Diffractive imaging using coherent x-ray light sources *Science* **348** 530 https://doi.org/10.1126/science.aaa1394

[157] Ding C *et al.* 2014 High flux coherent supercontinuum soft X-ray source driven by a single-stage, 10mJ, Ti:sapphire amplifier-pumped OPA *Optics Express* **22** 6194 https://doi.org/10.1364/OE.22.006194

[158] Wilmott P 2011 *An Introduction to Synchrotron Radiation:Techniques and Applications* (Wiley) https://doi.org/10.1002/9781119970958

[159] Ohashi H *et al.* 2013 Beamline mirrors and monochromator for X-ray free electron laser of SACLA *Nuclear Instruments & Methods In Physics Research Section A-Accelerators Spectrometers Detectors And Associated Equipment* **710** 139 https://doi.org/10.1016/j.nima.2012.10.094

[160] Tono K *et al.* 2013 Beamline, experimental stations and photon beam diagnostics for the hard x-ray free electron laser of SACLA *New Journal Of Physics* **15** 083035 https://doi.org/10.1088/1367-2630/15/8/083035

[161] Yabashi M, Tanaka H and Ishikawa T 2015 Overview of the SACLA facility *Journal of Synchrotron Radiation* **22** 477 https://doi.org/10.1107/S1600577515004658

[162] Nagler B *et al.* 2015 The Matter in Extreme Conditions instrument at the Linac Coherent Light Source *Journal of Synchrotron Radiation* **22** 520 https://doi.org/10.1107/S1600577515004865

[163] Alonso-Mori R *et al.* 2015 The X-ray Correlation Spectroscopy instrument at the Linac Coherent Light Source *Journal of Synchrotron Radiation* **22** 508 https://doi.org/10.1107/S1600577515004397

[164] Chollet M *et al.* 2015 The X-ray Pump-Probe instrument at the Linac Coherent Light Source *Journal of Synchrotron Radiation* **22** 503 https://doi.org/10.1107/S1600577515005135

[165] Ferguson K R *et al.* 2015 The Atomic, Molecular and Optical Science instrument at the Linac Coherent Light Source *Journal of Synchrotron Radiation* **22** 492 https://doi.org/10.1107/S1600577515004646

[166] Dakovski G L *et al.* 2015 The Soft X-ray Research instrument at the Linac Coherent Light source *Journal of Synchrotron Radiation* **22** 498 https://doi.org/10.1107/S160057751500301X

[167] Allaria E *et al.* 2010 The FERMI@Elettra free-electron-laser source for coherent X-ray physics: photon properties, beam transport system and applications *New J. Phys.* **12** 075002 https://doi.org/10.1088/1367-2630/12/7/075002

[168] Bostedt C *et al.* 2009 Experiments at FLASH *Nuclear Instruments & Methods In Physics Research Section A-Accelerators Spectrometers Detectors And Associated Equipment* **601** 108 https://doi.org/10.1016/j.nima.2008.12.202

[169] Tiedtke K *et al.* 2009 The soft x-ray free-electron laser FLASH at DESY: beamlines, diagnostics and end-stations *New Journal Of Physics* **11** 023029 https://doi.org/10.1088/1367-2630/11/2/023029

[170] Plönjes E *et al.* 2016 FLASH2: Operation, beamlines, and photon diagnostics *Proceedings of the 12th International Conference on Synchrotron Radiation Instrumentation – SRI2015* (Author(s)) pp 020008–5 http://dx.doi.org/10.1063/1.4952787

[171] Singer A *et al.* 2012 Spatial and temporal coherence properties of single free-electron laser pulses *Optics Express* **20** 17480 https://doi.org/10.1364/OE.20.017480

[172] Vartanyants I A *et al.* 2011 Coherence Properties of Individual Femtosecond Pulses of an X-Ray Free-Electron Laser *Physical Review Letters* **107** 144801 https://doi.org/10.1103/PhysRevLett.107.144801

[173] Gutt C *et al.* 2012 Single Shot Spatial and Temporal Coherence Properties of the SLAC Linac Coherent Light Source in the Hard X-Ray Regime *Physical Review Letters* **108** https://doi.org/10.1103/PhysRevLett.108.024801

[174] Lehmkühler F *et al.* 2014 Single Shot Coherence Properties of the Free-Electron Laser SACLA in the Hard X-ray Regime *Scientific Reports* **4** 5234 https://doi.org/10.1038/srep05234

[175] Altarelli M 2011 The European X-ray free-electron laser facility in Hamburg *Nuclear Instruments & Methods in Physics Research Section B-Beam Interactions with Materials and Atoms* **269** 2845 https://doi.org/10.1016/j.nimb.2011.04.034

[176] Kim J *et al.* 2015 Damage threshold of platinum/carbon multilayers under hard X-ray free-electron laser irradiation *Optics Express* **23** 29032 https://doi.org/10.1364/OE.23.029032

[177] Aquila A *et al.* 2015 Fluence thresholds for grazing incidence hard x-ray mirrors *Applied Physics Letters* **106** 241905 https://doi.org/10.1063/1.4922380

[178] Koyama T *et al.* 2015 Damage to inorganic materials illuminated by focused beam of x-ray free-electron laser radiation *SPIE Optics + Optoelectronics* ed Juha L, Bajt S and London R (SPIE) pp 951107–7 https://doi.org/10.1117/12.2182778

[179] Yumoto H *et al.* 2013 Focusing of X-ray free-electron laser pulses with reflective optics *Nature Photonics* **7** 43 https://doi.org/10.1038/nphoton.2012.306

[180] Yabashi M *et al.* 2014 Optics for coherent X-ray applications *Journal of Synchrotron Radiation* **21** 976 https://doi.org/10.1107/S1600577514016415

[181] Yamauchi K *et al.* 2002 Figuring with subnanometer-level accuracy by numerically controlled elastic emission machining *Rev. Sci. Inst.* **73** 4028 https://doi.org/10.1063/1.1510573

[182] Yamauchi K *et al.* 2003 Microstitching interferometry for x-ray reflective optics *Rev. Sci. Inst.* **74** 2894 https://doi.org/10.1063/1.1569405

[183] Mimura H *et al.* 2005 Relative angle determinable stitching interferometry for hard x-ray reflective optics *Rev. Sci. Inst.* **76** 045102 https://doi.org/10.1063/1.1868472

[184] Ishikawa T, Tamasaku K and Yabashi M 2005 High-resolution X-ray monochromators *Nucl. Inst. Meth. Phys. Res. Sect. A* **547** 42 https://doi.org/10.1016/j.nima.2005.05.010

[185] Follath R *et al.* 2016 Optical design of the ARAMIS-beamlines at SwissFEL *AIP Conference Proceedings* **1741** 020009 https://doi.org/10.1063/1.4952788

[186] Zhu D *et al.* 2014 Performance of a beam-multiplexing diamond crystal monochromator at the Linac Coherent Light Source *Rev. Sci. Inst.* **85** 063106 https://doi.org/10.1063/1.4880724

[187] Stoupin S *et al.* 2014 All-diamond optical assemblies for a beam-multiplexing X-ray monochromator at the Linac Coherent Light Source *J. Appl. Cryst.* **47** 1329 https://doi.org/10.1107/S1600576714013028

[188] Feng Y *et al.* 2015 Demonstration of simultaneous experiments using thin crystal multiplexing at the Linac Coherent Light Source *Journal of Synchrotron Radiation* **22** 626 https://doi.org/10.1107/S1600577515003999

[189] Dong X, Shu D and Sinn H 2016 Design of a cryocooled artificial channel-cut crystal monochromator for the European XFEL *Proceedings*

of the 12th International Conference on Synchrotron Radiation Instrumentation – SRI2015 (Author(s)) pp 040027–5 http://dx.doi.org/10.1063/1.4952899

[190] Shastri S D, Zambianchi P and Mills D M 2001 Dynamical diffraction of ultrashort X-ray free-electron laser pulses *Journal of Synchrotron Radiation* **8** 1131 https://doi.org/10.1107/S0909049501012390

[191] Shastri S D, Zambianchi P and Mills D M 2001 Femtosecond x-ray dynamical diffraction by perfect crystals *Proceedings of SPIE vol. 4143* pp 69–77 https://doi.org/10.1117/12.413681

[192] Bushuev V *et al.* 2011 Temporal and coherence properties of hard X-ray FEL radiation following Bragg diffraction by crystals *Proceedings of SPIE vol. 8141* pp 81410T–1–81410T–14 https://doi.org/10.1117/12.893054

[193] Bushuev V A 2008 Diffraction of X-ray free-electron laser femtosecond pulses on single crystals in the Bragg and Laue geometry *Journal of Synchrotron Radiation* **15** 495 https://doi.org/10.1107/S0909049508019602

[194] Heimann P A *et al.* 2011 Linac Coherent Light Source soft x-ray materials science instrument optical design and monochromator commissioning *Rev. Sci. Inst.* **82** 093104 https://doi.org/10.1063/1.3633947

[195] Schropp A *et al.* 2013 Full spatial characterization of a nanofocused x-ray free-electron laser beam by ptychographic imaging *Scientific Reports* **3** Article number: 1633 https://doi.org/10.1038/srep01633

[196] Inoue I *et al.* 2015 Characterizing transverse coherence of an ultra-intense focused X-ray free-electron laser by an extended Young's experiment *IUCrJ* **2** 620 https://doi.org/10.1107/S2052252515015523

[197] Tiedtke K *et al.* 2014 Absolute pulse energy measurements of soft x-rays at the Linac Coherent Light Source *Optics Express* **22** 21214 https://doi.org/10.1364/OE.22.021214

[198] Moeller S P *et al.* 2015 Pulse energy measurement at the SXR instrument *Journal of Synchrotron Radiation* **22** 606 https://doi.org/10.1107/S1600577515006098

[199] Tono K *et al.* 2011 Single-shot beam-position monitor for x-ray free electron laser *Rev. Sci. Inst.* **82** 023108 https://doi.org/10.1063/1.3549133

[200] Feng Y *et al.* 2011 A single-shot intensity-position monitor for hard x-ray FEL sources *Proceedings of SPIE vol. 8140* pp 81400Q–1–81400Q–6 https://doi.org/10.1117/12.893740

[201] Schlotter W F *et al.* 2012 The soft x-ray instrument for materials studies at the linac coherent light source x-ray free-electron laser *Rev. Sci. Inst.* **83** 043107 https://doi.org/10.1063/1.3698294

[202] Tanaka T *et al.* 2011 Improvement of a cryogenic radiometer for XFEL absolute intensity measurement *Nuclear Instruments and Methods in Physics Research, A* **659** 528 https://doi.org/10.1016/j.nima.2011.08.039

[203] Tanaka T *et al.* 2015 Room-temperature calorimeter for x-ray free-electron lasers *Rev. Sci. Inst.* **86** 093104 https://doi.org/10.1063/1.4929666

[204] Karvinen P *et al.* 2012 Single-shot analysis of hard x-ray laser radiation using a noninvasive grating spectrometer *Optics Letters* **37** 5073 https://doi.org/10.1364/OL.37.005073

[205] Makita M *et al.* 2015 High-resolution single-shot spectral monitoring of hard x-ray free-electron laser radiation *Optica* **2** 912 https://doi.org/10.1364/OPTICA.2.000912

[206] Feng Y *et al.* 2012 A hard x-ray transmissive single-shot spectrometer for FEL sources *Proceedings of SPIE vol. 8504* ed Moeller S P, Yabashi M and Hau-Riege S P (SPIE) pp 85040S–85040S–9 https://doi.org/doi:10.1117/12.930943

[207] Zhu D *et al.* 2012 A single-shot transmissive spectrometer for hard x-ray free electron lasers *Applied Physics Letters* **101** 034103 https://doi.org/10.1063/1.4736725

[208] Katayama T *et al.* 2016 A beam branching method for timing and spectral characterization of hard X-ray free-electron lasers *Structural Dynamics* **3** 034301 https://doi.org/10.1063/1.4939655

[209] Katayama T *et al.* 2013 Femtosecond x-ray absorption spectroscopy with hard x-ray free electron laser *Applied Physics Letters* **103** 131105 https://doi.org/10.1063/1.4821108

[210] Obara Y *et al.* 2014 Femtosecond time-resolved X-ray absorption spectroscopy of liquid using a hard X-ray free electron laser in a dual-beam dispersive detection method *Optics Express* **22** 1105 https://doi.org/10.1364/OE.22.001105

[211] Braune M *et al.* 2016 A non-invasive online photoionization spectrometer for FLASH2 *Journal of Synchrotron Radiation* **23** 10 https://doi.org/10.1107/S1600577515022675

[212] Dusterer S *et al.* 2014 Development of experimental techniques for the characterization of ultrashort photon pulses of extreme ultraviolet free-electron lasers *Physical Review Special Topics - Accelerators and Beams* **17** 120702 https://doi.org/10.1103/PhysRevSTAB.17.120702

[213] Ding Y *et al.* 2011 Femtosecond x-ray pulse temporal characterization in free-electron lasers using a transverse deflector *Physical Review Special Topics - Accelerators and Beams* **14** 120701 https://doi.org/10.1103/PhysRevSTAB.14.120701

[214] Behrens C *et al.* 2014 Few-femtosecond time-resolved measurements of X-ray free-electron lasers *Nature Communications* **5** Article number: 3762 https://doi.org/10.1038/ncomms4762

[215] Marinelli A *et al.* 2015 High-intensity double-pulse X-ray free-electron laser *Nature Communications* Article number: 6369 https://doi.org/10.1038/ncomms7369

[216] Juranić P N *et al.* 2014 High-precision x-ray FEL pulse arrival time measurements at SACLA by a THz streak camera with Xe clusters *Optics Express* **22** 30004 https://doi.org/10.1364/OE.22.030004

[217] Grguraš I *et al.* 2012 Ultrafast X-ray pulse characterization at free-electron lasers *Nature Photonics* **6** 852 https://doi.org/10.1038/nphoton.2012.276

[218] Helml W *et al.* 2014 Measuring the temporal structure of few-femtosecond free-electron laser X-ray pulses directly in the time domain *Nature Photonics* **8** 950 http://dx.doi.org/10.1038/nphoton.2014.278

[219] Duesterer S *et al.* 2011 Femtosecond x-ray pulse length characterization at the Linac Coherent Light Source free-electron laser *New Journal Of Physics* **13** 093024 https://doi.org/10.1088/1367-2630/13/9/093024

[220] Inubushi Y *et al.* 2012 Determination of the Pulse Duration of an X-Ray Free Electron Laser Using Highly Resolved Single-Shot Spectra *Physical Review Letters* **109** 144801 https://doi.org/10.1103/PhysRevLett.109.144801

[221] Minitti M P *et al.* 2015 Optical laser systems at the Linac Coherent Light Source *Journal of Synchrotron Radiation* **22** 526 http://dx.doi.org/10.1107/S1600577515006244

[222] Schulz S *et al.* 2013 Femtosecond-precision synchronization of the pump-probe optical laser for user experiments at FLASH *Proceedings of SPIE vol. 8778* pp 87780R–1–87780R–9 http://dx.doi.org/10.1117/12.2021572

[223] Schulz S *et al.* 2015 Femtosecond all-optical synchronization of an X-ray free-electron laser *Nature Communications* **6** 5938 http://dx.doi.org/10.1038/ncomms6938

[224] Allaria E *et al.* 2013 Two-stage seeded soft-X-ray free-electron laser *Nature Photonics* **7** 913 https://doi/doi:10.1038/nphoton.2013.277

[225] Allaria E *et al.* 2015 The FERMI free-electron lasers *Journal of Synchrotron Radiation* **22** 485 https://doi.org/10.1107/S1600577515005366

[226] Danailov M B *et al.* 2014 Towards jitter-free pump-probe measurements at seeded free electron laser facilities *Optics Express* **22** 12869 http://dx.doi.org/10.1364/OE.22.012869

[227] Bionta M R *et al.* 2014 Spectral encoding method for measuring the relative arrival time between x-ray/optical pulses *Rev. Sci. Inst.* **85** 083116 https://doi.org/10.1063/1.4893657

[228] Schorb S *et al.* 2012 X-ray–optical cross-correlator for gas-phase experiments at the Linac Coherent Light Source free-electron laser *Applied Physics Letters* **100** 121107 https://doi.org/10.1063/1.3695163

[229] Beye M *et al.* 2012 X-ray pulse preserving single-shot optical cross-correlation method for improved experimental temporal resolution *Applied Physics Letters* **100** 121108 https://doi.org/10.1063/1.3695164

[230] Harmand M *et al.* 2013 Achieving few-femtosecond time-sorting at hard X-ray free-electron lasers *Nature Photonics* **7** 215 https://doi.org/10.1038/nphoton.2013.11

[231] Hartmann N *et al.* 2014 Sub-femtosecond precision measurement of relative X-ray arrival time for free-electron lasers *Nature Photonics* **8** 706 https://doi.org/10.1038/nphoton.2014.164

[232] Chapman H N *et al.* 2006 Femtosecond diffractive imaging with a soft-X-ray free-electron laser *Nature Physics* **2** 839 https://doi.org/10.1038/nphys461

[233] Chapman H N *et al.* 2011 Femtosecond X-ray protein nanocrystallography *Nature* **470** 73 https://doi.org/10.1038/nature09750

[234] Schlichting I 2015 Serial femtosecond crystallography: the first five years *IUCrJ* **2** 246 https://doi.org/10.1107/S205225251402702X

[235] Spence J C H, Weierstall U and Chapman H 2012 X-ray lasers for structural and dynamic biology *Reports on progress in Physics* **75** 102601 https://doi.org/10.1088/0034-4885/75/10/102601

[236] Ribic P R and Margaritondo G 2012 Status and prospects of X-ray free-electron lasers (X-FELs): a simple presentation *J. Phys. D: Appl. Phys.* **45** 213001 https://doi.org/10.1088/0022-3727/45/21/213001

[237] Chapman H N, Caleman C and Timneanu N 2014 Diffraction before destruction *Phil. Trans. Roy. Soc. B* **369** 20130313 https://doi.org/10.1098/rstb.2013.0313

[238] Ihee H *et al.* 2010 Ultrafast X-ray scattering:structural dynamics from diatomic to protein molecules *Int. Rev. Phys. Chem.* **29** 453 https://doi.org/10.1080/0144235x.2010.498938

[239] 2014 Discussion Meeting Issue Biology with free-electron X-ray lasers organized and edited by John C. H. Spence and Henry N. Chapman *Phil. Trans. B* **369** http://rstb.royalsocietypublishing.org/content/369/1647

[240] Barty A *et al.* 2012 Self-terminating diffraction gates femtosecond X-ray nanocrystallography measurements *Nature Photonics* **6** 35 /https://doi.org/10.1038/nphoton.2011.297

[241] Weierstall U *et al.* 2014 Injector for scattering measurements on fully solvated biospecies *Rev. Sci. Inst.* **83** 035108 https://doi.org/10.1063/1.3693040

[242] Shapiro D A *et al.* 2008 Powder diffraction from a continuous microjet of submicrometer protein crystals *J. Synch. Rad.* **15** 593 https://doi.org/10.1107/S0909049508024151

[243] Kirian R A *et al.* 2010 Femtosecond protein nanocrystallography-data analysis methods *Optics Express* **18** 5713 https://doi.org/10.1364/OE.18.005713

[244] Millane R P and Lo L 2013 Iterative projection algorithms in protein crystallography. I.Theory *Acta Crystallograpica A* **69** 517 https://doi.org/10.1107/S0108767313015249

[245] Hawkes P W *et al.* 2007 *Science of microscopy* (New York: Springer) online ISBN: 978-0-387-49762-4

[246] Marchesini S 2007 Invited article: A unified evaluation of iterative projection algorithms for phase retrieval *Rev. Sci. Inst* **78** 011301 https://doi.org/10.1063/1.2403783

[247] Maia F R N C *et al.* 2010 Hawk: the image reconstruction package for coherent X-ray diffractive imaging *J. Appl. Cryst.* **43** 1535 https://doi.org/10.1107/S0021889810036083

[248] Hosseinizadeh A *et al.* 2015 Single-particle structure determination by X-ray free-electron lasers: Possibilities and challenges *Structural Dynamics* **2** 041601 https://doi.org/10.1063/1.4919740

[249] Ayyer K *et al.* 2016 *Dragonfly*: an implementation of the expand-maximize-compress algorithm for single-particle imaging *J. Appl. Cryst.* **49** 1320 https://doi.org/10.1107/S1600576716008165

[250] Wang D J *et al.* 2014 Double-focusing mixing jet for XFEL study of chemical kinetics *J. Synch. Rad.* **21** 1364 https://doi.org/10.1107/S160057751401858X

[251] Kupitz C *et al.* 2016 Structural Enzymology Using X-ray Free Electron Lasers *Struct. Dyn.* In press

[252] Pande K *et al.* 2016 Femtosecond structural dynamics drives the trans/cis isomerization in photoactive yellow protein *Science* **352** 725 https://doi.org/doi:10.1126/science.aad5081

[253] Kern J *et al.* 2015 Metalloprotein structures at ambient conditions and in real-time: biological crystallography and spectroscopy using X-ray free electron lasers *Curr. Opin. Struct. Bio.* **34** 87 https://doi.org/10.1016/j.sbi.2015.07.014

[254] Weierstall U *et al.* 2008 Droplet streams for serial crystallography of proteins *Exp. Fluids* **44** 675 https://doi.org/10.1007/s00348-007-0426-8

[255] Zhang H T *et al.* 2015 Structure of the angiotensin receptor revealed by serial femtosecond crystallography *Cell* **161** 833 https://doi.org/10.1016/j.cell.2015.04.011

[256] Weierstall U *et al.* 2014 Lipidic cubic phase injector facilitates membrane protein serial femtosecond crystallography *Nature Communications* **5** Article number: 3309 https://doi.org/10.1038/ncomms4309

[257] Nogly P *et al.* 2015 Lipidic cubic phase serial millisecond crystallography using synchrotron radiation *IUCrJ* **2** 168 https://doi.org/10.1107/S2052252514026487

[258] Conrad C E *et al.* 2015 A novel inert crystal delivery medium for serial femtosecond crystallography *IUCrJ* **2** 421 https://doi.org/10.1107/S2052252515009811

[259] Sugahara M *et al.* 2015 Grease matrix as a versatile carrier of proteins for serial crystallography *Nature Meth.* **12** 61 https://doi.org/10.1038/nmeth.3172

[260] Weierstall U 2014 Liquid sample delivery techniques for serial femtosecond crystallography

Phil. Trans. Roy. Soc. B **5** 369 https://doi.org/10.1038/ncomms4309

[261] Sierra R G *et al.* 2012 Nanoflow electrospinning serial femtosecond crystallography *Acta Crystallographica Section D-Biological Crystallography* **68** 1584 https://doi.org/10.1107/S0907444912038152

[262] Roedig P *et al.* 2016 Room-temperature macromolecular crystallography using a micropatterned silicon chip with minimal background scattering *J. Appl. Cryst.* **49** 968 https://doi.org/10.1107/S1600576716006348

[263] Mueller C *et al.* 2015 Fixed target matrix for femtosecond time-resolved and *in situ* serial micro-crystallography *Structural Dynamics-Us* **2** 054302 https://doi.org/10.1063/1.4928706

[264] Cohen A E *et al.* 2014 Goniometer-based femtosecond crystallography with X-ray free electron lasers *Proc. Natl. Acad. Sci. USA* **111** 17122 https://doi.org/10.1073/pnas.1418733111

[265] Oghbaey S *et al.* 2016 Fixed target combined with spectral mapping: approaching 100% hit rates for serial crystallography *Acta Crystallographica Section D: Structural Biology* **72** 944 https://doi.org/10.1107/S2059798316010834

[266] Kupitz C *et al.* 2014 Serial time-resolved crystallography of photosystem II using a femtosecond X-ray laser *Nature* **513** 261 https://doi.org/10.1038/nature13453

[267] Sauter N *et al.* 2016 No observable conformational changes in PSII *Nature* **533** E1 https://doi.org/10.1038/nature17983

[268] Liu W *et al.* 2016 Serial Femtosecond Crystallography of G ProteinCoupled Receptors *Science* **342** 1521 https://doi.org/10.1126/science.1244142

[269] White T A *et al.* 2016 Serial femtosecond crystallography datasets from G protein-coupled receptors *Sci. Data* 3:160057 https://doi.org/10.1038/sdata.2016.57

[270] Tenboer J *et al.* 2014 Time-resolved serial crystallography captures high-resolution intermediates of photoactive yellow protein *Science* **346** 1242 https://doi.org/10.1126/science.1259357

[271] Kang Y *et al.* 2015 Crystal structure of rhodopsin bound to arrestin by femtosecond X-ray laser *Nature* **523** 561 https://doi.org/10.1038/nature14656

[272] Zhou X E *et al.* 2016 X-ray laser diffraction for structure determination of the rhodopsin-arrestin complex *Scientific Data 3* 160021 https://doi.org/10.1038/sdata.2016.21

[273] Patterson B D 2014 Crystallography using an X-ray free-electron laser *Crystallography Reviews* **20** 242 https://doi.org/10.1080/0889311X.2014.939649

[274] Fromme P and Spence J C 2011 Femtosecond nanocrystallography using X-ray lasers for membrane protein structure determination *Curr. Opin. Struct. Bio.* **21** 509 https://doi.org/10.1016/j.sbi.2011.06.001

[275] Neutze R, Branden G and Schertler G 2015 Membrane protein structural biology using X-ray free electron lasers *Curr. Opin. Struct. Bio.* **33** 115 https://doi.org/10.1016/j.sbi.2015.08.006

[276] Spence J C H 2014 Approaches to time-resolved diffraction using an XFEL *Faraday Discussions* **171** 429 https://doi.org/10.1098/rstb.2013.0309

[277] Aquila A *et al.* 2012 Time-resolved protein nanocrystallography using an X-ray free-electron laser *Optics Express* **20** 2706 https://doi.org/10.1364/OE.20.002706

[278] Kern J *et al.* 2014 Taking snapshots of photosynthetic water oxidation using femtosecond X-ray diffraction and spectroscopy *Nature Communications* **5** 4371 https://doi.org/10.1038/ncomms5371

[279] Sauter N 2015 XFEL diffraction: developing processing methods to optimize data quality *J. Synch. Rad.* **22** 239 https://doi.org/10.1107/S1600577514028203

[280] White T A *et al.* 2016 Recent developments in *CrystFEL J. Appl. Cryst.* **49** 680 https://doi.org/10.1107/S1600576716004751

[281] Barty A *et al.* 2014 *Cheetah*: software for high-throughput reduction and analysis of serial femtosecond X-ray diffraction data *J. Appl. Cryst.* **47** 1118 https://doi.org/10.1107/S1600576714007626

[282] Levantino M *et al.* 2015 Ultrafast myoglobin structural dynamics observed with an X-ray free-electron laser *Nature Communications* 6772 https://doi.org/10.1038/ncomms7772

[283] Levantino M *et al.* 2015 Observing heme doming in myoglobin with femtosecond X-ray absorption spectroscopy *Structural Dynamics* 041713 https://doi.org/10.1063/1.4921907

[284] Ansari A *et al.* 1985 Protein states and Proteinquakes *Proc. Natl. Acad. Sci. U.S.A.* **82** 5000 https://doi.org/10.1073/pnas.82.15.5000

[285] Arnlund D *et al.* 2014 Visualizing a protein quake with time-resolved X-ray scattering at a free-electron laser *Nature Methods* **11** 923 https://doi.org/10.1038/nmeth.3067

[286] Kimura T *et al.* 2014 Imaging live cell in micro-liquid enclosure by X-ray laser diffraction *Nature Communications.* 7 https://doi.org/10.103/ncomms4052

[287] Luke D R 2005 Relaxed averaged alternating reflections for diffraction imaging *Inverse Problems* **21** 37 https://doi.org/10.1088/0266-5611/21/1/004

[288] Marchesini S *et al.* 2003 X-ray image reconstruction from a diffraction pattern alone *Phys. Rev. B* **68** 140101 https://doi.org/10.1103/PhysRevB.68.140101

[289] Martin A V *et al.* 2012 Noise-robust coherent diffractive imaging with a single diffraction pattern *Opt. Express* **20** 16650 https://doi.org/10.1364/OE.20.016650

[290] van der Schot G *et al.* 2015 Imaging single cells in a beam of live cyanobacteria with an X-ray Laser *Nature Communications* **6** https://doi.org/10.1038/ncomms6704

[291] van der Schot G *et al.* 2016 Open data set of live cyanobacterial cells imaged using an X-ray laser *Scientific Data* 3:160058 https://doi.org/10.1038/sdata.2016.58

[292] Sawaya M R *et al.* 2014 Protein crystal structure obtained at 2.9 A resolution from injecting bacterial cells into an X-ray free-electron laser beam *Proc. Natl. Acad. Sci. U.S.A.* **111** 12769 https://doi.org/10.1073/pnas.141345611

[293] Hantke M F *et al.* 2014 High-throughput imaging of heterogeneous cell organelles with an X-ray laser *Nature Photonics* **8** 943 https://doi.org/10.1038/nphoton.2014.270

[294] Hantke M F *et al.* 2016 A data set from flash X-Ray imaging of carboxysomes. *Scientific Data* **3** 160061 https://doi.org/10.1038/sdata.2016.61

[295] Seibert M *et al.* 2011 Single mimivirus particles intercepted and imaged with an X-ray laser *Nature* **470** 78 https://doi.org/10.1038/nature09748

[296] Ekeberg T *et al.* 2015 Three-dimensional reconstruction of the giant mimivirus particle with an X-ray free electron laser *Phys. Rev. Lett.* **114** 098102 https://doi.org/10.1103/PhysRevLett.114.098102

[297] Loh N D and Elsner V 2009 Reconstruction algorithm for single-particle diffraction imaging experiments *Phys. Rev.E* **80** 026705 https://doi.org/10.1103/PhysRevE.80.026705

[298] Loh N D *et al.* 2010 Cryptotomography: Reconstructing 3D Fourier intensities from randomly oriented single-shot diffraction pastterns *Phys. Rev. Lett.* **104** 225501 https://doi.org/10.1103/PhysRevLett.104.225501

[299] Lawrence R M *et al.* 2015 Serial femtosecond X-ray diffraction of enveloped virus microcrystals *Structural Dynamics-US* 041720 https://doi.org/10.1063/1.4929410

[300] Munke A *et al.* 2016 Coherent diffraction of single Rice Dwarf virus particles using hard X-rays at the Linac Coherent Light Source. *Sci. Data* **3** 160064 https://doi.org/10.1038/sdata.2016.64

[301] Saldin D K *et al.* 2011 New Light on Disordered Ensembles: *Ab Initio* Structure Determination of One Particle from Scattering Fluctuations of Many Copies *Phys. Rev. Lett.* **106** 115501 https://doi.org/10.1103/PhysRevLett.106.115501

[302] Wochner P *et al.* 2009 X-ray cross correlation analysis uncovers hidden local symmetries in disordered matter *Proc. Natl. Acad. Sci. USA* **106** 11511 https://doi.org/10.1073/pnas.0905337106

[303] Donatelli J J *et al.* 2015 Iterative phasing for fluctuation X-ray scattering *Proc. Natl. Acad. Sci. USA* **112** 10286 https://doi.org/10.1073/pnas.1513738112

[304] Starodub D *et al.* 2012 Single-particle structure determination by correlations of snapshot x-ray diffraction patterns *Nature Communications* **3** 1276 https://doi.org/10.1038/ncomms2288

[305] Pedrini B *et al.* 2013 Two-dimensional structure from random multiparticle X-ray scattering images using cross-correlations *Nature Communications* **4** 1647 https://doi.org/10.1038/ncomms2622

[306] Moffat K 2014 Time-resolved crystallography and protein design: signalling photoreceptors and optogenetics *Phil. Trans. Roy. Soc. B* **369** 20130568 https://doi.org/10.1098/rstb.2013.0568

[307] Scheres S H W 2012 RELION: Implementation of a Bayesian approach to cryo-EM structure determination *J. Struct. Bio.* **180** 519 https://doi.org/10.1016/j.jsb.2012.09.006

[308] Wabnitz H *et al.* 2002 Multiple ionization of atom clusters by intense soft X-rays from a free-electron laser *Nature* **420** 482 https://doi.org/10.1038/nature01197

[309] Sorokin A A *et al.* 2007 Photoelectric Effect at Ultrahigh Intensities *Phys. Rev. Lett.* **99** 213002 https://doi.org/10.1103/PhysRevLett.99.213002

[310] Richter M *et al.* 2009 Extreme Ultraviolet Laser Excites Atomic Giant Resonance *Phys. Rev. Lett.* **102** 163002 https://doi.org/10.1103/PhysRevLett.102.163002

[311] Berrah N and Fang L 2015 Chemical analysis: Double core-hole spectroscopy with free-electron Lasers *J. Elect. Spect. Relat. Phen.* **204** 284 https://doi.org/10.1016/j.elspec.2015.05.020

[312] Hishikawa A *et al.* 2011 Enhanced Nonlinear Double Excitation of He in Intense Extreme Ultraviolet Laser Fields *Phys. Rev. Lett.* **107** 243003 https://doi.org/10.1103/PhysRevLett.107.243003

[313] Ma R *et al.* 2013 Photoelectron angular distributions for the two-photon ionization of helium by ultrashort extreme ultraviolet free-electron laser pulses *J. Phys. B: At. Mol. Opt. Phys.* **46** 164018 https://doi.org/10.1088/0953-4075/46/16/164018

[314] Ishikawa K L and Ueda K 2012 Competition of Resonant and Nonresonant Paths in Resonance-Enhanced Two-Photon Single Ionization of He by an Ultrashort Extreme-Ultraviolet Pulse *Phys. Rev. Lett.* **108** 033003 https://doi.org/10.1103/PhysRevLett.108.033003

[315] Zitnik M *et al.* 2014 High Resolution Multiphoton Spectroscopy by a Tunable Free-Electron-Laser Light *Phys. Rev. Lett.* **113** 193201 https://doi.org/10.1103/PhysRevLett.113.193201

[316] Prince K *et al.* 2016 Coherent control with a short-wavelength free-electron laser *Nature Photonics* **10** 176 https://doi.org/doi:10.1038/nphoton.2016.13

[317] Fukuzawa H *et al.* 2010 Photoelectron spectroscopy of sequential three-photon double ionization of Ar irradiated by EUV free-electron laser pulses *J. Phys. B* **43** 111001 https://doi.org/10.1088/0953-4075/43/11/111001

[318] Hikosaka Y *et al.* 2010 Multiphoton Double Ionization of Ar in Intense Extreme Ultraviolet Laser Fields Studied by Shot-by-Shot Photoelectron Spectroscopy *Phys. Rev. Lett.* **105** 133001 https://doi.org/10.1103/PhysRevLett.105.133001

[319] Miyauchi N *et al.* 2011 Three-photon double ionization of Ar studied by photoelectron spectroscopy using an extreme ultraviolet free-electron laser: manifestation of resonance states of an intermediate Ar+ ion *J.*

Phys. B **44** 071001 https://doi.org/10.1088/0953-4075/44/7/071001

[320] Gryzlova E V *et al.* 2011 Doubly resonant three-photon double ionization of Ar atoms induced by an EUV free-electron laser *Phys. Rev. A* **84** 063405 https://doi.org/10.1103/PhysRevA.84.063405

[321] Berrah N *et al.* 2010 Non-linear processes in the interaction of atoms and molecules with intense EUV and X-ray fields from SASE free electron lasers (FELs) *J. Mod. Opt.* **57** 1015 https://doi.org/10.1080/09500340.2010.487946

[322] Motomura K *et al.* 2009 Multiple ionization of atomic argon irradiated by EUV free-electron laser pulses at 62 nm: evidence of sequential electron strip *J. Phys. B* **42** 221003 https://doi.org/10.1088/0953-4075/42/22/221003

[323] Kurka M *et al.* 2009 Two-photon double ionization of Ne by free-electron laser radiation: a kinematically complete experiment *J. Phys. B: At. Mol. Opt. Phys.* **42** 141002 https://doi.org/10.1088/0953-4075/42/14/141002

[324] Kurka M *et al.* 2010 Differential cross sections for non-sequential double ionization of He by 52 eV photons from the Free Electron Laser in Hamburg, FLASH *New J. Phys.* **12** 073035 https://doi.org/doi:10.1088/1367-2630/12/7/073035

[325] Rouzee A *et al.* 2011 Angle-resolved photoelectron spectroscopy of sequential three-photon triple ionization of neon at 90.5 eV photon energy *Phys. Rev. A* **83** 031401(R) https://doi.org/10.1103/PhysRevA.83.031401

[326] Sorokin A A *et al.* 2007 Photoelectric Effect at Ultrahigh Intensities *Phys. Rev. Lett.* **99** 213002 https://doi.org/10.1103/PhysRevLett.99.213002

[327] Makris M G *et al.* 2009 Theory of Multiphoton Multielectron Ionization of Xenon under Strong 93-eV Radiation *Phys. Rev. Lett.* **102** 033002 https://doi.org/10.1103/PhysRevLett.102.033002

[328] Gerken N *et al.* 2014 Time-Dependent Multiphoton Ionization of Xenon in the Soft-X-Ray Regime *Phys. Rev. Lett.* **112** 213002 https://doi.org/10.1103/PhysRevLett.112.213002

[329] Young L *et al.* 2010 Femtosecond electronic response of atoms to ultra-intense X-rays *Nature* **466** 56 https://doi.org/10.1038/nature09177

[330] Frasinski L J *et al.* 2013 Dynamics of Hollow Atom Formation in Intense X-Ray Pulses Probed by Partial Covariance Mapping *Phys. Rev.*

Lett. **111** 073002 https://doi.org/10.1103/PhysRevLett.111.073002

[331] Frasinski L J *et al.* 1989 Covariance Mapping: A Correlation Method applied to Multiphoton Multiple Ionization *Science* **246** 1029 https://doi.org/10.1126/science.246.4933.1029

[332] https://en.wikipedia.org/wiki/Covariance_mapping

[333] Rudek B *et al.* 2012 Ultra-efficient ionization of heavy atoms by intense X-ray free-electron laser pulses *Nature Photonics* **6** 858 https://doi.org/10.1038/nphoton.2012.261

[334] Ho P *et al.* 2014 Theoretical Tracking of Resonance-Enhanced Multiple Ionization Pathways in X-ray Free-Electron Laser Pulses *Phys. Rev. Lett.* **113** 253001 https://doi.org/10.1103/PhysRevLett.113.253001

[335] Fukuzawa H *et al.* 2013 Deep Inner-Shell Multiphoton Ionization by Intense X-Ray Free-Electron Laser Pulses *Phys. Rev. Lett.* **110** 173005 https://doi.org/10.1103/PhysRevLett.110.173005

[336] Tamasaku K *et al.* 2013 Double Core-Hole Creation by Sequential Attosecond Photoionization *Phys. Rev. Lett.* **111** 043001 https://doi.org/10.1103/PhysRevLett.111.043001

[337] Yamada A *et al.* 2010 Ion-ion coincidence studies on multiple ionizations of N_2 and O_2 molecules irradiated by extreme ultraviolet free-electron laser pulses *J. Chem. Phys.* **132** 204305 https://doi.org/10.1063/1.3436722

[338] Jiang Y H *et al.* 2009 Few-Photon Multiple Ionization of N_2 by Extreme Ultraviolet Free-Electron Laser Radiation *Phys. Rev. Lett.* **102** 123002 https://doi.org/10.1103/PhysRevLett.102.123002

[339] Kornilov O *et al.* 2013 Coulomb explosion of diatomic molecules in intense XUV fields mapped by partial covariance *J. Phys. B: At. Mol. Opt. Phys.* **46** 164028 https://doi.org/10.1088/0953-4075/46/16/164028

[340] Jiang Y H *et al.* 2013 Ultrafast dynamics in acetylene clocked in a femtosecond XUV stopwatch *J. Phys. B: At. Mol. Opt. Phys.* **46** 164027 https://doi.org/10.1088/0953-4075/46/16/164027

[341] Hoener M *et al.* 2010 Ultraintense X-Ray Induced Ionization, Dissociation, and Frustrated Absorption in Molecular Nitrogen *Phys. Rev. Lett.* **104** 253002 https://doi.org/10.1103/PhysRevLett.104.253002

[342] Fang L *et al.* 2010 Double Core-Hole Production in N_2: Beating the Auger Clock *Phys. Rev.* *Lett.* **105** 083005 https://doi.org/10.1103/PhysRevLett.105.083005

[343] Cryan J P *et al.* 2010 Auger Electron Angular Distribution of Double Core-Hole States in the Molecular Reference Frame *Phys. Rev. Lett.* **105** 083004 https://doi.org/10.1103/PhysRevLett.105.083004

[344] Cederbaum L S *et al.* 1986 On double vacancies in the core *J. Chem. Phys.* **85** 6513 https://doi.org/10.1063/1.451432

[345] Santra R, Kryzhevoi N V and Cederbaum L S 2009 X-Ray Two-Photon Photoelectron Spectroscopy: A Theoretical Study of Inner-Shell Spectra of the Organic Para-Aminophenol Molecule *Phys. Rev. Lett.* **103** 013002 https://doi.org/10.1103/PhysRevLett.103.013002

[346] Tashiro M *et al.* 2010 Molecular double core hole electron spectroscopy for chemical analysis *J. Chem. Phys.* **132** 184302 https://doi.org/10.1063/1.3408251

[347] Berrah N *et al.* 2011 Double-core-hole spectroscopy for chemical analysis with an intense X-ray femtosecond laser. *Proc. Natl. Acad. Sci. U.S.A.* **108** 16912 https://doi.org/10.1073/pnas.1111380108

[348] Salen P *et al.* 2012 Publishers Note: Experimental Verification of the Chemical Sensitivity of Two-Site Double Core-Hole States Formed by an X-Ray Free-Electron Laser [Phys. Rev. Lett. 108, 153003 (2012)] *Phys. Rev. Lett.* **108** 199903 https://doi.org/10.1103/PhysRevLett.108.199903

[349] Mucke M *et al.* 2015 Covariance mapping of two-photon double core hole states in C_2H_2 and C_2H_6 produced by an X-ray free electron laser *New J. Phys.* **17** 073002 https://doi.org/10.1088/1367-2630/17/7/073002

[350] Zhaunerchyk V *et al.* 2015 Disentangling formation of multiple-core holes in aminophenol molecules exposed to bright X-FEL radiation *J. Phys. B: At. Mol. Opt. Phys.* **48** 244003 https://doi.org/10.1088/0953-4075/48/24/244003

[351] Erk B *et al.* 2013 Ultrafast Charge Rearrangement and Nuclear Dynamics upon Inner-Shell Multiple Ionization of Small Polyatomic Molecules *Phys. Rev. Lett.* **110** 053003 https://doi.org/10.1103/PhysRevLett.110.053003

[352] Motomura K *et al.* 2015 Charge and Nuclear Dynamics Induced by Deep Inner-Shell Multiphoton Ionization of CH_3I Molecules by Intense X-ray Free Electron Laser Pulses *J. Phys. Chem. Lett.* **6** 2944 https://doi.org/10.1021/acs.jpclett.5b01205

[353] Nagaya K *et al.* 2016 Ultrafast Dynamics of a Nucleobase Analogue Illuminated by a Short Intense X-ray Free Electron Laser Pulse *Phys. Rev. X* **6** 021035 https://doi.org/10.1103/PhysRevX.6.021035

[354] Nagaya K *et al.* 2016 Femtosecond charge and molecular dynamics of I-containing organic molecules induced by intense X-ray free-electron laser pulses *Faraday Discussions* **194** 537 https://doi.org/10.1039/c6fd00085a

[355] Kierspel T *et al.* 2015 Stongly aligned gas-phase molecules at free-electron lasers *J. Phys. B: At. Mol. Opt. Phys.* **48** 204002 https://doi.org/10.1088/0953-4075/48/20/204002

[356] Hartmann N *et al.* 2014 Sub-femtosecond precision measurement of relative X-ray arrival time for free-electron lasers *Nature Photonics* **8** 706 https://doi.org/10.1038/nphoton.2014.164

[357] Erk B *et al.* 2014 Imaging charge transfer in iodomethane upon X-ray photoabsorption *Science* **345** 288 https://doi.org/10.1126/science.1253607

[358] Quiney H M and Nugent K A 2011 Biomolecular imaging and electronic damage using X-ray free-electron lasers *Nature Physics* **7** 142 https://doi.org/10.1038/nphys1859

[359] Barty A *et al.* 2012 Self-terminating diffraction gates femtosecond X-ray nanocrystallography measurements *Nature Photonics* **6** 35 https://doi.org/10.1038/nphoton.2011.297

[360] Hau-Riege S P 2012 Photoelectron Dynamics in X-Ray Free-Electron-Laser Diffractive Imaging of Biological Samples *Phys. Rev. Lett.* **108** 238101 https://doi.org/10.1103/PhysRevLett.108.238101

[361] Krainov V P and Smirnov M B 2002 Cluster beams in the super-intense femtosecond laser pulse *Physics Reports* **370** 237 https://doi.org/10.1016/S0370-1573(02)00272-7

[362] Ditmire T 1996 Interaction of intense laser pulses with atomic clusters *Phys. Rev.A* **53** 3379 https://doi.org/10.1103/PhysRevA.53.3379

[363] Santra R and Greene C 2003 Xenon Clusters in Intense VUV Laser Fields *Phys. Rev. Lett.* **91** 233401 https://doi.org/10.1103/PhysRevLett.91.233401

[364] Siedschlag C and Rost J M 2004 Small Rare-Gas Clusters in Soft X-Ray Pulses *Phys. Rev. Lett.* **93** 043402 https://doi.org/10.1103/PhysRevLett.93.043402

[365] Bauer D 2004 Small rare gas clusters in laser fields: ionization and absorption at long and short laser wavelengths *J. Phys. B: At. Mol. Opt. Phys.* **37** 3085 https://doi.org/10.1088/0953-4075/37/15/007

[366] Jungreuthmayer C *et al.* 2005 Intense VUV laser cluster interaction in the strong coupling regime *J. Phys. B: At. Mol. Opt. Phys.* **38** 3029 https://doi.org/10.1088/0953-4075/38/16/013

[367] Rusek M and Orlowski A 2005 Different mechanisms of cluster explosion within a unified smooth particle hydrodynamics Thomas-Fermi approach: Optical and short-wavelength regimes compared *Phys. Rev. A* **71** 043202 https://doi.org/10.1103/PhysRevA.71.043202

[368] Walters Z, Santra R and Greene C 2006 Interaction of intense vuv radiation with large xenon clusters *Phys. Rev. A* **74** 043204 https://doi.org/10.1103/PhysRevA.74.043204

[369] Georgescu I, Saalmann U and Rost J M 2007 Clusters under strong VUV pulses: A quantum-classical hybrid description incorporating plasma effects *Phys. Rev. A* **76**(4) 043203 https://doi.org/10.1103/PhysRevA.76.043203

[370] Laarmann T *et al.* 2005 Emission of Thermally Activated Electrons from Rare Gas Clusters Irradiated with Intense VUV Light Pulses from a Free Electron Laser *Phys. Rev. Lett.* **95** 063402 https://doi.org/10.1103/PhysRevLett.95.063402

[371] Ziaja B *et al.* 2008 Femtosecond non-equilibrium dynamics of clusters irradiated with short intense VUV pulses *New. J. Phys.* **10** 043003 https://doi.org/10.1088/1367-2630/10/4/043003

[372] Ziaja B *et al.* 2009 Energetics, Ionization, and Expansion Dynamics of Atomic Clusters Irradiated with Short Intense Vacuum-Ultraviolet Pulses *Phys. Rev. Lett.* **120** 205002 https://doi.org/10.1103/PhysRevLett.102.205002

[373] Fukuzawa H *et al.* 2009 Dead-time-free ion momentum spectroscopy of multiple ionization of Xe clusters irradiated by euv free-electron laser pulses *Phys. Rev. A* **79** 031201(R) https://doi.org/10.1103/PhysRevA.79.031201

[374] Iwayama H *et al.* 2009 Frustration of direct photoionization of Ar clusters in intense extreme ultraviolet pulses from a free electron laser *J. Phys. B: At. Mol. Opt. Phys.* **42** 134019 https://doi.org/10.1088/0953-4075/42/13/134019

[375] Iwayama H *et al.* 2010 Inhomogeneous charge redistribution in Xe clusters exposed to an intense extreme ultraviolet free electron laser *J. Phys. B: At. Mol. Opt. Phys.* **43** 161001 https://doi.org/10.1088/0953-4075/43/16/161001

[376] Sugishima A *et al.* 2012 Charge and energy transfer in argon-coreneon-shell clusters irradiated by free-electron-laser pulses at 62 nm *Phys.*

Rev. A **86** 033203 https://doi.org/10.1103/PhysRevA.86.033203

[377] Iwayama H *et al.* 2013 Towards coherent control of SASE pulses using propagation through helium gas at wavelengths corresponding to double excitation *J. Phys. B: At. Mol. Opt. Phys.* **46** 164019 https://doi.org/10.1088/0953-4075/46/16/164021

[378] Nagaya K *et al.* 2013 Unusual under-threshold ionization of neon clusters studied by ion spectroscopy *J. Phys. B: At. Mol. Opt. Phys.* **46** 164023 https://doi.org/10.1088/0953-4075/46/16/164023

[379] Yase S *et al.* 2013 Crossover in the photoionization processes of neon clusters with increasing EUV free-electron-laser intensity *Phys. Rev. A* **88** 043203 https://doi.org/10.1103/PhysRevA.88.043203

[380] Nagaya K *et al.* 2016 Interatomic Coulombic decay cascades in multiply excited neon clusters *Nature Communications* **13477** https://doi.org/10.1038/ncomms13477

[381] Cederbaum L S, Zobeley J and Tarantelli F 1997 Giant Intermolecular Decay and Fragmentation of Clusters *Phys. Rev. Lett.* **79** 4778 https://doi.org/10.1103/PhysRevLett.79.4778

[382] Kuleff A I *et al.* 2010 Ultrafast Interatomic Electronic Decay in Multiply Excited Clusters *Phys. Rev. Lett.* **105** 043004 https://doi.org/10.1103/PhysRevLett.105.043004

[383] LaForge A *et al.* 2014 Collective Autoionization in Multiply-Excited Systems: A novel ionization process observed in Helium Nanodroplets *Sci. Rep.* **4** 3621 https://doi.org/10.1038/srep03621

[384] Ovcharenko Y *et al.* 2014 Novel Collective Autoionization Process Observed in Electron Spectra of He Clusters *Phys. Rev. Lett.* **112** 073401 https://doi.org/10.1103/PhysRevLett.112.073401

[385] Bostedt C *et al.* 2008 Multistep Ionization of Argon Clusters in Intense Femtosecond Extreme Ultraviolet Pulses *Phys. Rev. Lett.* **100** 133401 https://doi.org/10.1103/PhysRevLett.100.133401

[386] Bostedt C *et al.* 2010 Fast electrons from multi-electron dynamics in xenon clusters induced by inner-shell ionization *New. J. Phys.* **12** 083004 https://doi.org/doi:10.1088/1367-2630/12/8/083004

[387] Arbeiter M and Fennel T 2011 Rare-gas clusters in intense VUV, XUV and soft x-ray pulses: signatures of the transition from nanoplasma-driven cluster expansion to Coulomb explosion in ion and electron spectra *New J. Phys.* **13** 053022 http://dx.doi.org/10.1088/1367-2630/13/5/053022

[388] Bostedt C *et al.* 2010 Clusters in intense FLASH pulses: ultrafast ionization dynamics and electron emission studied with spectroscopic and scattering techniques *J. Phys. B* **43** 194011 http://dx.doi.org/10.1088/0953-4075/43/19/194011

[389] Rupp D *et al.* 2012 Identification of twinned gas phase clusters by single-shot scattering with intense soft X-ray pulses *New. J. Phys.* **14** 055016 https://doi.org/10.1088/1367-2630/14/5/055016

[390] Bostedt C *et al.* 2012 Ultrafast X-Ray Scattering of Xenon Nanoparticles: Imaging Transient States of Matter *Phys. Rev. Lett.* **108** 093401 https://doi.org/10.1103/PhysRevLett.108.093401

[391] Thomas H *et al.* 2012 Explosions of Xenon Clusters in Ultraintense Femtosecond X-Ray Pulses from the LCLS Free Electron Laser *Phys. Rev. Lett.* **108** 133401 https://doi.org/10.1103/PhysRevLett.108.133401

[392] Gorkhover T *et al.* 2012 Nanoplasma Dynamics of Single Large Xenon Clusters Irradiated with Superintense X-Ray Pulses from the Linac Coherent Light Source Free-Electron Laser *Phys. Rev. Lett.* **108** 245005 https://doi.org/10.1103/PhysRevLett.108.245005

[393] Tachibana T *et al.* 2015 Nanoplasma Formation by High Intensity Hard X-rays *Sci. Rep.* **5** 10977 https://doi.org/10.1038/srep10977

[394] Zewail A H 1988 Laser Femtochemistry *Science* **242** 1645 https://doi.org/10.1126/science.242.4886.1645

[395] Haldrup K *et al.* 2016 Observing Solvation Dynamics with Simultaneous Femtosecond X-ray Emission Spectroscopy and X-ray Scattering *J. Phys. Chem. B* **120** 1158 https://doi.org/10.1021/acs.jpcb.5b12471

[396] Lemke H T *et al.* 2013 Femtosecond X-ray Absorption Spectroscopy at a Hard X-ray Free Electron Laser: Application to Spin Crossover Dynamics *J. Phys. Chem. A* **117** 735 https://doi.org/10.1021/jp312559h

[397] Kunnus K *et al.* 2016 Identification of the dominant photochemical pathways and mechanistic insights to the ultrafast ligand exchange of $Fe(CO)_5$ to $Fe(CO)_4$EtOH *Structural Dynamics* **3** 043204 https://doi.org/10.1063/1.4941602

[398] Wernet P *et al.* 2015 Orbital-specific mapping of the ligand exchange dynamics of Fe(CO)$_5$ in solution *Nature* **520** 78 https://doi.org/10.1038/nature14296

[399] Schreck S *et al.* 2014 Reabsorption of Soft X-Ray Emission at High X-Ray Free-Electron Laser Fluences *Phys. Rev. Lett.* **113** 153002 https://doi.org/10.1103/PhysRevLett.113.153002

[400] McFarland B K *et al.* 2014 Ultrafast X-ray Auger probing of photoexcited molecular dynamics *Nature Communications* **5** 4235 https://doi.org/10.1038/ncomms5235

[401] Zhang W *et al.* 2014 Tracking excited-state charge and spin dynamics in iron coordination complexes *Nature* **509** 345 https://doi.org/10.1038/nature13252

[402] Uemura Y *et al.* 2015 Dynamics of Photoelectrons and Structural Changes of Tungsten Trioxide Observed by Femtosecond Transient XAFS *Angewandte Chemie International Edition* **55** 1364 https://doi.org/10.1002/anie.201509252

[403] Ogi Y *et al.* 2015 Ultraviolet photochemical reaction of [Fe(III)(C$_2$O$_4$)$_3$]$^{3-}$ in aqueous solutions studied by femtosecond time-resolved X-ray absorption spectroscopy using an X-ray free electron laser *Structural Dynamics* **2** 034901 https://doi.org/10.1063/1.4918803

[404] Bressler C *et al.* 2009 Femtosecond XANES Study of the Light-Induced Spin Crossover Dynamics in an Iron(II) Complex *Science* **323** 489 https://doi.org/10.1126/science.1165733

[405] Milne C J, Penfold T J and Chergui M 2014 Recent experimental and theoretical developments in time-resolved X-ray spectroscopies *Coordination Chemistry Reviews* **277** 44 https://doi.org/10.1016/j.ccr.2014.02.013

[406] Neutze R and Moffat K 2012 Time-resolved structural studies at synchrotrons and X-ray free electron lasers: opportunities and challenges *Curr. Opin. Struct. Bio.* **22** 651 https://doi.org/10.1016/j.sbi.2012.08.006

[407] Kim J *et al.* 2010 Ultrafast X-ray diffraction in liquid, solution and gas: present status and future prospects *Acta Cryst. Sect. A* **66** 270 https://doi.org/10.1107/S0108767309052052

[408] Haldrup K, Christensen M and Nielsen M M 2010 Analysis of time-resolved X-ray scattering data from solution-state systems *Acta Cryst. Sect. A* **66** 261 https://doi.org/10.1107/S0108767309054233

[409] Vankó G *et al.* 2010 Picosecond Time-Resolved X-Ray Emission Spectroscopy: Ultrafast Spin-State Determination in an Iron Complex *Angewandte Chemie International Edition* **49** 5910 https://doi.org/10.1002/anie.201000844

[410] Vankó G *et al.* 2013 Spin-state studies with XES and RIXS: From static to ultrafast *J. Elect. Spec. Relat. Phenom.* **188** 166 https://doi.org/10.1016/j.elspec.2012.09.012

[411] Chen L X, Zhang X and Shelby M L 2014 Recent advances on ultrafast X-ray spectroscopy in the chemical sciences *Chemical Science* **5** 4136 https://doi.org/10.1039/C4SC01333F

[412] Kim J *et al.* 2016 Tracking reaction dynamics in solution by pump-probe X-ray absorption spectroscopy and X-ray liquidography (solution scattering) *Chemical Communications* **52** 3734 https://doi.org/10.1039/C5CC08949B

[413] Canton S E *et al.* 2015 Visualizing the non-equilibrium dynamics of photoinduced intramolecular electron transfer with femtosecond X-ray pulses *Nature Communications* Article number: 6359 https://doi.org/10.1038/ncomms7359

[414] Haldrup K *et al.* 2012 Guest–Host Interactions Investigated by Time-Resolved X-ray Spectroscopies and Scattering at MHz Rates: Solvation Dynamics and Photoinduced Spin Transition in Aqueous Fe(bipy)$_3^{2+}$ *J. Phys. Chem. A* **116** 9878 https://doi.org/10.1021/jp306917x

[415] Vankó G *et al.* 2015 Detailed Characterization of a Nanosecond-Lived Excited State: X-ray and Theoretical Investigation of the Quintet State in Photoexcited [Fe(terpy)$_2$]$^{2+}$ *J. Phys. Chem. C* **119** 5888 https://doi.org/10.1021/acs.jpcc.5b00557

[416] Minitti M P *et al.* 2015 Imaging Molecular Motion: Femtosecond X-Ray Scattering of an Electrocyclic Chemical Reaction *Phys. Rev. Lett.* **114** 255501 https://doi.org/10.1103/PhysRevLett.114.255501

[417] Budarz J M *et al.* 2016 Observation of femtosecond molecular dynamics via pump-probe gas phase X-ray scattering *J. Phys. B: At. Mol. Opt. Phys.* **49** 034001 https://doi.org/10.1088/0953-4075/49/3/034001

[418] Blaj G *et al.* 2015 X-ray detectors at the Linac Coherent Light Source *J. Synch. Rad.* **22** 577 https://doi.org/10.1107/S1600577515005317

[419] Öberg H *et al.* 2015 Optical laser-induced CO desorption from Ru(0001) monitored with a free-electron X-ray laser: DFT prediction and X-ray confirmation of a precursor state *Surface*

Science 80 https://doi.org/10.1016/j.susc.2015.03.011

[420] LaRue J L *et al.* 2015 THz-Pulse-Induced Selective Catalytic CO Oxidation on Ru *Phys. Rev. Lett.* **115** 036103 https://doi.org/10.1103/PhysRevLett.115.036103

[421] Ostrom H *et al.* 2015 Probing the transition state region in catalytic CO oxidation on Ru *Science* **347** 978 https://doi.org/10.1126/science.1261747

[422] Beye M *et al.* 2013 Selective Ultrafast Probing of Transient Hot Chemisorbed and Precursor States of CO on Ru(0001) *Phys. Rev. Lett.* **110** 186101 https://doi.org/10.1103/PhysRevLett.110.186101

[423] Dell'Angela M *et al.* 2013 Real-Time Observation of Surface Bond Breaking with an X-ray Laser *Science* **339** 1302 https://doi.org/10.1126/science.1231711

[424] Katayama T *et al.* 2013 Ultrafast soft X-ray emission spectroscopy of surface adsorbates using an X-ray free electron laser *J. Elect. Spec. Relat. Phenom.* **187** 9 https://doi.org/10.1016/j.elspec.2013.03.006

[425] Neppl S and Gessner O 2015 Time-resolved X-ray photoelectron spectroscopy techniques for the study of interfacial charge dynamics *J. Elect. Spec. Relat. Phenom.* **200** 64 https://doi.org/10.1016/j.elspec.2015.03.002

[426] Milne C J, Penfold T J and Chergui M 2014 Recent experimental and theoretical developments in time-resolved X-ray spectroscopies *Coordination Chemistry Reviews* **277-278** 44 https://doi.org/10.1016/j.ccr.2014.02.013

[427] Pietzsch A *et al.* 2008 Towards time resolved core level photoelectron spectroscopy with femtosecond X-ray free-electron lasers *New J. of Phys.* **10** 033004 https://doi.org/10.1088/1367-2630/10/3/033004

[428] Fognini A *et al.* 2014 The role of space charge in spin-resolved photoemission experiments *New J. of Phys.* **16** 043031 https://doi.org/10.1088/1367-2630/16/4/043031

[429] Hellmann S *et al.* 2009 Vacuum space-charge effects in solid-state photoemission *Phys. Rev. B* **79** 035402 https://doi.org/10.1103/PhysRevB.79.035402

[430] Hellmann S *et al.* 2010 Ultrafast Melting of a Charge-Density Wave in the Mott Insulator $1T$-TaS$_2$ *Phys. Rev. Lett.* **105** 187401 https://doi.org/10.1103/PhysRevLett.105.187401

[431] Fognini A *et al.* 2014 Ultrafast reduction of the total magnetization in iron *Appl. Phys. Lett.* **104** 032402 http://dx.doi.org/10.1063/1.4862476

[432] Oloff L P *et al.* 2014 Time-resolved HAXPES at SACLA: probe and pump pulse-induced space-charge effects *New J. Phys.* **16** 123045 http://dx.doi.org/10.1088/1367-2630/16/12/123045

[433] DellAngela M *et al.* 2016 Ultrafast surface dynamics probed with time resolved photoemission *Surf. Sci.* **643** 197 http://dx.doi.org/10.1016/j.susc.2015.08.011

[434] Frischkorn C and Wolf M 2006 Femtochemistry at Metal Surfaces: Nonadiabatic Reaction Dynamics *Chem. Rev.* **106** 4207 https://doi.org/10.1021/cr050161r

[435] Beaurepaire E *et al.* 1996 Ultrafast Spin Dynamics in Ferromagnetic Nickel *Phys. Rev. Lett.* **76** 4250 https://doi.org/10.1103/PhysRevLett.76.4250

[436] Stanciu C D *et al.* 2007 All-Optical Magnetic Recording with Circularly Polarized Light *Phys. Rev. Lett.* **99** 047601 https://doi.org/10.1103/PhysRevLett.99.047601

[437] Gutt C *et al.* 2010 Single-pulse resonant magnetic scattering using a soft x-ray free-electron laser *Phys. Rev. B* **81** 100401 https://doi.org/10.1103/PhysRevB.81.100401

[438] Schlotter W F *et al.* 2012 The soft x-ray instrument for materials studies at the linac coherent light source x-ray free-electron laser *Rev. Sci. Inst.* **83** 043107 http://dx.doi.org/10.1063/1.3698294

[439] Wang T H *et al.* 2012 Femtosecond Single-Shot Imaging of Nanoscale Ferromagnetic Order in Co/Pd Multilayers Using Resonant X-Ray Holography *Phys. Rev. Lett.* **108** 267403 https://doi.org/10.1103/PhysRevLett.108.267403

[440] Pfau B *et al.* 2012 Ultrafast optical demagnetization manipulates nanoscale spin structure in domain walls *Nature Comm.* **3** 1100 https://doi.org/10.1038/ncomms2108

[441] Graves C E *et al.* 2013 Nanoscale spin reversal by non-local angular momentum transfer following ultrafast laser excitation in ferrimagnetic GdFeCo *Nature Materials* **12** 293 https://doi.org/10.1038/nmat3597

[442] Müller L *et al.* 2013 Breakdown of the X-Ray Resonant Magnetic Scattering Signal during Intense Pulses of Extreme Ultraviolet Free-Electron-Laser Radiation *Phys. Rev. Lett.* **110** 234801 https://doi.org/10.1103/PhysRevLett.110.234801

[443] Wu B *et al.* 2016 Elimination of X-Ray Diffraction through Stimulated X-Ray Transmission *Phys. Rev. Lett.* **117** 027401 https://doi.org/10.1103/PhysRevLett.117.027401

[444] Schmising C V *et al.* 2014 Imaging Ultrafast Demagnetization Dynamics after a Spatially Localized Optical Excitation *Phys. Rev. Lett.* **112** 217203 https://doi.org/10.1103/PhysRevLett.112.217203

[445] Lutman A A *et al.* 2016 Polarization control in an X-ray free-electron laser *Nature Photonics* **10** 468 https://doi.org/10.1038/nphoton.2016.79

[446] Pontius N *et al.* 2011 Time-resolved resonant soft x-ray diffraction with free-electron lasers: Femtosecond dynamics across the Verwey transition in magnetite *Appl. Phys. Lett.* **98** 182504 http://dx.doi.org/10.1063/1.3584855

[447] de Jong S *et al.* 2013 Speed limit of the insulator-metal transition in magnetite *Nature Materials* **12** 882 https://doi.org/10.1038/nmat3718

[448] Chuang Y D *et al.* 2013 Real-Time Manifestation of Strongly Coupled Spin and Charge Order Parameters in Stripe-Ordered $La_{1.75}Sr_{0.25}NiO_4$ Nickelate Crystals Using Time-Resolved Resonant X-Ray Diffraction *Phys. Rev. Lett.* **110** 127404 https://doi.org/10.1103/PhysRevLett.110.127404

[449] Beaud P *et al.* 2014 A time-dependent order parameter for ultrafast photoinduced phase transitions *Nature Materials* **13** 923 https://doi.org/10.1038/nmat4046

[450] Kubacka T *et al.* 2014 Large-amplitude spin dynamics driven by a THz pulse in resonance with an electromagnon *Science* **343** 1333 https://doi.org/10.1126/science.1242862

[451] Fausti D *et al.* 2011 Light-Induced Superconductivity in a Stripe-Ordered Cuprate *Science* **331** 6014 https://doi.org/10.1126/science.1197294

[452] Mankowsky R *et al.* 2014 Nonlinear lattice dynamics as a basis for enhanced superconductivity in $YBa_2Cu_3O_{6.5}$ *Nature* **516** 71 https://doi.org/10.1038/nature13875

[453] Dean M P M *et al.* 2016 Ultrafast energy- and momentum-resolved dynamics of magnetic correlations in the photo-doped Mott insulator Sr_2IrO_4 *Nature Materials* **15** 601 https://doi.org/10.1038/nmat4641

[454] Trigo M *et al.* 2013 Fourier-transform inelastic X-ray scattering from time- and momentum-dependent phonon-phonon correlations *Nature Physics* **9** 790 https://doi.org/10.1038/nphys2788

[455] Gerber S *et al.* 2015 Three-dimensional charge density wave order in $YBa_2Cu_3O_{6.67}$ at high magnetic fields *Science* **350** 949 https://doi.org/10.1126/science.aac6257

[456] Bloembergen N 1982 Nonlinear optics and spectroscopy *Rev. Mod. Phys.* **54** 685 https://doi.org/10.1103/RevModPhys.54.685

[457] Johnson P M and Otis C E 2013 Molecular Multiphoton Spectroscopy with Ionization Detection *Ann. Rev. Phys. Chem.* **32** 139 https://doi.org/10.1146/annurev.pc.32.100181.001035

[458] Mukamel S *et al.* 2013 Multidimensional Attosecond Resonant X-Ray Spectroscopy of Molecules: Lessons from the Optical Regime *Ann. Rev. Phys. Chem.* **64** 101 https://doi.org/10.1146/annurev-physchem-040412-110021

[459] Göppert-Mayer M 1931 Über Elementarakte mit zwei Quantensprüngen *Annalen der Physik* **401** 273 http://dx.doi.org/10.1002/andp.19314010303

[460] Doumy G *et al.* 2011 Nonlinear Atomic Response to Intense Ultrashort X Rays *Physical Review Letters* **106** 083002 http://dx.doi.org/10.1103/PhysRevLett.106.083002

[461] Tamasaku K *et al.* 2014 X-ray two-photon absorption competing against single and sequential multiphoton processes *Nature Photonics* **8** 313 http://dx.doi.org/10.1038/NPHOTON.2014.10

[462] Szlachetko J *et al.* 2016 Establishing nonlinearity thresholds with ultraintense X-ray pulses *Scientific Reports* **6** 33292 http://dx.doi.org/10.1038/srep33292

[463] Ghimire S *et al.* 2016 Nonsequential two-photon absorption from the K shell in solid zirconium *Physical Review A - Atomic, Molecular, and Optical Physics* **94** 043418 http://dx.doi.org/10.1103/PhysRevA.94.043418

[464] Nordgren J *et al.* 1989 Soft X-ray emission spectroscopy using monochromatized synchrotron radiation (invited) *Rev. Sci. Inst.* **60** 1690 https://doi.org/10.1063/1.1140929

[465] Beye M *et al.* 2013 Stimulated X-ray emission for materials science *Nature* **501** 191 https://doi.org/10.1038/nature12449

[466] Bencivenga F *et al.* 2015 Coherent and transient states studied with extreme ultraviolet and X-ray free electron lasers: present and future prospects *Adv. in Physics* **63** 327 https://doi.org/10.1080/00018732.2014.1029302

[467] Sjodin T *et al.* 2000 Ultrafast transient grating scattering studies of carrier dynamics at a silicon surface *Chemical Physics* **251** 205 https://doi.org/10.1016/S0301-0104(99)00365-1

[468] Bencivenga F and Masciovecchio C 2009 FEL-based transient grating spectroscopy to investigate nanoscale dynamics *Nucl. Instr. Meth.* **A606** 785 https://doi.org/10.1016/j.nima.2009.05.147

[469] Bencivenga F *et al.* 2013 Nanoscale dynamics by short-wavelength four wave mixing experiments *New J. of Phys.* **15** 123023 https://doi.org/10.1088/1367-2630/15/12/123023

[470] Turner B D and Nelson K A 2010 Coherent measurements of high-order electronic correlations in quantum wells *Nature* **466** 1089 https://doi.org/10.1038/nature09286

[471] Collini E *et al.* 2010 Coherently wired light-harvesting in photosynthetic marine algae at ambient temperature *Nature* **463** 644 https://doi.org/10.1038/nature08811

[472] Bencivenga F *et al.* 2015 Four wave mixing experiments with extreme ultraviolet transient gratings *Nature* **520** 205 https://doi.org/10.1038/nature14341

[473] Cundiff S T and Mukamel S 2013 Optical multidimensional coherent spectroscopy *Phys. Today* **66** 44 https://doi.org/10.1063/PT.3.2047

[474] Correa A A, Bonev S A and Galli G 2006 Carbon under extreme conditions: Phase boundaries and electronic properties from first-principles theory. *Proc. Natl. Acad. Sci. U S A* **103** 1204 https://doi.org/10.1073/pnas.0510489103

[475] Sun J, Klug D D and Martoňák R 2009 Structural transformations in carbon under extreme pressure: Beyond diamond *J. Chem. Phys.* **130** 194512 https://doi.org/10.1063/1.3139060

[476] Johnson Q *et al.* 1971 X-ray Diffraction Evidence for Crystalline Order and Isotropic Compression during the Shock-wave Process *Nature* **231** 5301 https://doi.org/10.1038/231310b0

[477] Johnson Q *et al.* 1972 Xray diffraction study of single crystals undergoing shockwave compression *Appl. Phys. Lett.* **21** 29 https://doi.org/10.1063/1.1654205

[478] Rigg P A and Gupta Y M 1998 Real-time X-ray diffraction to examine elasticplastic deformation in shocked lithium fluoride crystals *Appl. Phys. Lett.* **73** 1655 http://scitation.aip.org/content/aip/journal/apl/73/12/10.1063/1.122236

[479] Gupta Y M *et al.* 1999 Experimental developments to obtain real-time X-ray diffraction measurements in plate impact experiments *Rev. Sci. Inst.* **70** 4008 http://scitation.aip.org/content/aip/journal/rsi/70/10/10.1063/1.1150026

[480] Turneaure S J and Gupta Y M 2007 X-ray diffraction and continuum measurements in silicon crystals shocked below the elastic limit *Appl. Phys. Lett.* **90** 051905 https://doi.org/10.1063/1.2436638

[481] Wark J S *et al.* 1989 Subnanosecond X-ray diffraction from laser-shocked crystals *Phys. Rev. B* **40**(8) 5705 https://doi.org/10.1103/PhysRevB.40.5705

[482] Loveridge-Smith A *et al.* 2001 Anomalous Elastic Response of Silicon to Uniaxial Shock Compression on Nanosecond Time Scales *Phys. Rev. Lett.* **86**(11) 2349 https://doi.org/10.1103/PhysRevLett.86.2349

[483] Kalantar D H *et al.* 2005 Direct Observation of the α-ϵ Transition in Shock-Compressed Iron via Nanosecond X-Ray Diffraction *Phys. Rev. Lett.* **95**(7) 075502 https://doi.org/10.1103/PhysRevLett.95.075502

[484] Wang J *et al.* 2015 X-ray diffraction of molybdenum under shock compression to 450 GPa *Phys. Rev. B* **92**(17) 174114 https://doi.org/10.1103/PhysRevB.92.174114

[485] Lazicki A *et al.* 2015 X-Ray Diffraction of Solid Tin to 1.2 TPa *Phys. Rev. Lett.* **115**(7) 075502 https://doi.org/10.1103/PhysRevLett.115.075502

[486] Milathianaki D *et al.* 2013 Femtosecond Visualization of Lattice Dynamics in Shock-Compressed Matter *Science* **342** 220 https://doi.org/10.1126/science.1239566

[487] Wehrenberg C 2016 Personal Communication

[488] Bringa E M *et al.* 2006 Shock deformation of face-centred-cubic metals on subnanosecond timescales *Nature materials* **5** 805 https://doi.org/10.1038/nmat1735

[489] Dupont V and Germann T C 2012 Strain rate and orientation dependencies of the strength of single crystalline copper under compression *Phys. Rev. B* **86**(13) 134111 https://doi.org/10.1103/PhysRevB.86.134111

[490] Higginbotham A and McGonegle D 2014 Prediction of Debye-Scherrer diffraction patterns in arbitrarily strained samples *J. Appl. Phys.* **115** 174906 https://doi.org/10.1063/1.4874656

[491] Wark J S *et al.* 2014 Combined Hydrodynamic and Diffraction Simulations of Fem-

tosecond X-ray Scattering from Laser-Shocked Crystals *Journal of Physics: Conference Series* **500** 152016 https://doi.org/10.1088/1742-6596/500/15/152016

[492] Taylor J W 1965 Dislocation Dynamics and Dynamic Yielding *J. Appl. Phys.* **36** 3146 https://doi.org/10.1063/1.1702940

[493] Gorman M G *et al.* 2015 Direct Observation of Melting in Shock-Compressed Bismuth With Femtosecond X-ray Diffraction *Phys. Rev. Lett.* **115**(9) 095701 https://doi.org/10.1103/PhysRevLett.115.095701

[494] Hayes D B 1975 Wave propagation in a condensed medium with N transforming phases: Application to solidIsolidIIliquid bismuth *J. Appl. Phys.* **46** 3438 https://doi.org/10.1063/1.322065

[495] Bastea M *et al.* 2005 Kinetics of propagating phase transformation in compressed bismuth *Phys. Rev. B* **71** 180101(R) https://doi.org/10.1103/PhysRevB.71.180101

[496] Kraus D *et al.* 2016 Nanosecond formation of diamond and lonsdaleite by shock compression of graphite *Nature Communications* **7** https://doi.org/10.1038/ncomms10970

[497] McMahon M 2016 Personal Communication

[498] Briggs R *et al.* Ultra-fast X-ray Diffraction Studies of the Phase Transitions and Equation of State of Scandium Shock-Compressed to 82 GPa *Phys. Rev. Lett.* Accepted

[499] Gleason A E *et al.* 2015 Ultrafast visualization of crystallization and grain growth in shock-compressed SiO_2 *Nat. Comm.* **6** https://doi.org/10.1038/ncomms9191

[500] Clark J N *et al.* 2013 Ultrafast Three-Dimensional Imaging of Lattice Dynamics in Individual Gold Nanocrystals **341** 56 http://science.sciencemag.org/content/341/6141/56

[501] Clark J N *et al.* 2015 Imaging transient melting of a nanocrystal using an X-ray laser *Proc. Natl. Acad. Sci. U.S.A.* **112** 7444 http://www.pnas.org/content/112/24/7444.abstract

[502] Gorkhover T *et al.* 2016 Femtosecond and nanometre visualization of structural dynamics in superheated nanoparticles *Nature Photonics* **10** 93 https://doi.org/10.1038/nphoton.2015.264

[503] Schropp A *et al.* 2015 Imaging Shock Waves in Diamond with Both High Temporal and Spatial Resolution at an XFEL *Scientific Reports* **5** 11089 EP https://doi.org/10.1038/srep11089

[504] McGonegle D *et al.* 2015 Simulations of in situ X-ray diffraction from uniaxially compressed highly textured polycrystalline targets *J. Appl. Phys.* **118** 065902 https://doi.org/10.1063/1.4927275

[505] Higginbotham A *et al.* 2012 Molecular dynamics simulations of ramp-compressed copper *Phys. Rev. B* **85** 024112 https://doi.org/10.1103/PhysRevB.85.024112

[506] Grady D E 2010 Structured shock waves and the fourth-power law *J. Appl. Phys.* **107** 013506 https://doi.org/10.1063/1.3269720

[507] Banerjee S *et al.* 2013 DiPOLE: A multi-slab cryogenic diode pumped Yb:YAG amplifier https://doi.org/10.1117/12.2016611

[508] Vinko S 2015 X-ray free-electron laser studies of dense plasmas *Journal of Plasma Physics* **81** 365810501 https://doi.org/10.1017/S0022377815000902

[509] Lévy A *et al.* 2015 The creation of large-volume, gradient-free warm dense matter with an X-ray free-electron laser *Physics of Plasmas* **22** 030703 https://doi.org/10.1063/1.4916103

[510] Vinko S *et al.* 2012 Creation and diagnosis of a solid-density plasma with an X-ray free-electron laser. *Nature* **482** 59 https://doi.org/10.1038/nature10746

[511] Schlotter W F *et al.* 2012 The soft X-ray instrument for materials studies at the linac coherent light source X-ray free-electron laser *Rev. Sci. Inst.* **83** 043107 https://doi.org/10.1063/1.3698294

[512] Ciricosta O *et al.* 2016 Detailed model for hot-dense aluminum plasmas generated by an X-ray free electron laser *Physics of Plasmas* **23** https://doi.org/10.1063/1.4942540

[513] Cho B *et al.* 2012 Resonant Kα Spectroscopy of Solid-Density Aluminum Plasmas *Phys. Rev. Lett.* **109** 245003 https://doi.org/10.1103/PhysRevLett.109.245003

[514] Ciricosta O *et al.* 2012 Direct Measurements of the Ionization Potential Depression in a Dense Plasma *Phys. Rev. Lett.* **109** 065002 https://doi.org/10.1103/PhysRevLett.109.065002

[515] Son S K *et al.* 2014 Quantum-mechanical calculation of ionization-potential lowering in dense plasmas *Phys. Rev. X* **4**(3) 031004 https://doi.org/10.1103/PhysRevX.4.031004

[516] Crowley B 2014 Continuum lowering – a new perspective *High Energy Density Physics* **13** 84 https://doi.org/10.1016/j.hedp.2014.04.003

[517] Vinko S M, Ciricosta O and Wark J S 2014 Density functional theory calculations of continuum lowering in strongly coupled plasmas *Nat. Commun.* **5** 3533 https://doi.org/10.1038/ncomms4533

[518] Calisti A, Ferri S and Talin B 2015 Ionization potential depression in hot dense plasmas through a pure classical model *Contributions to Plasma Physics* **55** 360 https://doi.org/10.1002/ctpp.201400087

[519] Ciricosta O *et al.* 2016 Measurements of continuum lowering in solid-density plasmas created from elements and compounds *Nat. Commun.* **7** 11713 https://doi.org/10.1038/ncomms11713

[520] Vinko S *et al.* 2015 Investigation of femtosecond collisional ionization rates in a solid-density aluminium plasma *Nat. Commun.* **6** 6397 https://doi.org/10.1038/ncomms7397

[521] Yoneda H *et al.* 2014 Saturable absorption of intense hard x-rays in iron *Nat. Commun.* **5** 5080 https://doi.org/10.1038/ncomms6080

[522] Rackstraw D *et al.* 2015 Saturable absorption of an x-ray free-electron-laser heated solid-density aluminum plasma *Phys. Rev. Lett.* **114**(1) 015003 https://doi.org/10.1103/PhysRevLett.114.015003

[523] Nagler B *et al.* 2009 Turning solid aluminium transparent by intense soft X-ray photoionization *Nature Physics* **5** 693 https://doi.org/10.1038/nphys1341

[524] Stewart J C and Pyatt K J 1966 Lowering of ionization potentials in plasmas *The Astrophysical Journal* **144** 1203 https://doi.org/10.1086/148714

[525] Ecker and Kröll 1963 Lowering of the Ionization Energy for a Plasma in Thermodynamic Equilibrium *The Physics of Fluids* **6** 62 https://doi.org/10.1063/1.1724509

[526] Fäustlin R R *et al.* 2010 Observation of Ultrafast Nonequilibrium Collective Dynamics in Warm Dense Hydrogen *Phys. Rev. Lett.* **104** 2 https://doi.org/10.1103/PhysRevLett.104.125002

[527] Zastrau U *et al.* 2014 Resolving ultrafast heating of dense cryogenic hydrogen *Phys. Rev. Lett.* **112**(10) 105002 https://doi.org/10.1103/PhysRevLett.112.105002

[528] Brown C R D *et al.* 2014 Evidence for a glassy state in strongly driven carbon *Scientific Reports* **4** 5214 EP https://doi.org/10.1038/srep05214

[529] Fletcher L B *et al.* 2015 Ultrabright X-ray laser scatterong for dynamic warm dense matter physics *Nature Photonics* https://doi.org/10.1038/NPHOTON.2015.41

[530] Sperling P *et al.* 2015 Free-Electron X-Ray Laser Measurements of Collisional-Damped Plasmons in Isochorically Heated Warm Dense Matter *Phys. Rev. Lett.* **115**(11) 115001 https://doi.org/10.1103/PhysRevLett.115.115001

[531] White T G 2014 *Study of High Energy Density Matter through Quantum Molecular Dynamics and Time Resolved X-ray Scattering* Ph.D. thesis University of Oxford

[532] ACARE Flightpath 2050 targets http://www.acare4europe.org/sria/flightpath-2050-goals/protecting-environment-and-energy-supply-0/

[533] 2015 Rolls Royce plc: Annual Report 2015 http://www.rolls-royce.com/investors/annual-report-archive.aspx#annual-reports

[534] Rugg D 2014 Materials for Future Gas Turbine Applications *Materials Science and Technology* **30** 1848 https://doi.org/10.1179/1743284714Y.0000000609

[535] Rugg D, Burrows J and Dixon M 2016 High Temperature application of titanium alloys in gas turbines. Material life cycle opportunities and threats - an industrial perspective *Materials at High Temperatures* **33** 536 https://doi.org/10.1080/09603409.2016.1184423

[536] http://www.ati.org.uk/strategy/publications/

[537] Castelluccio G M *et al.* 2014 Recent developments in assessing microstructure-sensitive early stage fatigue of polycrystals *Current Opinion in Solid State and Materials Science* **18** 180 https://doi.org/10.1016/j.cossms.2014.03.001

[538] Szczepanski C J *et al.* 2013 Development of a microscale fatigue testing technique *Advanced Materials and Processes* **171** 18 http://www.asminternational.org/documents/10192/6016508/amp17106p18.pdf/7c40988b-7d40-478e-9a4b-fb2ccb905409/AMP17106P18

[539] Armstrong D E J, Rogers M E and Roberts S G 2009 Micromechanical testing of stress corrosion cracking of individual grain boundaries *Scripta Mat.* **61** 741 https://doi.org/10.1016/j.scriptamat.2009.06.017

[540] Britton T B, Randman D and Wilkinson A J 2009 Nanoindentation study of slip transfer phenomenon at grain boundaries *J. Mat. Res.* **24** 607 https://doi.org/10.1557/jmr.2009.0088

[541] Guo Y *et al.* 2015 Measurements of stress fields near a grain boundary: Exploring blocked arrays of dislocations in 3D *Acta Mat.* **96** 229 https://doi.org/10.1016/j.actamat.2015.05.041

[542] Yu Q *et al.* 2015 Origin of dramatic oxygen solute strengthening effect in Titanium *Science* **347** 635 https://doi.org/10.1126/science.1260485

[543] Burr P A *et al.* 2015 From solid solution to cluster formation of Fe and Cr in α-Zr *J. Nucl. Mat.* **467** 320 https://doi.org/10.1016/j.jnucmat.2015.10.001

[544] Lavrentiev Y, Nguyen-Manh D and Dudarev S L 2010 Magnetic cluster expansion model for bcc-fcc transitions in Fe and Fe-Cr alloys *Phys. Rev. B* **81** 184202 https://doi.org/10.1103/PhysRevB.81.184202

[545] Mason D R *et al.* 2014 Elastic trapping of dislocation loops in cascades in ion-irradiated tungsten foils *J. Phys. Cond. Matter* **26** 375701 https://doi.org/10.1088/0953-8984/26/37/375701

[546] Swinburne T D *et al.* 2016 Picosecond dynamics of a shock-driven displacive phase transformation in Zr. *Phys. Rev. B* **93** 144119 https://doi.org/10.1103/PhysRevB.93.144119

[547] Maire E and Withers P J 2014 Quantitative X-ray tomography *Int. Mat. Rev.* **59** 1 https://doi.org/10.1179/1743280413Y.0000000023

[548] Wielewski E *et al.* 2015 Three-dimensional alpha colony characterization and prior-beta grain reconstruction of a lamellar Ti-6Al-4V specimen using near-field high-energy X-ray diffraction microscopy *J. Appl. Cryst.* **48** 1165 https://doi.org/10.1107/S1600576715011139

[549] Moore G 1965 Cramming more components onto integrated circuits *Electronics Magazine* **38**

[550] Wagner C and Harned N 2010 EUV lithography: Lithography gets extreme *Nature Photonics* **4** 24 https://doi.org/10.1038/nphoton.2009.251

[551] Bakshi V 2009 *EUV Lithography* (SPIE, Washington, and John Wiley & Sons, New Jersey)

[552] Endo A 2015 Status and Potential of Laser based EUV Sources *CLEO: 2015* (Optical Society of America) https://doi.org/10.1364/CLEO_AT.2015.ATu4M.5

[553] Hosler E R *et al.* 2015 Considerations for a free-electron laser-based extreme-ultraviolet lithography program *Proc. SPIE* **9422** 94220D https://doi.org/10.1117/12.2085538

[554] Hosler E R, Wood O R and Preil M E 2016 Extending extreme-UV lithography technology *SPIE Newsroom* https://doi.org/10.1117/2.1201601.006323

[555] Neil G *et al.* 2006 The JLab high power ERL light source *Nucl. Inst. Meth. Phys. Res. Sect. A* **557** 9 https://doi.org/10.1016/j.nima.2005.10.047

[556] Benson S *et al.* 2007 High Power Operation of the JLab IR FEL Driver Accelerator *Proc. of PAC2007* p 79 https://doi.org/10.1109/PAC.2007.4440128

[557] Science & Technology Facilities Council (UK) 2016 Free-Electron Laser (FEL) Strategic Review https://www.stfc.ac.uk/files/fel-report-2016/